

1

3 **Supporting Information for “Detection of slow slip
4 events along the southern Peru - northern Chile
5 subduction zone”**

6 **J. Jara**  * ¹, **R. Jolivet**  ^{1,2}, **A. Socquet**  ³, **D. Comte**  ^{4,5}, **E. Norabuena**  ⁶

7 ¹Laboratoire de Géologie, Département de Géosciences, École Normale Supérieure, PSL Research University, CNRS UMR 8538, Paris,

8 France, ²Institut Universitaire de France, Paris, France, ³Université Grenoble Alpes, Université Savoie Mont Blanc, CNRS, IRD, IFSTTAR,

9 ISTerre, Grenoble, France, ⁴Departamento de Geofísica, Facultad de Ciencias Físicas y Matemáticas, Universidad de Chile, Blanco

10 Encalada 2002, Santiago, Chile, ⁵Advanced Mining Technology Center, Facultad de Ciencias Físicas y Matemáticas, Universidad de Chile,

11 Av. Tupper 2007, Santiago, Chile, ⁶Instituto Geofísico del Perú, Lima, Perú

12

*Corresponding author: now at GFZ Potsdam, jorge@gfz-potsdam.de

13 **Text S1. GNSS time series noise analysis**

14 Geodetic noise is usually modeled as a combination of white and colored noises (Williams, 2003; Bock and Melgar,
 15 2016), such as

$$16 \quad \mathbf{P}(f) = P_0 (\mathbf{f}^{-\alpha} + f_0^{-\alpha}), \quad (1)$$

17 where \mathbf{P} is the power spectrum of the frequency f , P_0 and f_0 are normalization constants, and α is the spectral index.
 18 We explore the geodetic noise in the GNSS time series of residuals, obtained after removing a best fit Trajectory Model
 19 (Bevis and Brown, 2014) and a common mode (see the Main Text for details in the procedure).

20 We Fourier transform each component of the residual time series (see an example in Figure S26. Then, we infer
 21 parameters P_0 , f_0 , and α in a Bayesian framework. We sample the possible parameters using a Metropolis algorithm,
 22 generating 10000 models and derive the mean and standard deviation for each parameter. Figure S27 shows the
 23 Probability Density Function (PDF) for each parameter for both components of station UAPE (see Tables S39 - S42 for
 24 all network noise parameters inferred following the same methodology). We then use the obtained distribution to
 25 generate 1000 synthetic noises for each component of each station, following the Eq. 1 (Figure S26).

26 **Text S2. Aseismic slip detections: synthetic tests and resolution maps**

27 We compute the weighted correlation function (WCF) at each fault node defined as

$$28 \quad \mathbf{C}_f(t) = \frac{\sum_{i=1}^{2N} |\mathbf{G}_i| \mathbf{C}_i(t)}{\sum_{i=1}^{2N} |\mathbf{G}_i|} \quad (2)$$

29 where \mathbf{G} denotes the Green's functions and \mathbf{C}_i is the correlation between the time series and the synthetic template
 30 at a given fault node i .

31 We split the network into three periods due to its evolution on time: 2000 - 2003 (four stations), 2004 - 2007 (20 sta-
 32 tions), 2008 - 2014 (55 stations). We examine the network sensitivity to detect aseismic events by doing synthetic tests
 33 for each of those periods. These tests consist of introducing synthetic transients to the synthetic noises mentioned
 34 above (with known duration, magnitude, and location), which enable us to perform a detection process and estimate
 35 statistics on the results.

36 Let us first set the procedure to build the synthetic aseismic events. We build a database using the 1000 synthetic
 37 noise for each period mentioned above. This database consists of 600-day long time series, plus synthetic aseismic
 38 events of 10, 20, and 30 days duration, centered on days 100, 300, and 500. At each fault node, such synthetic events
 39 have magnitudes ranging between M_w 5.0 - 7.0 (every 0.1 of magnitude). Our resolution approach is based on defining
 40 four parameters to study the network resolution: distance to the actual timing of maximum WCF ($M_{w_{tim}}$), duration
 41 ($M_{w_{dur}}$), magnitude ($M_{w_{mag}}$), and location ($M_{w_{loc}}$).

42 In the cases of the three first parameters, we carry out the WCF estimation (Eq. 2), analyzing fault nodes inde-
 43 pendently for each magnitude and duration. Considering the distance to the actual timing in the WCF, we know that
 44 this function might present peaks at the 100, 300, and 500 days. This idea is based on synthetic events are centered
 45 on such days. We estimate the difference between the real and synthetic timing on the WCF for the 1000 synthetics

46 noises as follows:

$$47 \quad Tim_{stats_{Tij}} = |PWCF_{Tij} - RPT_i|, \quad (3)$$

48 with PWCF, the peak on the WCF estimated from synthetics at the fault node T with a duration i (10, 20 and 30
49 days), and magnitude j (M_w 5.0 - 7.0, every 0.1 of magnitude), whereas RPT is the actual peak on time (days 100, 300,
50 and 500). To estimate the mean and the standard deviation on such results, we employ a Kernel Density Estimation
51 (KDE) rather than classic histograms, avoiding larger dispersions in statistical parameters. We cluster the potential
52 Gaussian distributions having more than 250 samples, estimating the mean and standard deviation for each one.
53 Then, we consider the Mode (the most probable model) of estimated means (and its associated standard deviation)
54 as the actual representative timing for a given fault node T , duration i , and magnitude j (see Figure S28, a and b (iv)
55 for an example at fault nodes 5 and 71, with synthetics of 10 days duration).

56 To estimate the magnitude and duration resolution, we consider the peaks on the WCF estimated above as pos-
57 itive detections, modeling them in a Bayesian framework. We consider that the following expression can represent
58 synthetic aseismic events (Rousset et al., 2017, 2019):

$$59 \quad s(t) = \frac{1}{2} \left[1 - \cos \left(\frac{\pi t}{dT} \right) \right], \quad (4)$$

60 where dT corresponds to the events duration, also considering two linear trends before and after that function. So,
61 we stack the noise time series with a length of 80 days, centered in the peak of the WCF, carrying out a Metropolis
62 exploration of the solution space with 30000 samples. By doing so, mean duration and magnitude are estimated,
63 enabling us to estimate the difference between such values and the real ones following:

$$64 \quad Dur_{stats_{Tij}} = |SDur_{Tij} - Dur_i|, \quad (5)$$

$$65 \quad Mag_{stats_{Tij}} = |SMag_{Tij} - Mag_i|. \quad (6)$$

66 Eq. 5 is related to the duration, where $SDur$ is the inferred synthetic duration at a given fault node T , duration i ,
67 and magnitude j , whereas Dur is the actual synthetic duration (10, 20, and 30 days). In addition, Eq. 6 describes the
68 differences between magnitudes, with $SMag$ the inferred synthetic magnitude at a given fault node T , duration i , and
69 magnitude j , whereas Mag is the actual synthetic magnitude ranging between M_w 5.0-7.0 (every 0.1 of magnitude).
70 As in the case of WCF timing resolution, we employ a KDE to cluster the potential Gaussian distributions. From
71 such results, we estimate the Mode to provide duration and magnitude values for a given fault node T , duration i ,
72 and magnitude j (see Figure S28, a and b (ii, iii) for an example at fault nodes 5 and 71, with synthetics of 10 days
73 duration).

74 In the synthetic location case, we assume that the event location takes place where the maximum of the WCF
75 (Eq. 2) is coming (Rousset et al., 2017). So, we need to calculate the WCF for all fault nodes and locate the maximum,
76 following:

$$77 \quad Loc_{stats_{Tij}} = \max_{t \in T} \{WCF_{tij}\}, \quad (7)$$

78 where T denotes the number of fault nodes, i duration (10, 20, and 30 days), and j magnitudes (M_w 5.0-7.0, every
 79 0.1 of magnitude). We use a KDE as in the previous examples to extract Gaussian distributions, taking the Mode of
 80 such results as the location values. We notice a large variability in the results (extremely high standard deviations),
 81 mainly because of the extension along the strike to the study area. Such effects might come from the fact that Green's
 82 functions are estimated using a velocity structure and not a half-space (Segall, 2010), along with the variation in the
 83 area size along the fault plane. Therefore, far fault nodes from the actual synthetic location might produce high cor-
 84 relation values, but they do not necessarily match the signature of the aseismic event searched. We apply a Pearson
 85 correlation to avoid such effects, which measures a linear correlation between the WCF of the true synthetic location
 86 with the WCF from the rest of the fault nodes. Thus, we search for WCF close in shape to the synthetic event one. We
 87 estimate such parameters following:

$$88 \quad Loc90_{stats_{Tij}} = \max_{\substack{WCF_{tij} > 0.9 * WCF_{syn} \\ t \in T}} \{WCF_{tij}\}, \quad (8)$$

89 where we consider a Person correlation coefficient higher than 90% to perform the statistics. We repeat the KDE
 90 processing to estimate the mean and standard deviation as the previous parameters for all faults nodes, duration,
 91 and magnitudes (see Figure S28, a and b (i) for an example at fault nodes 5 and 71, with synthetics of 10 days duration).

92 Once all parameters are estimated ($Tim_{stats_{Tij}}$, $Dur_{stats_{Tij}}$, $Mag_{stats_{Tij}}$, $Loc_{stats_{Tij}}$, $Loc90_{stats_{Tij}}$), we search for
 93 a minimal magnitude detectable at each fault node T . We define certain thresholds that help define a minimal res-
 94 olution. For the location case ($Loc_{stats_{Tij}}$, $Loc90_{stats_{Tij}}$), we consider a maximal distance of 150km, whereas in the
 95 distance to the actual magnitude we define 0.25 ($Mag_{stats_{Tij}}$). In the duration ($Dur_{stats_{Tij}}$) and distance to the actual
 96 timing ($Tim_{stats_{Tij}}$) cases we consider a limit of 5 days. By doing so, we define the threshold resolution at each fault
 97 node by:

$$98 \quad Res_{Ti} = \max_{t \in T} \{M_{w_{loc_{ti}}}, M_{w_{tim_{ti}}}, M_{w_{dur_{ti}}}, M_{w_{mag_{ti}}}\}, \quad (9)$$

99 where each M_w is defined as follows:

$$100 \quad M_{w_{loc_{ti}}} = \min_{\substack{Loc_{stats_{Tij}} \leq 150km \\ t \in T ; i \in 10,20,30}} \{Loc_{stats_{Tij}}\}, \quad (10)$$

$$101 \quad M_{w_{tim_{ti}}} = \min_{\substack{Tim_{stats_{Tij}} \leq 5 \\ t \in T ; i \in 10,20,30}} \{Tim_{stats_{Tij}}\}, \quad (11)$$

$$102 \quad M_{w_{dur_{ti}}} = \min_{\substack{Dur_{stats_{Tij}} \leq 5 \\ t \in T ; i \in 10,20,30}} \{Dur_{stats_{Tij}}\}, \quad (12)$$

$$103 \quad M_{w_{mag_{ti}}} = \min_{\substack{Mag_{stats_{Tij}} \leq 0.25 \\ t \in T ; i \in 10,20,30}} \{Mag_{stats_{Tij}}\}, \quad (13)$$

107 which enables us to build resolution maps for the tested synthetics events with duration of 10, 20, and 30 days. Choos-

108 ing the max of four parameters is based on the sensitivity of the location. Figure S28 a shows an example for fault
 109 nodes 5 and 71. For the fault node 5 case, even when we get some resolution for the magnitude, duration, and tim-
 110 ing, we see that the location never converges to values lower than 500km, independent of the period analyzed. That
 111 means the station distribution is not optimal in the location case, and thus, we need to consider the four parameters
 112 to estimate reliable resolution values at each fault node, which is also the case for fault node 71.

113 Subsequently, we produce the resolution maps by not considering Pearson's correlation (Figure S29) and including
 114 it (Figure S30) at the moment of estimating the location resolution (Eq. 7 and 8 in Eq. 9). Such maps exhibit that
 115 network detection capability depends directly on the available stations and their distribution to perform the analysis.
 116 Not using the Person correlation in the location analysis enables us to validate 20 aseismic events, whereas using it
 117 improve our detections to 24 events (events with * in Table S43). This choice seems appropriate when looking at the
 118 observations and modeled aseismic events (Figures S33, S37 and S43); thus, we consider validating our detections as
 119 aseismic slip events by using those where the Pearson's correlation is estimated.

120 Additionally, we analyze the capability of the template matching technique discriminating aseismic events from
 121 common-mode error, which is behavior spatially correlated (Wdowinski et al., 1997; Williams et al., 2003; Bock and
 122 Melgar, 2016). We introduce slip at the fault node 318 to an aseismic event of magnitude M_w 6.0 (Figure S31 a, dis-
 123 placement field denoted by red arrows), and synthetic events (10, 20, and 30 days) to GNSS time series of noise (Figure
 124 S31 c and d, for AEDA station which has the higher displacement amplitude). By applying our proposed methodology,
 125 we obtain the WCF (red curve Figure S31 c) that presents correlation peaks where the synthetic aseismic events are
 126 located (in timing). Then, we create a synthetic common-mode error with an amplitude of 1mm at each station (green
 127 arrows Figure S31c). We add such signals to the GNSS noise time series and apply the correlation technique, using the
 128 same template mentioned before. The associated WCF (green curve Figure S31 c) does not exhibit correlation peaks.
 129 Therefore, we are confident that the proposed methodology discriminates the common-mode error from aseismic
 130 slip events.

131

132 **Text S3. Seismic and Aseismic Moment comparison**

133 Our 33 detections are contrasted with the seismicity reported by the ISC (International Seismological Centre,
 134 2016) (Figure 1 Main Text). This procedure helps us to ensure our detections are not related to earthquakes and are
 135 actually aseismic slip events. To do so, we consider a multivariate normal distribution as follow:

$$136 \quad x_{ev} = \mathcal{N}(\mu_{ev}, \sigma_{ev}), \quad (14)$$

137 assuming that the location uncertainty is normally distributed. Here, ev corresponds to the aseismic event (Table
 138 S43), μ_{ev} its epicenter location, and σ_{ev} is the covariance matrix of the location. σ_{ev} is based on the resolution test
 139 analysis, considering the standard deviation of the minimal magnitude (synthetic location) at each fault node. That
 140 estimation enables us to generate randomly 10000 synthetic events for each aseismic event. Then, we consider all the
 141 earthquakes occurring at the same time as the aseismic event, estimating the total seismic moment for each event

142 as:

$$M_0^{sis} = \sum_{\substack{i=1 \\ dist(m_{0i}, x_{ev}) \leq 2\sigma_{ev}}}^{10000} 10^{\frac{3}{2}m_{0i} + 9.1}, \quad (15)$$

144 with m_{0i} the seismic moment released by all earthquakes at a distance less than $2\sigma_{ev}$. Such seismic moments are
 145 compared with the ones released by all aseismic events (M_0^{asis}), estimating the ratio between them. By doing so, we
 146 obtain that 30 of the reported aseismic events are transients with an aseismic ratio above 95%.

147

148 **Text S4. Moment-duration scaling**

149 We determine the moment-duration scaling following the approach of Michel et al. (2019). The moment-duration
 150 relation writes as,

$$\log_{10}(T) = \frac{1}{c} \log_{10}(M_0) + g, \quad (16)$$

151 where T is the event duration in seconds, M_0 the moment magnitude in [Nm], c the temporal scaling factor, and g
 152 a constant. In order to estimate the scaling factor c , we use the curve fit function from the Scipy Python package
 153 (Virtanen et al., 2020) to fit Eq. 1 to our data, resulting in a moment-duration scaling of $M \propto T^{4.12 \pm 1.64}$ (red curve,
 154 Figure S45 a and b). We set bounds for c to $[0.1, 100]$ and g to $[-35, 1000]$.

155 We also compare our detections with best fitting T and T^3 scalings (black and green curves, Figure S45 a and b).
 156 Despite the limitations of our method in resolving a large magnitude range, our results consistently suggest a scaling
 157 closer to T^3 rather than T . This finding holds both in the time/magnitude space (Figure S45 a) and the log-log space
 158 (Figure S45 b).

159 We then use the Python PyMC solver (Abril-Pla et al., 2023) to explore a broader solution space and provide an
 160 uncertainty analysis of the estimated parameters. We set priors as uniform distributions bounded by $[0.1 - 10]$ for
 161 c and $[-35, 1000]$ for g . We examine 5.000.000 models to estimate the posterior distribution, giving a mean value for
 162 c of 4.99 ± 0.48 and g of 609 ± 400 , both with a 94% confidence interval (Figure S46). It is important to highlight that
 163 these results hold when categorizing the events as A (probables, Figures S47-S48) and B (possibles, Figures S49-S50).

164 Subsequently, we compare our results against published equations for scaling relationships. Gomberg et al. (2016)
 165 evaluates theoretical moment-duration scaling for spatially bounded and unbounded ruptures, whether slow or fast,
 166 considering the width of the region in which events occur (W_{max}), their stress drop ($\Delta\tau$) and their rupture velocity
 167 (V).

168 For a rupture with unbounded growth, rupture time scales with moment as

$$\log(T) = \frac{1}{3} \log(M_0) - \frac{1}{3} \log(c\Delta\tau V^3), \text{ for } M_0 < c\Delta\tau W_{max}^3. \quad (17)$$

169 For a rupture with a bounded growth, rupture time scales with moment as

$$\log(T) = \log(M_0) - \log(c\Delta\tau W_{max}^3), \text{ for } M_0 > c\Delta\tau W_{max}^3, \quad (18)$$

170 where c is a constant ($\frac{3\pi}{16}$), and M_0 the seismic moment. To draw the slow bounded and unbounded regions in Figure

174 6 in the main text, we assume a $\Delta\tau$ of 0.1 MPa, rupture velocities of 1 and 5 km/day, and a W_{max} of 30 km, a value
 175 inferred from geodetic and seismological observations (Chlieh et al., 2004; Comte et al., 2016). For the fast region
 176 case, we use $\Delta\tau$ values of 0.2 and 0.5 MPa, ruptures velocities of 1-2 km/s, and the same above-mentioned W_{max} .

177 It is worth noting that there are many factors that could affect the scaling estimates of our events. The detected
 178 events cover a very limited range of magnitudes (5.4-6.2), with considerable standard deviations for their durations.
 179 This could have an important impact on the estimation of the moment-duration scaling (Ide and Beroza, 2023). In
 180 addition, our method does not allow us to detect propagating events. Therefore, our events seem to be located more
 181 in the unbounded, crack-like region, rather than the pulsed, bounded ones. Taking all these constraints into account,
 182 we find that the seismic moment of our events in the Peru-Chile subduction region appears to have similar source
 183 properties that those observed in other subduction zones (Ide and Beroza, 2023, and reference therein). In addition,
 184 we provide a new database of slow slip events that can be used in global studies on this subject—a topic beyond the
 185 scope of the present manuscript.

186

187 **Text S5. PDF for coupling, depth, and Vp/Vs ratio**

188 **PDF of coupling.** We perform a statistical analysis to compare our coupling distribution with the detected events
 189 (see Figure 7a, b, c). This analysis involves comparing random values with those associated with our detected events.
 190 Our coupling model, illustrated in Figure 3 (main text), represents an average derived from 250,000 models. Initially,
 191 we selected 1000 random coupling models for the entire region, randomly sampling 24 points for each model (i.e. the
 192 number of detected events) to build the PDF of coupling at the location of SSEs if those were randomly distributed
 193 (see Figure S53a). We then compute the probability density function (PDF) of coupling at the location of our detected
 194 events. We approximate both PDFs using a Kernel Density Estimate (KDE). The analysis reveals that random values
 195 exhibit a distribution with a mean and standard deviation of 0.33 ± 0.35 (as shown by the gray line in Figure S53a).
 196 In contrast, for our detected events, we obtained $\mu \pm \sigma = 0.44 \pm 0.32$ (as indicated by the dark green line in Figure
 197 S53b).

198 Given the distinct resolution over the Peruvian and Chilean regions, we conduct a separate analysis for each region
 199 (Peru, latitude $>19^{\circ}\text{S}$, and Chile, latitude $\leq 19^{\circ}\text{S}$). In Peru, randomly sampled events yield coupling values with a mean
 200 and standard deviation of 0.2 ± 0.26 (gray line in Figure S53c), while our detections exhibit values of $\mu \pm \sigma = 0.24 \pm$
 201 0.2 (blue line in Figure S53d). For Chile, randomly sampled values are $\mu \pm \sigma = 0.37 \pm 0.36$ (gray line in Figure S53e),
 202 whereas our detections show values of $\mu \pm \sigma = 0.56 \pm 0.31$ (magenta line in Figure S53f).

203 Although the PDF are not definitive on that point, detected events in Chile tend to cluster in areas where coupling
 204 is average. While the results suggest a similar trend in the Peruvian region, the relationship is less clear. This potential
 205 disparity may stem from differences in data density between the regions (GNSS stations and InSAR in Chile, and just
 206 GNSS in Peru) and the sparse distribution of GNSS stations in Peru. It is important to highlight that these results hold
 207 when categorizing the events as A (probable, Figure S56 a, b, and c) and B (possible, Figure S57 a, b and c).

208 **PDF of Depths.** We perform a similar statistical analysis on the depth distribution of our detected events. To eliminate
 209 the possibility that the localization and clustering of our events result from chance, we compare our detections
 210 with events randomly distributed along the megathrust. Initially, we generate 10,000 sets of 24 random events to

211 build the PDF of depth of these random picks(Figure Sa). For detected events, we generate 10,000 locations for each
 212 detection drawn from a multivariate normal distribution $\mathbf{x} = \mathcal{N}_2(\mu_{le}, \sigma_{le}^2)$, assuming a normal error distribution for
 213 the event location. Here, μ_{le} is the event location (longitude and latitude), while σ_{le} is the standard deviation drawn
 214 from the covariance matrix of the synthetic event analysis.

215 Subsequently, for a detailed analysis, we computed PDFs and KDE of random values from depths shallower than
 216 60 km. This analysis relies on the fact that our events tend to occur at these depths. We repeat the same procedure
 217 used for the entire region, as well as the Chilean and Peruvian regions, for randomly distributed events (Figure S54
 218 b, e, h). Our results reveal distinct distributions between random events and actual locations. Random distributions
 219 exhibit either a highly flattened normal distribution across all depths or a nearly uniform distribution for depths ≤ 60
 220 km. In contrast, our detected events tend to cluster at depths corresponding to the transition zone (Chlieh et al., 2004;
 221 Comte et al., 2016). It is important to highlight that these results hold when categorizing the events as A (probable,
 222 Figure S56 d, e, and f) and B (possible, Figure S57 d, e, and f).

223 **PDF of Vp/Vs ratio.** We compare our results with the Vp/Vs ratio to explore a potential relationship with fluids.
 224 Fluids, a factor influencing the underlying physics of slow events (Jolivet and Frank, 2020, and references therein),
 225 can be inferred from estimates of Vp/Vs ratio (Comte et al., 2016, and references therein). Here, we use the Vp/Vs
 226 model by Comte et al. (2016) for northern Chile. From this model, we can derive a Vp/Vs ratio only for 17 of our
 227 events. First, we randomly sample 17 points in the Vp/Vs model 1000 times to build the PDF of Vp/Vs (Figure S55a,
 228 gray line). Second, we generate 1000 synthesized events for each detection using a multivariate normal distribution
 229 $\mathbf{x} = \mathcal{N}_2(\mu_{le}, \sigma_{le}^2)$, assuming a normally distributed event location. Here, μ_{le} signifies the event location (longitude
 230 and latitude), and σ_{le} is the covariance matrix based on the standard deviation of each event obtained during the
 231 synthesized event analysis. It is important to highlight that these results hold when categorizing the events as A
 232 (probable, Figure S56 g) and B (possible, Figure S57 g).

233 These results suggest that the observed distributions are not significantly distinct. One plausible explanation is
 234 that our events may occur in regions devoid of a permanent fluid source, as indicated by the Vp/Vs ratio mapping.
 235 However, this does not preclude the possibility of rapid fluid migrations contributing to event generation (Contreras-
 236 Reyes et al., 2021; Bouchon et al., 2023) or an aseismic response induced by pore pressure waves (Cruz-Atienza et al.,
 237 2018). Both hypotheses require further investigation and are beyond the scope of this manuscript.

238

239 **Text S6. Aseismic slip and gravity model**

240 We contrast our results with a 3D gravity model in the (Tassara and Echaurren, 2012) zone to compare our results
 241 with large tectonic structures and their possible relationship to fluids. We project the detected events onto trench
 242 perpendicular cross sections. We then project the uncertainties associated with these detections on the cross sec-
 243 tions. To consider an uncertainty analysis on the depth of our events, we employ a multivariate normal distribution
 244 $\{\mathbf{x}\} = \mathcal{N}_2(\mu_{le}, \sigma_{le}^2)$, assuming that the event location is normally distributed. Here, μ_{le} corresponds to the event
 245 location, while σ_{le} is the covariance matrix of the location, which is based on the standard deviation of each event
 246 obtained during the synthetic analysis. We project these uncertainties on the megathrust and show the extent of the
 247 regions in which the detected event could be located (cyan lines in Figure S51).

248 References

- 249 Abril-Pla, O., Andreani, V., Carroll, C., Dong, L., Fonnesbeck, C. J., Kochurov, M., Kumar, R., Lao, J., Luhmann, C. C., Martin, O. A., Osthege,
250 M., Vieira, R., Wiecki, T., and Zinkov, R. PyMC: a modern, and comprehensive probabilistic programming framework in Python. *PeerJ
Computer Science*, 9:e1516, 2023. doi: 10.7717/peerj-cs.1516.
- 252 Bevis, M. and Brown, A. Trajectory models and reference frames for crustal motion geodesy. *Journal of Geodesy*, 88(3):283–311, 3 2014.
253 doi: 10.1007/s00190-013-0685-5.
- 254 Bock, Y. and Melgar, D. Physical applications of GPS geodesy: A review. *Reports on Progress in Physics*, 79(10):106801, 2016.
255 doi: 10.1088/0034-4885/79/10/106801.
- 256 Bouchon, M., Guillot, S., Marsan, D., Socquet, A., Jara, J., and Renard, F. Observation of a Synchronicity between Shallow and Deep Seis-
257 mic Activities during the Foreshock Crisis Preceding the Iquique Megathrust Earthquake. *Seismica*, 2(2), 10 2023. doi: 10.26443/seis-
258 mica.v2i2.849.
- 259 Chlieh, M., De Chabalier, J. B., Ruegg, J. C., Armijo, R., Dmowska, R., Campos, J., and Feigl, K. L. Crustal deformation and fault slip during the
260 seismic cycle in the North Chile subduction zone, from GPS and InSAR observations. *Geophysical Journal International*, 158(2):695–711,
261 2004. doi: 10.1111/j.1365-246X.2004.02326.x.
- 262 Comte, D., Carrizo, D., Roecker, S., Ortega-Culaciati, F., and Peyrat, S. Three-dimensional elastic wave speeds in the northern Chile
263 subduction zone: Variations in hydration in the supraslab mantle. *Geophysical Journal International*, 207(2):1080–1105, 2016.
264 doi: 10.1093/gji/ggw318.
- 265 Contreras-Reyes, E., Díaz, D., Bello-González, J. P., Slezak, K., Potin, B., Comte, D., Maksymowicz, A., Ruiz, J. A., Osses, A., and Ruiz, S.
266 Subduction zone fluids and arc magmas conducted by lithospheric deformed regions beneath the central Andes. *Scientific Reports*, 11
267 (1):1–12, 2021. doi: 10.1038/s41598-021-02430-9.
- 268 Cruz-Atienza, V. M., Villafuerte, C., and Bhat, H. S. Rapid tremor migration and pore-pressure waves in subduction zones. *Nature Commu-
269 nications*, 9(1), 2018. doi: 10.1038/s41467-018-05150-3.
- 270 Gomberg, J., Wech, A., Creager, K., Obara, K., and Agnew, D. Reconsidering earthquake scaling. *Geophysical Research Letters*, 43(12):
271 6243–6251, 6 2016. doi: 10.1002/2016GL069967.
- 272 Ide, S. and Beroza, G. C. Slow earthquake scaling reconsidered as a boundary between distinct modes of rupture propagation. *Proceedings
273 of the National Academy of Sciences*, 120(32):2017, 8 2023. doi: 10.1073/pnas.2222102120.
- 274 International Seismological Centre. On-line Bulletin, 2016.
- 275 Jolivet, R. and Frank, W. B. The Transient and Intermittent Nature of Slow Slip. *AGU Advances*, 1(1), 2020. doi: 10.1029/2019av000126.
- 276 Michel, S., Gualandi, A., and Avouac, J.-P. Similar scaling laws for earthquakes and Cascadia slow-slip events. *Nature*, 574(7779):522–526,
277 10 2019. doi: 10.1038/s41586-019-1673-6.
- 278 Nocquet, J. M., Villegas-Lanza, J. C., Chlieh, M., Mothes, P. A., Rolandone, F., Jarrin, P., Cisneros, D., Alvarado, A., Audin, L., Bondoux, F.,
279 Martin, X., Font, Y., Régnier, M., Vallée, M., Tran, T., Beauval, C., Maguiña Mendoza, J. M., Martinez, W., Tavera, H., and Yepes, H. Motion of
280 continental slivers and creeping subduction in the northern Andes. *Nature Geoscience*, 7(4):287–291, 2014. doi: 10.1038/ngeo2099.
- 281 Rousset, B., Campillo, M., Lasserre, C., Frank, W. B., Cotte, N., Walpersdorf, A., Socquet, A., and Kostoglodov, V. A geodetic matched filter
282 search for slow slip with application to the Mexico subduction zone. *Journal of Geophysical Research: Solid Earth*, 122(12):498–10, 12
283 2017. doi: 10.1002/2017JB014448.
- 284 Rousset, B., Bürgmann, R., and Campillo, M. Slow slip events in the roots of the San Andreas fault. *Science Advances*, 5(2):eaav3274, 2 2019.
285 doi: 10.1126/sciadv.aav3274.

- 286 Segall, P. Earthquake and volcano deformation. *Choice Reviews Online*, 48(01):48–0287, 9 2010. doi: 10.5860/CHOICE.48-0287.
- 287 Tassara, A. and Echaurren, A. Anatomy of the Andean subduction zone: three-dimensional density model upgraded and compared against
288 global-scale models. *Geophysical Journal International*, 189(1):161–168, 4 2012. doi: 10.1111/j.1365-246X.2012.05397.x.
- 289 Virtanen, P., Gommers, R., Oliphant, T. E., Haberland, M., Reddy, T., Cournapeau, D., Burovski, E., Peterson, P., Weckesser, W., Bright, J.,
290 van der Walt, S. J., Brett, M., Wilson, J., Millman, K. J., Mayorov, N., Nelson, A. R. J., Jones, E., Kern, R., Larson, E., Carey, C. J., Polat, I.,
291 Feng, Y., Moore, E. W., VanderPlas, J., Laxalde, D., Perktold, J., Cimrman, R., Henriksen, I., Quintero, E. A., Harris, C. R., Archibald, A. M.,
292 Ribeiro, A. H., Pedregosa, F., van Mulbregt, P., Vijaykumar, A., Bardelli, A. P., Rothberg, A., Hilboll, A., Kloeckner, A., Scopatz, A., Lee, A.,
293 Rokem, A., Woods, C. N., Fulton, C., Masson, C., Häggström, C., Fitzgerald, C., Nicholson, D. A., Hagen, D. R., Pasechnik, D. V., Olivetti, E.,
294 Martin, E., Wieser, E., Silva, F., Lenders, F., Wilhelm, F., Young, G., Price, G. A., Ingold, G.-L., Allen, G. E., Lee, G. R., Audren, H., Probst, I.,
295 Dietrich, J. P., Silterra, J., Webber, J. T., Slavič, J., Nothman, J., Buchner, J., Kulick, J., Schönberger, J. L., de Miranda Cardoso, J. V., Reimer,
296 J., Harrington, J., Rodríguez, J. L. C., Nunez-Iglesias, J., Kuczynski, J., Tritz, K., Thoma, M., Newville, M., Kümmeler, M., Bolingbroke, M.,
297 Tartre, M., Pak, M., Smith, N. J., Nowaczyk, N., Shebanov, N., Pavlyk, O., Brodtkorb, P. A., Lee, P., McGibbon, R. T., Feldbauer, R., Lewis,
298 S., Tygier, S., Sievert, S., Vigna, S., Peterson, S., More, S., Pudlik, T., Oshima, T., Pingel, T. J., Robitaille, T. P., Spura, T., Jones, T. R., Cera,
299 T., Leslie, T., Zito, T., Krauss, T., Upadhyay, U., Halchenko, Y. O., and Vázquez-Baeza, Y. SciPy 1.0: fundamental algorithms for scientific
300 computing in Python. *Nature Methods*, 17(3):261–272, 3 2020. doi: 10.1038/s41592-019-0686-2.
- 301 Wdowinski, S., Bock, Y., Zhang, J., Fang, P., and Genrich, J. Southern California permanent GPS geodetic array: Spatial filtering of daily
302 positions for estimating coseismic and postseismic displacements induced by the 1992 Landers earthquake. *Journal of Geophysical
303 Research: Solid Earth*, 102(B8):18057–18070, 1997. doi: 10.1029/97jb01378.
- 304 Williams, S. D. P. The effect of coloured noise on the uncertainties of rates estimated from geodetic time series. *Journal of Geodesy*, 76
305 (9-10):483–494, 2003. doi: 10.1007/s00190-002-0283-4.
- 306 Williams, S. D. P., Bock, Y., Fang, P., Jamason, P., Nikolaidis, R. M., Prawirodirdjo, L., Miller, M., and Johnson, D. J. Error analysis of continuous
307 GPS position time series. *Journal of Geophysical Research-Solid Earth*, 109(B3):B03412, 2003. doi: 10.1029/2003JB002741.

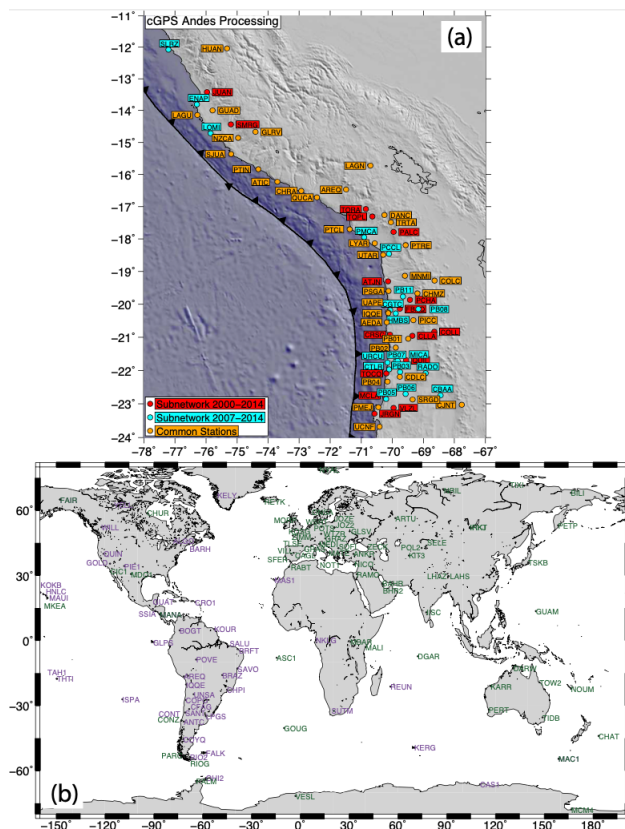


Figure S1. (a) 2 local subnetworks of cGPS in map view (Andes 2000-2014 in red and Andes 2007-2014 in cyan). Orange dots are the common stations in both networks. (b) Global GPS network processed. Green names denotes IGS stations included in the Global processing, while purple ones indicate IGS stations overlapping with the Andean subnetworks.

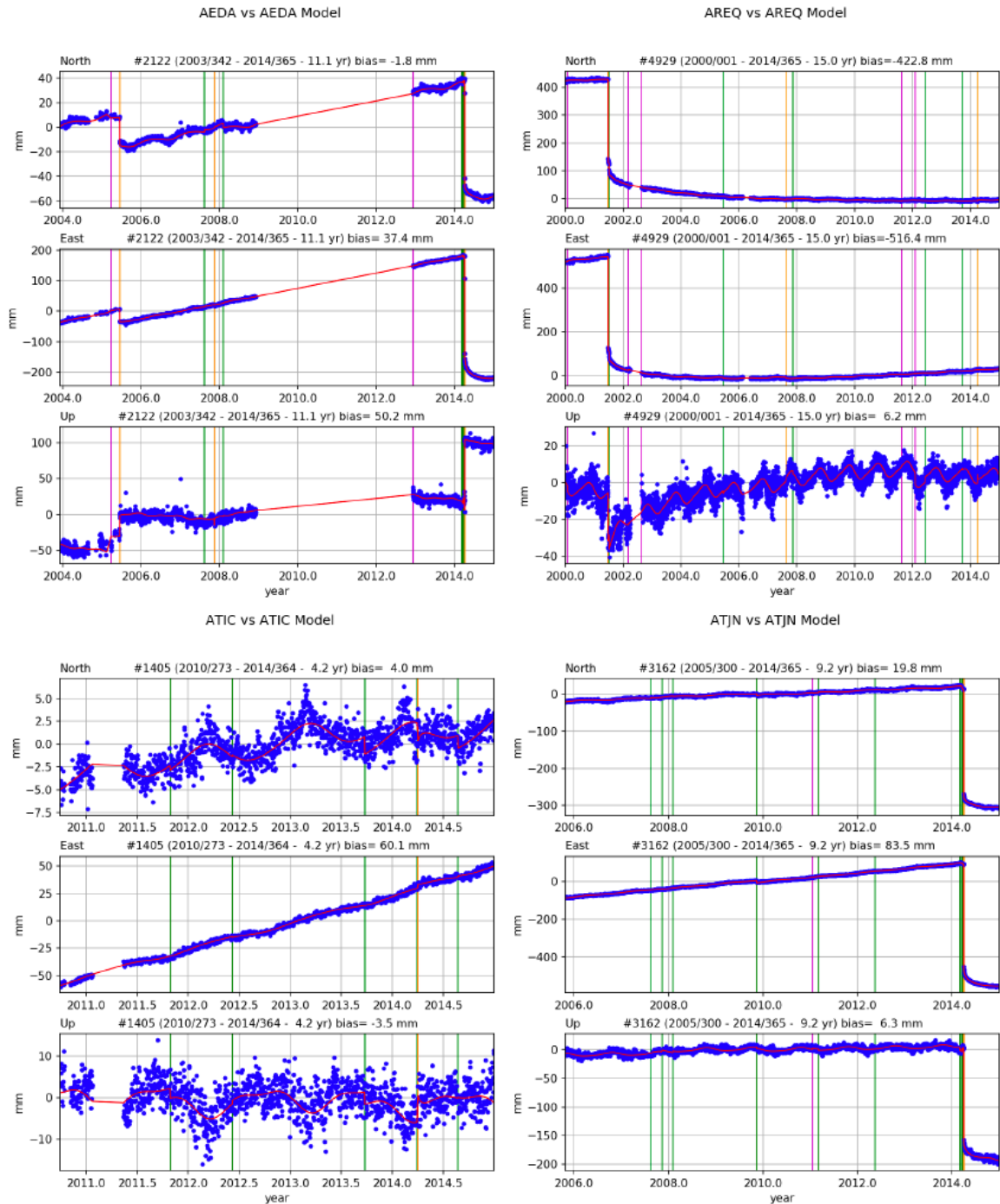


Figure S2. Daily Displacement Time Series (blue dots) and its best-fit trajectory model (red curves) for AEDA, AREQ, ATIC and ATJN stations. Purple vertical lines denote the antenna changes, orange vertical lines are earthquake with $M \geq 7.5$ (for which post-seismic signal is modeled), while green vertical lines represent the earthquakes $6.0 \leq M < 7.5$.

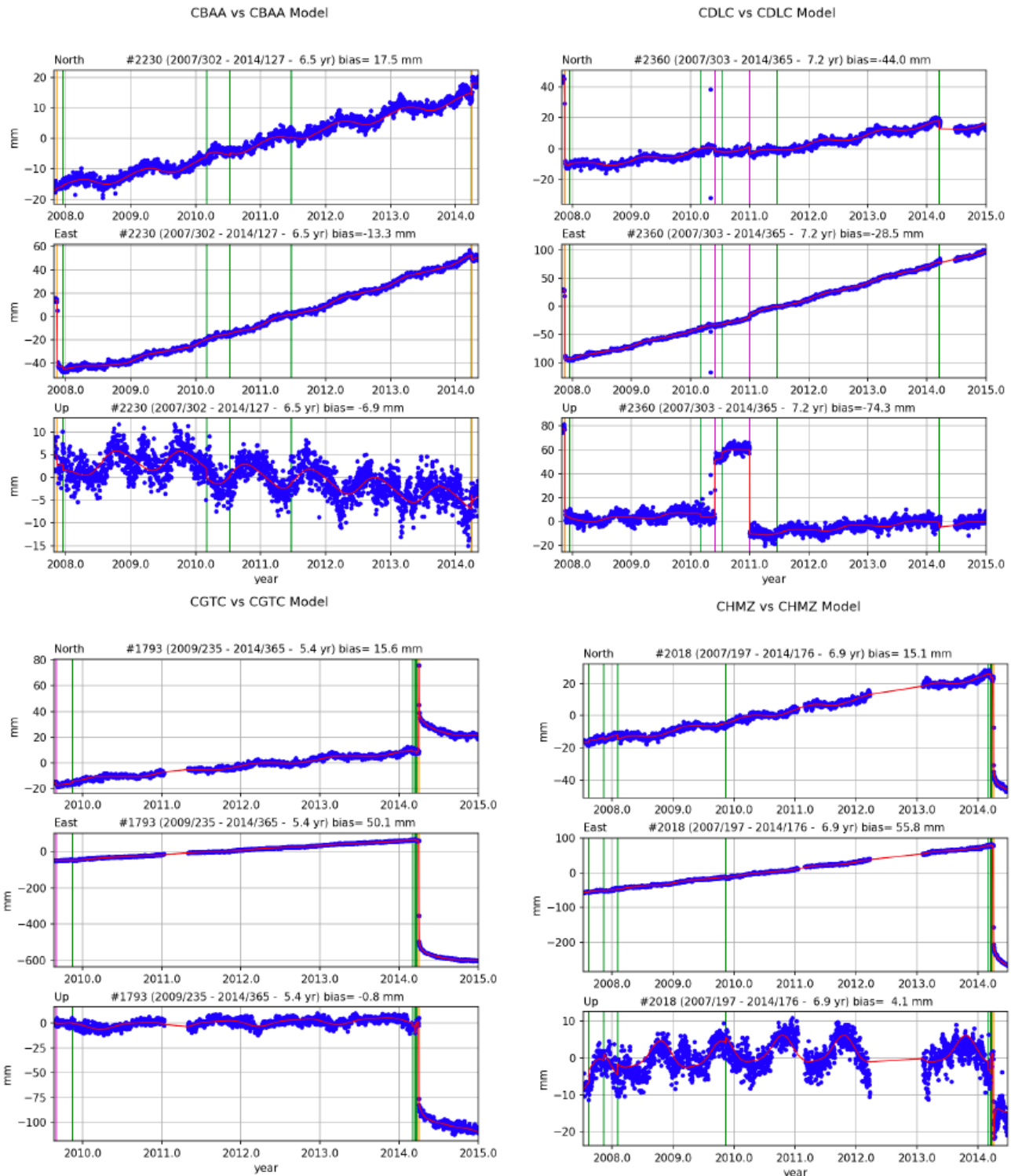


Figure S3. Same caption as in Figure S2, but for CBAA, CDLC, CGTC and CHMZ stations.

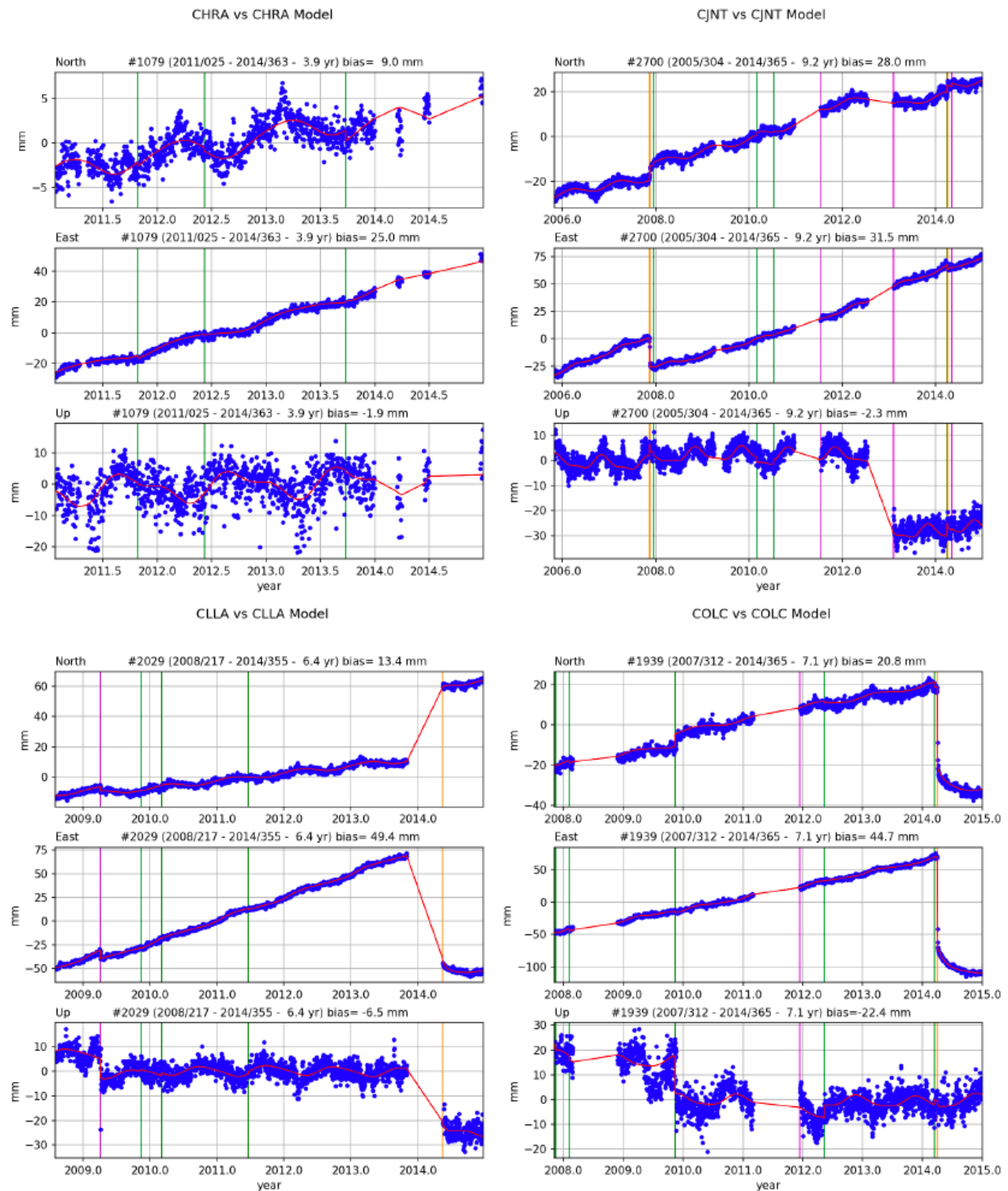


Figure S4. Same caption as in Figure S2, but for CHRA, CJNT, CLLA and COLC stations.

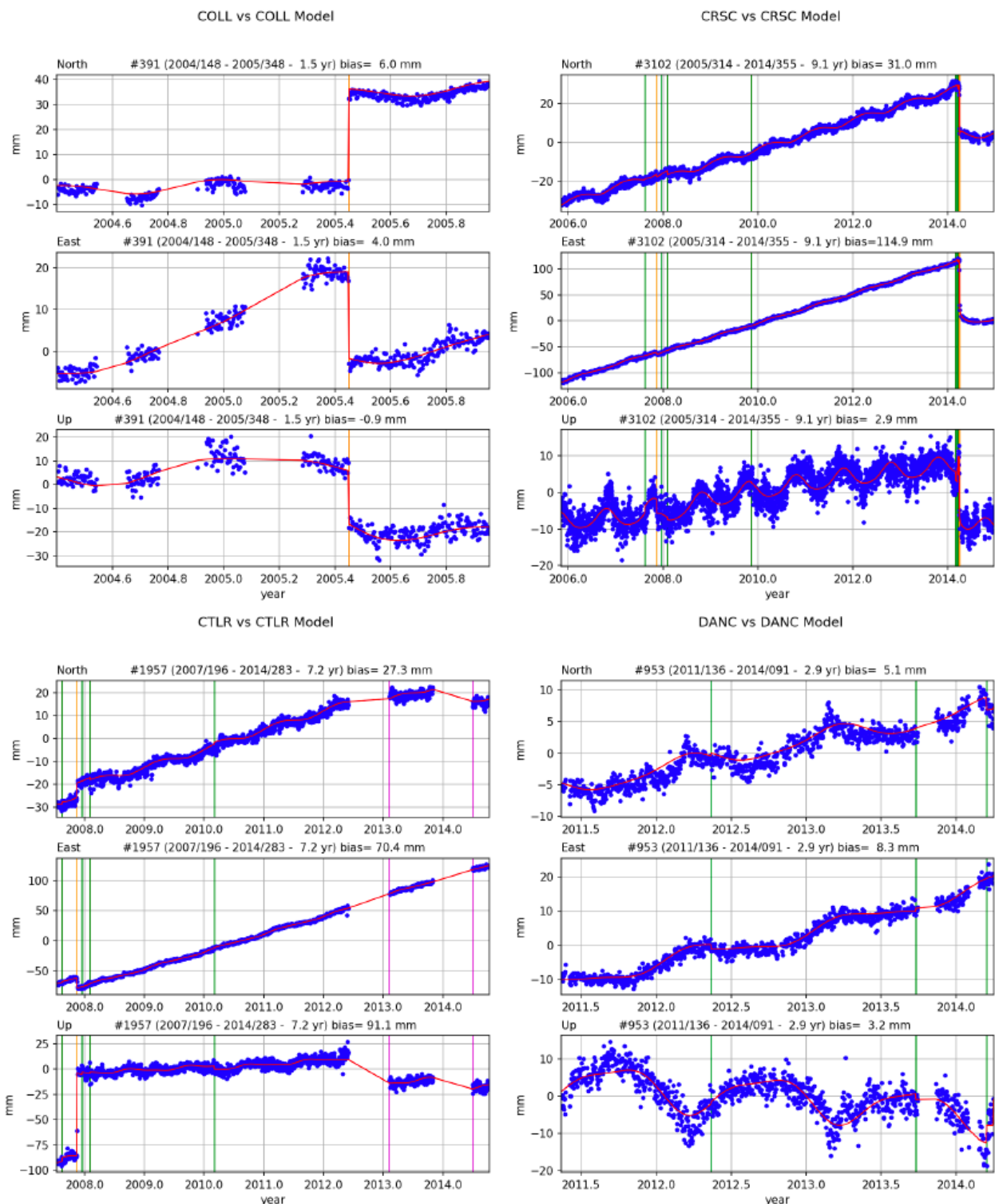


Figure S5. Same caption as in Figure S2, but for COLL, CRSC, CTLR and DANC stations.

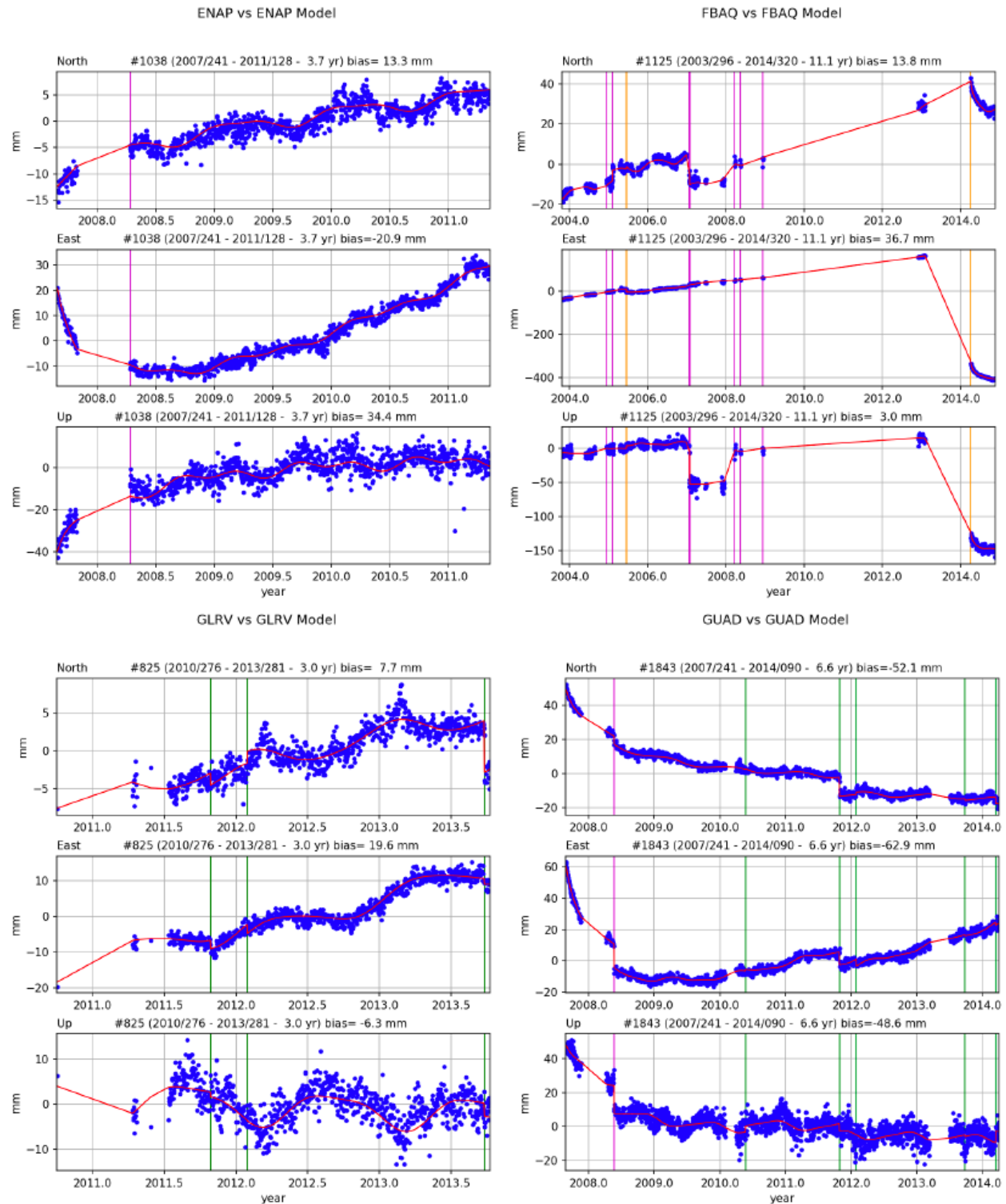


Figure S6. Same caption as in Figure S2, but for ENAP, FBAQ, GLRV and GUAD stations.

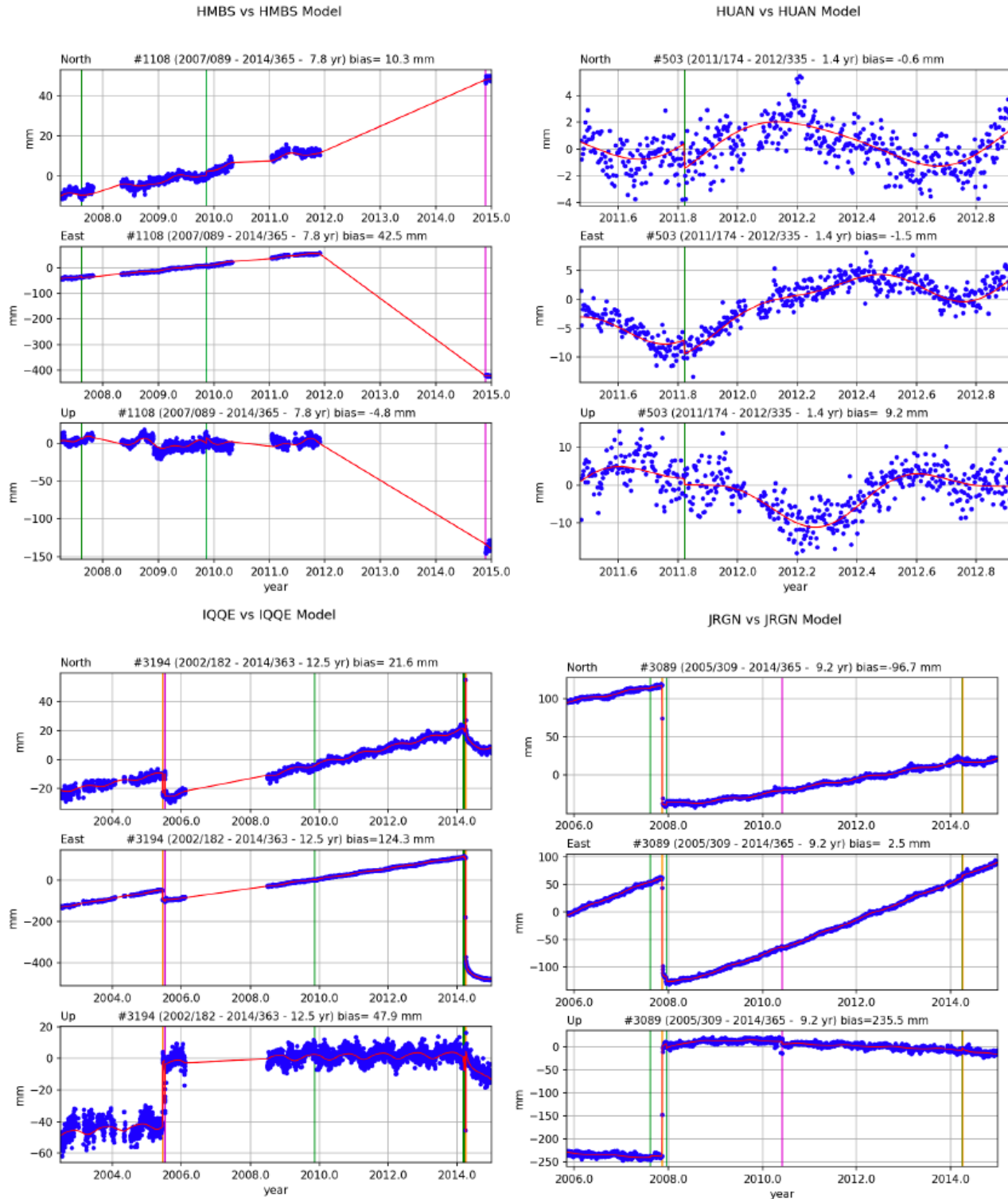


Figure S7. Same caption as in Figure S2, but for HMBS, HUAN, IQQE and JRGN stations.

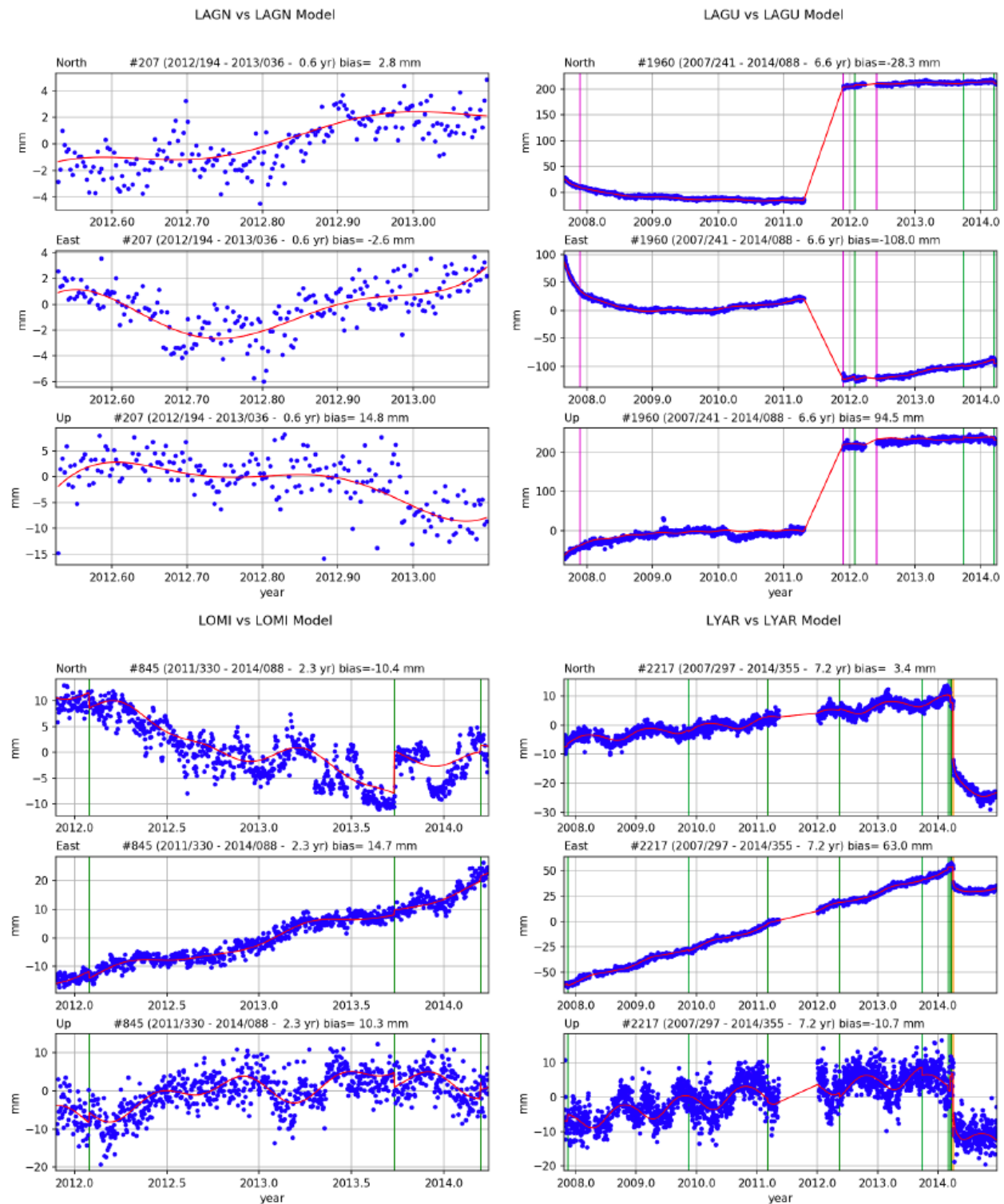


Figure S8. Same caption as in Figure S2, but for LAGN, LAGU, LOMI and LYAR stations.

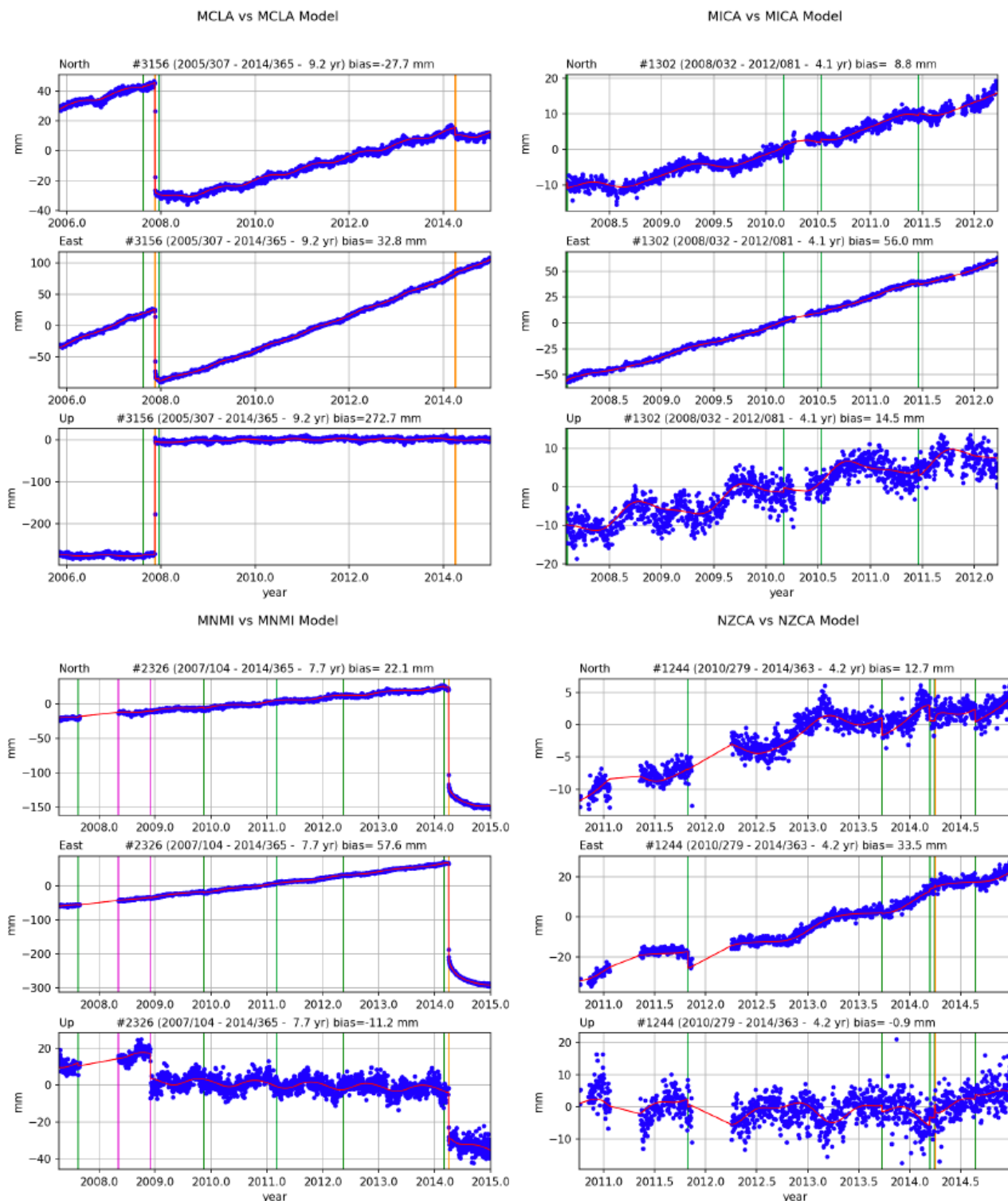


Figure S9. Same caption as in Figure S2, but for MCLA, MICA, MNMI and NZCA stations.

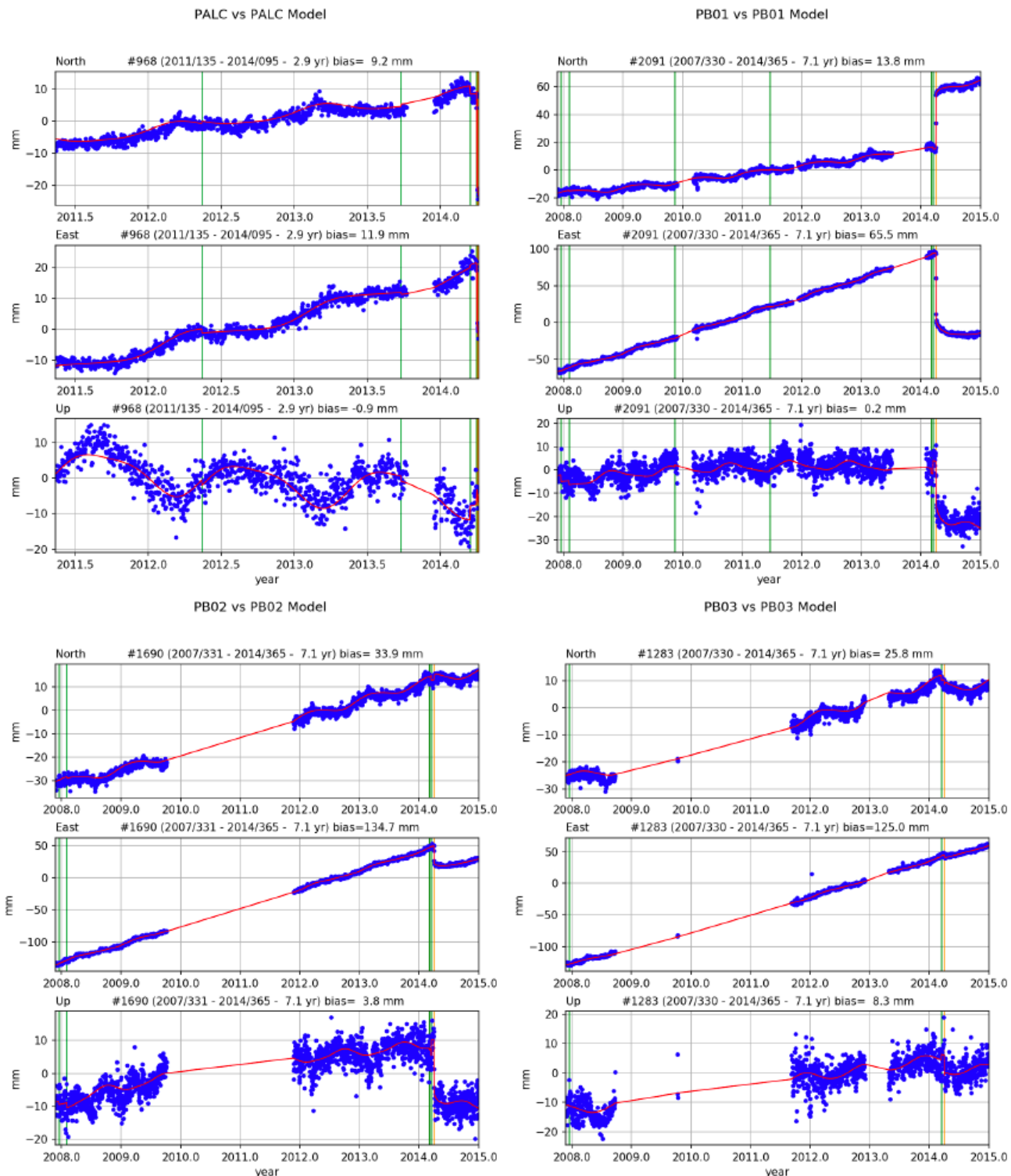


Figure S10. Same caption as in Figure S2, but for PALC, PB01, PB02 and PB03 stations.

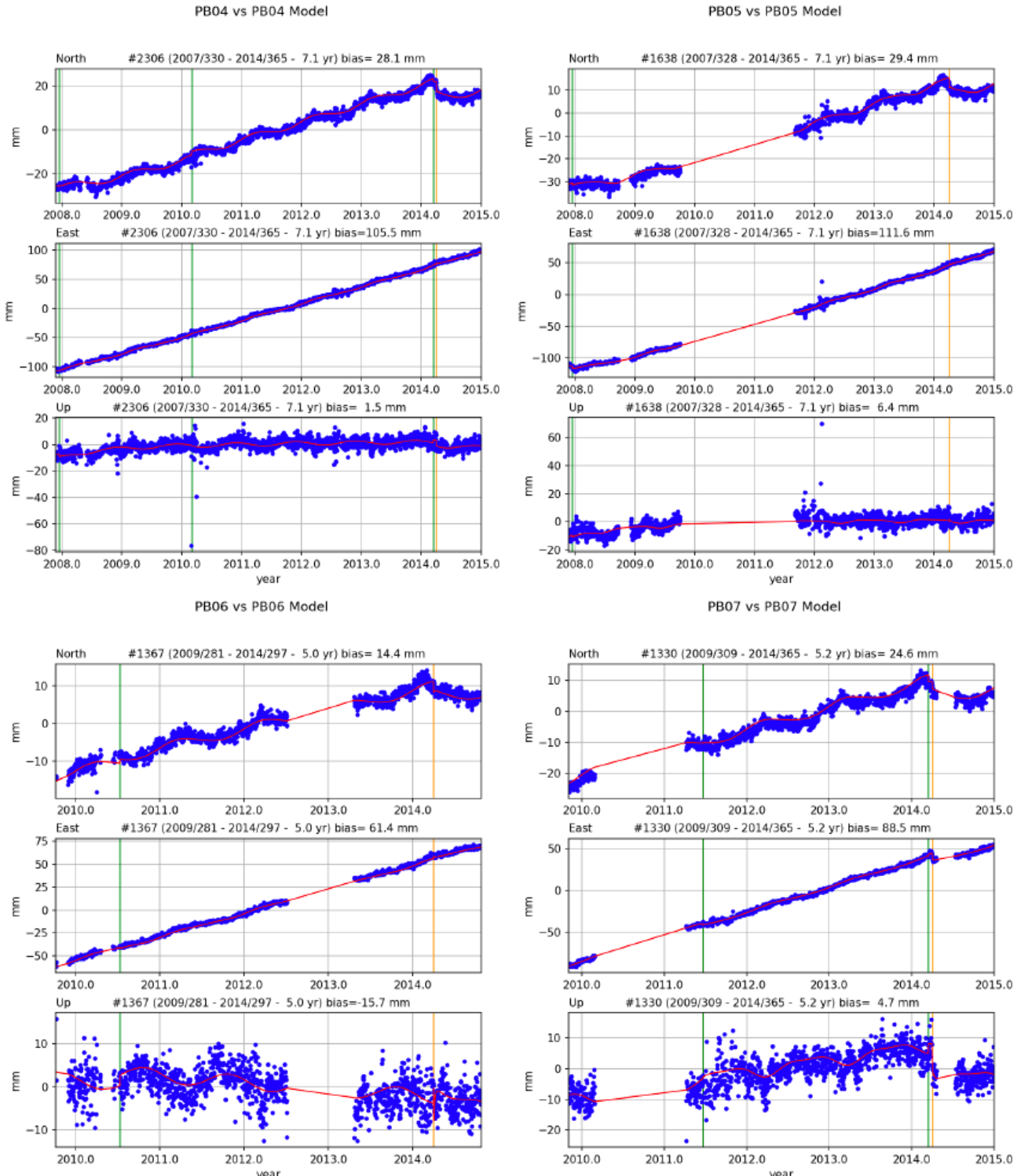


Figure S11. Same caption as in Figure S2, but for PB04, PB05, PB06 and PB07 stations.

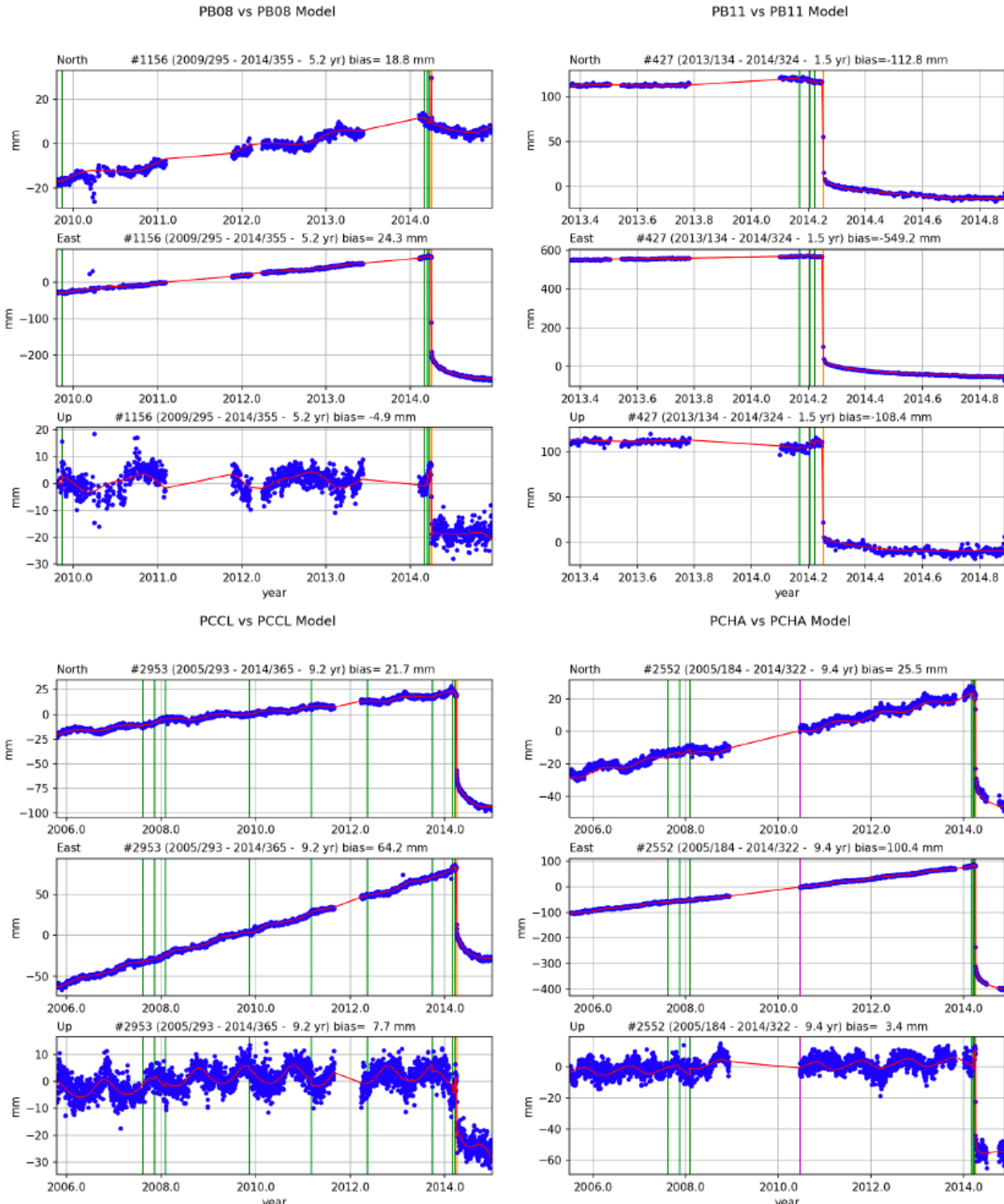


Figure S12. Same caption as in Figure S2, but for PB08, PB11, PCCL and PCHA stations.

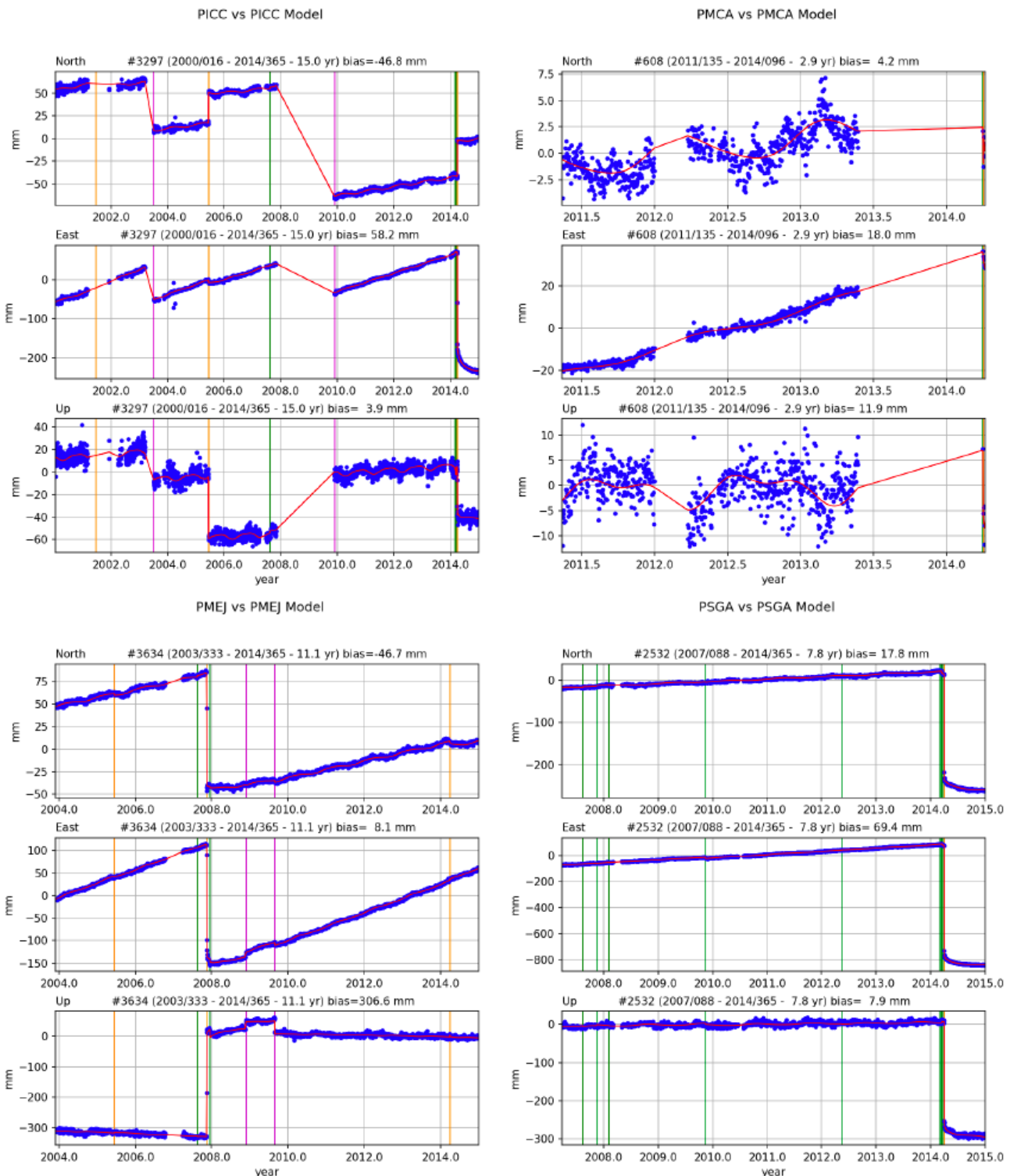


Figure S13. Same caption as in Figure S2, but for PICC, PMCA, PMEJ and PSGA stations.

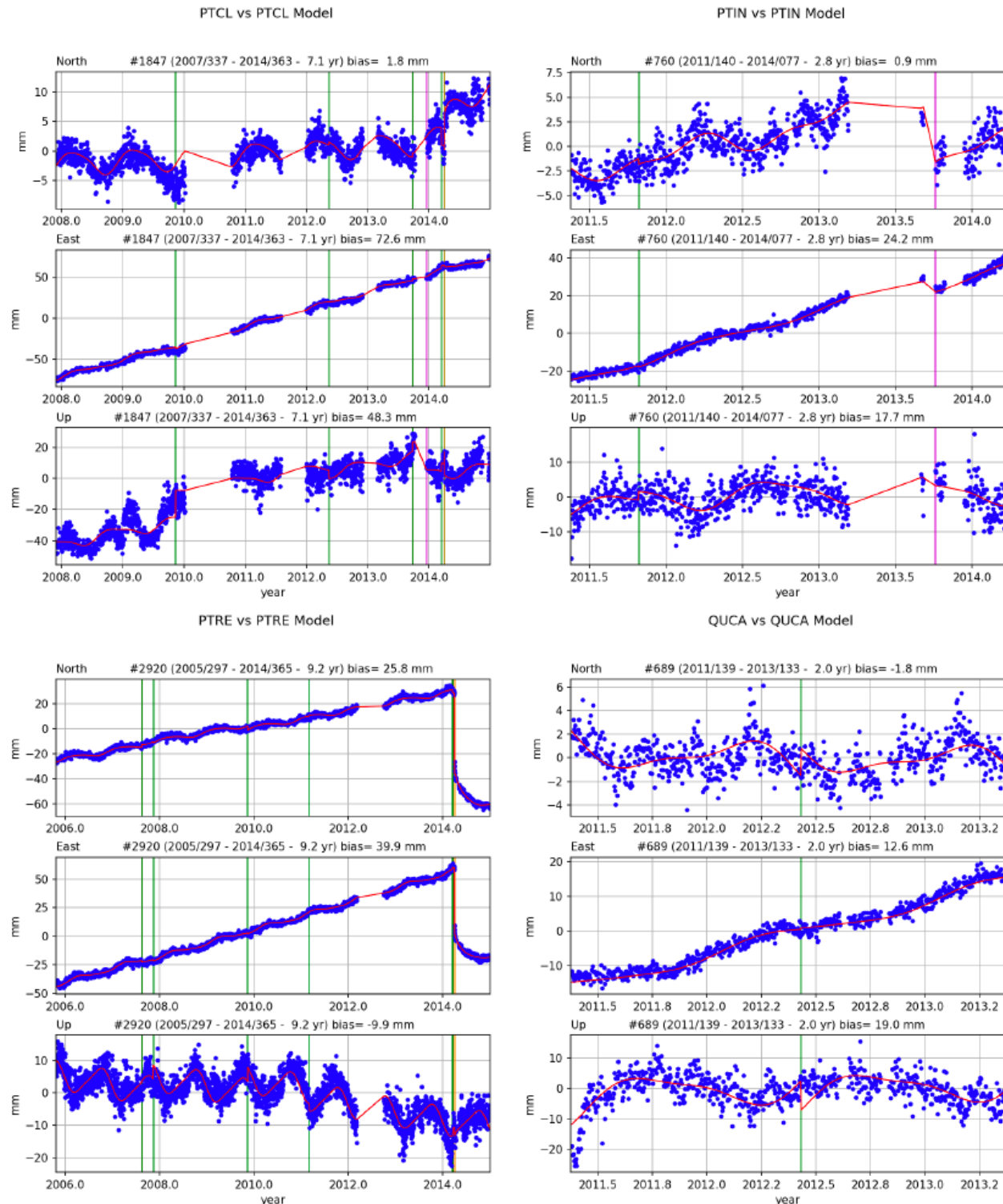


Figure S14. Same caption as in Figure S2, but for PTCL, PTIN, PTRE and QUCA stations.

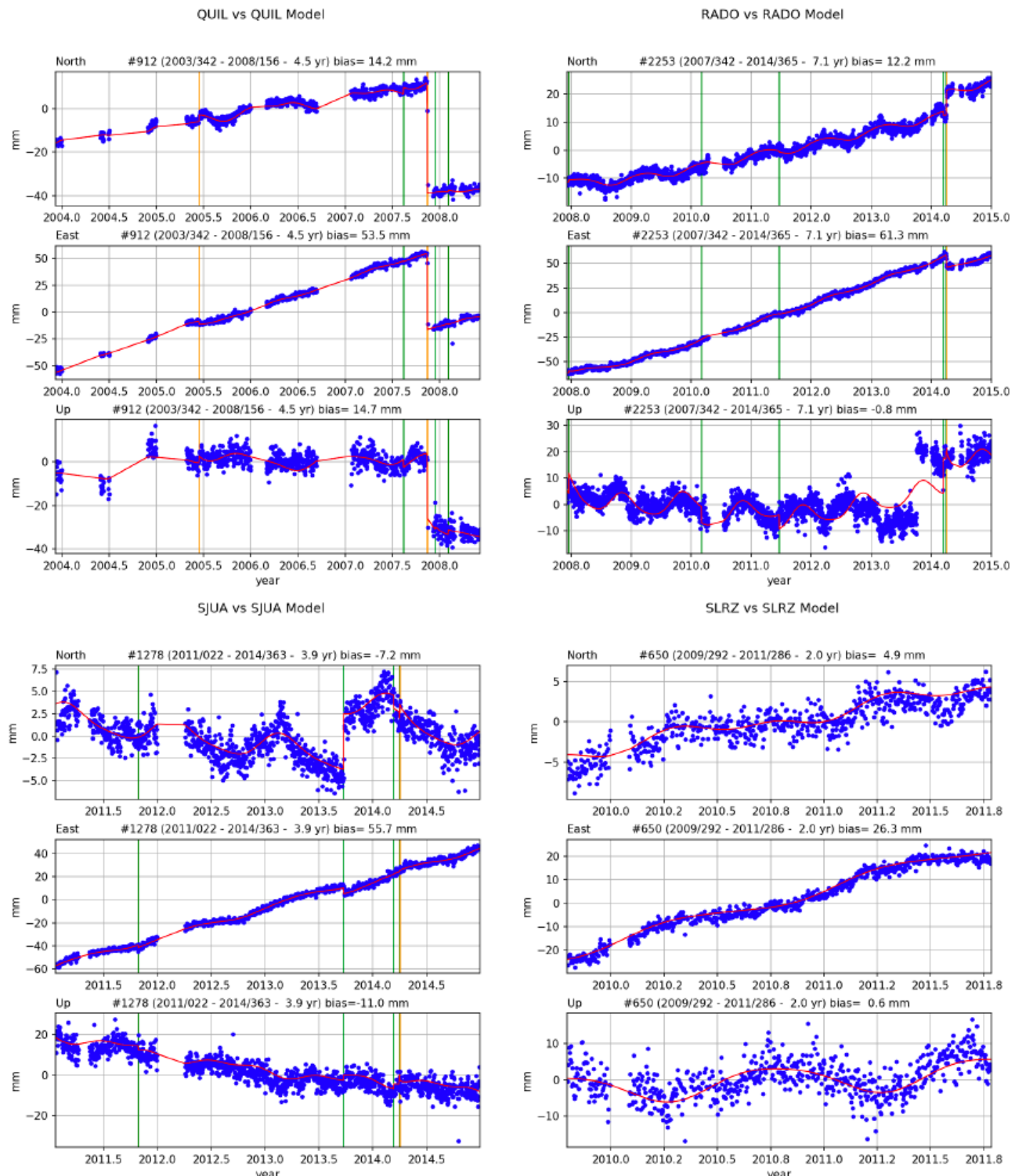


Figure S15. Same caption as in Figure S2, but for QUIL, RADO, SJUA and SLRZ stations.

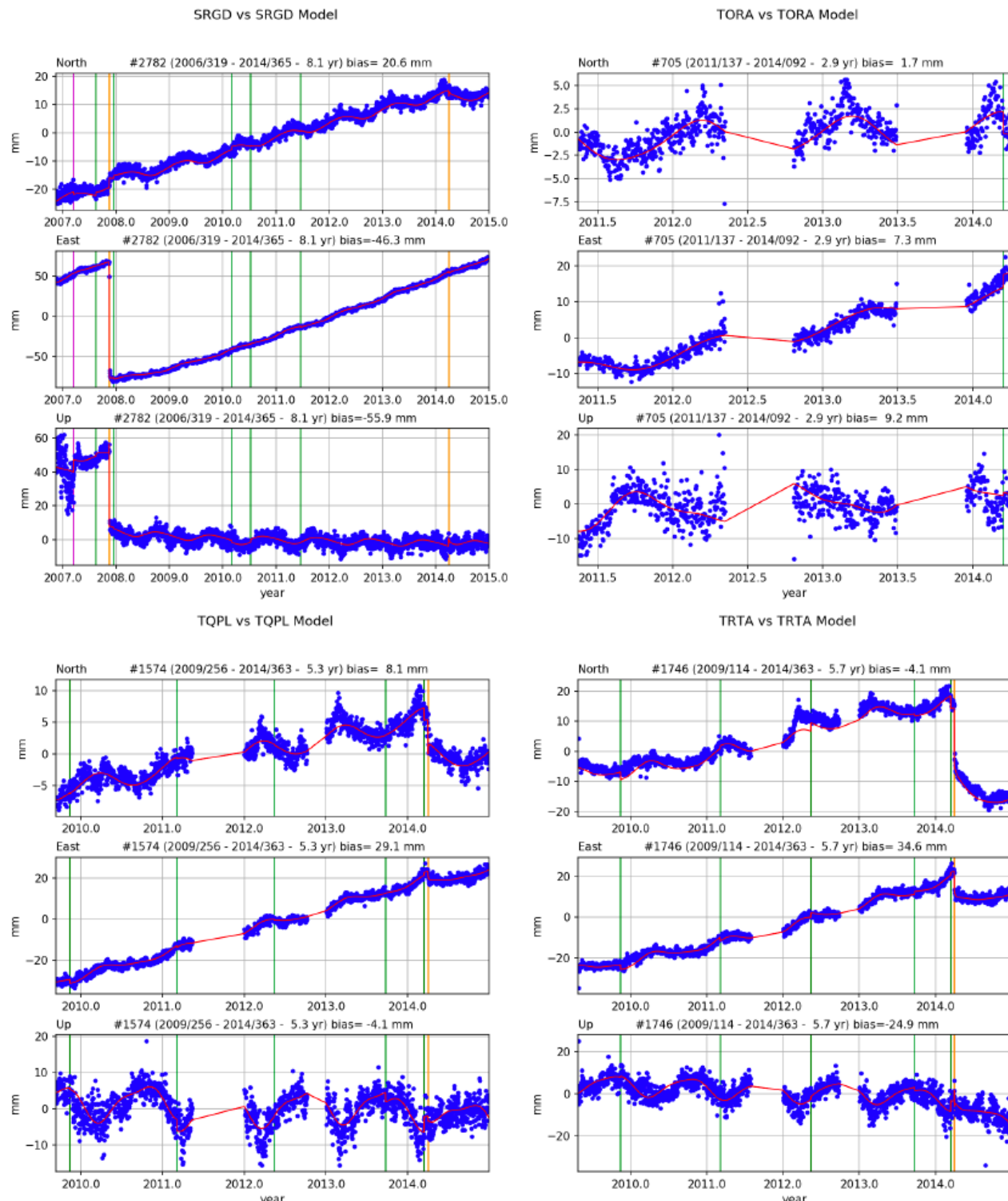


Figure S16. Same caption as in Figure S2, but for UAPE, UCNF, UTAR and VLZL stations.

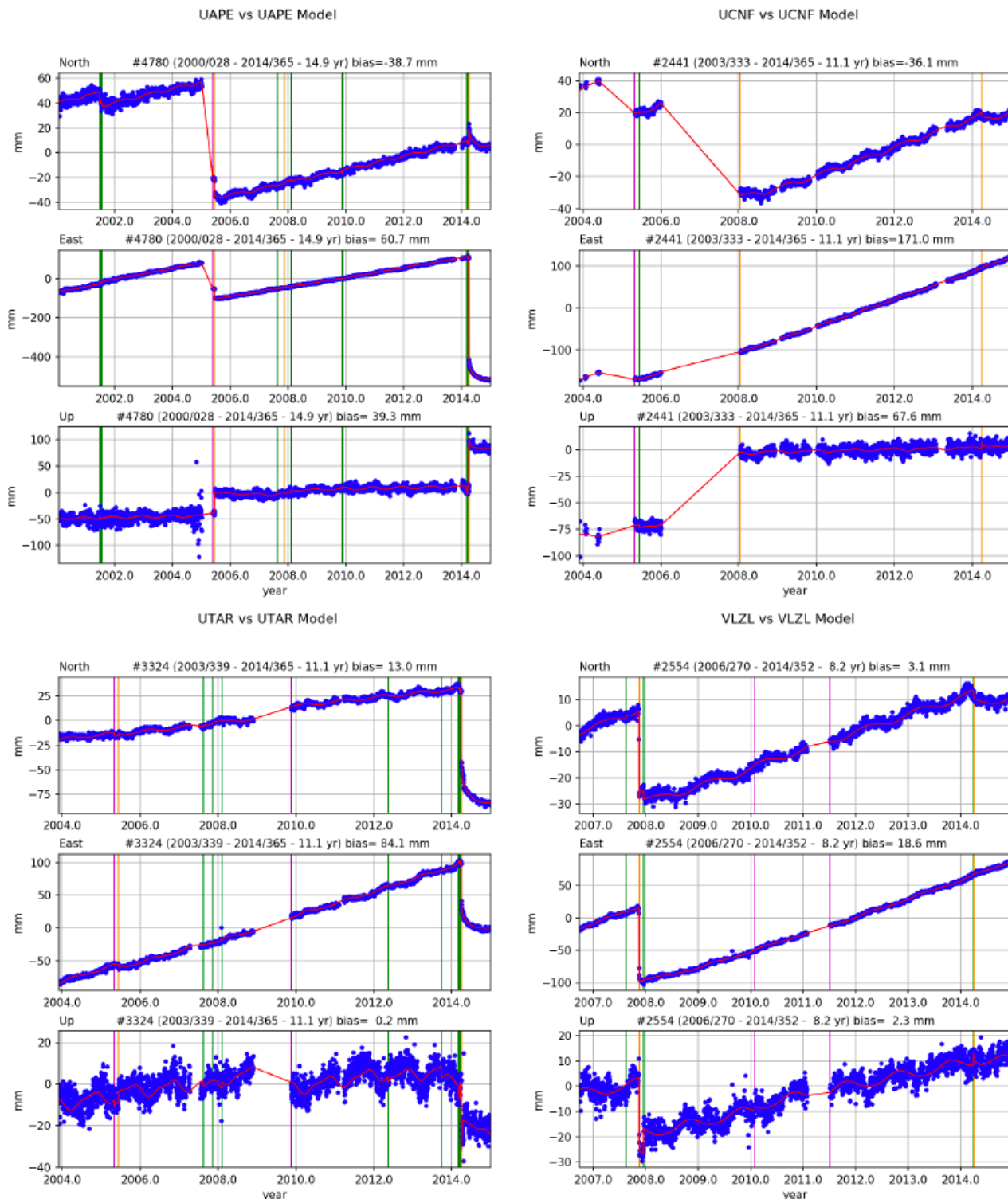


Figure S17. Same caption as in Figure S2, but for UAPE, UCNF, UTAR and VLZL stations.

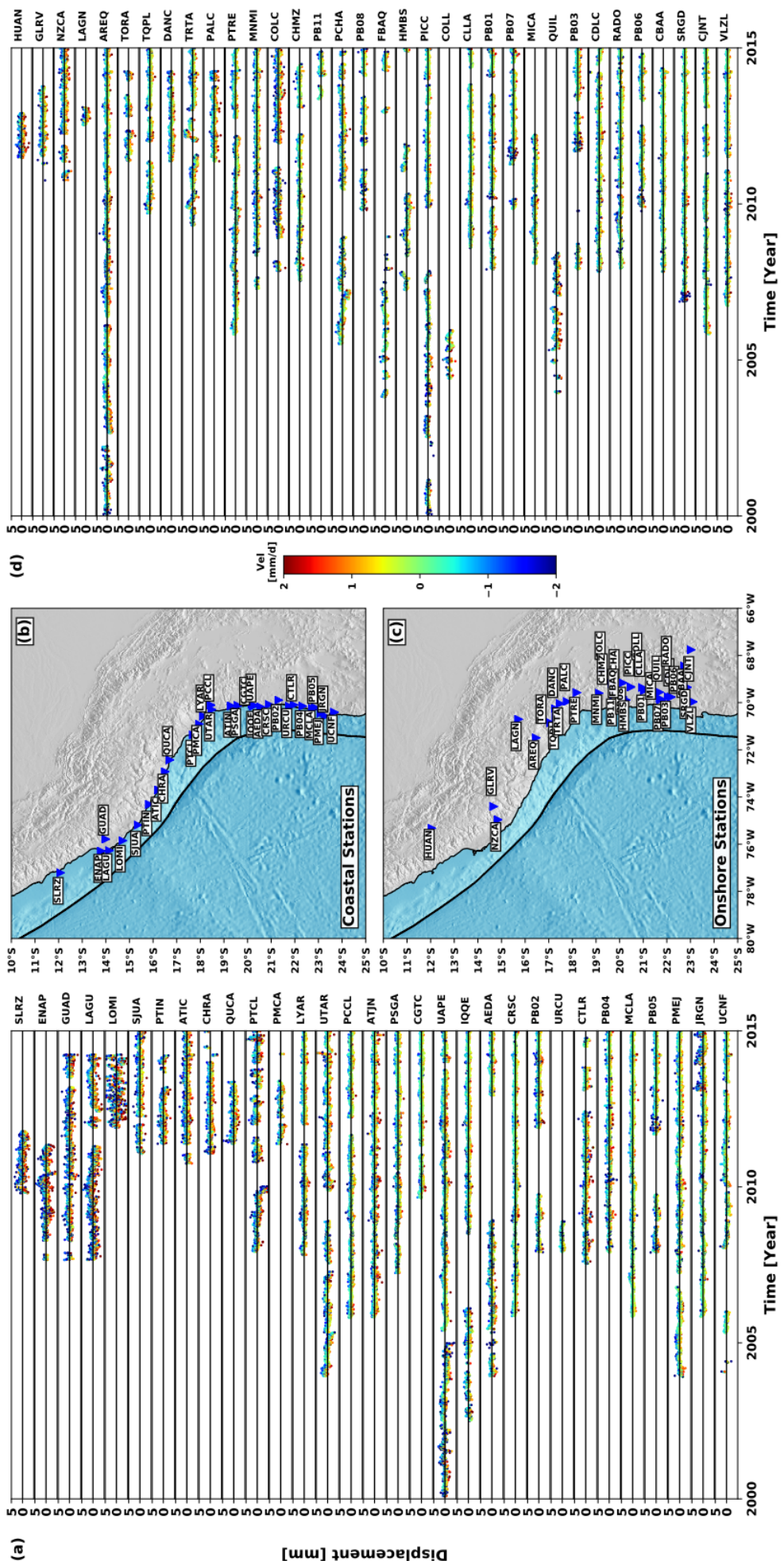


Figure S18. (a) North residuals displacement time series for the coastal stations, color-coded with the daily velocity. (b) Map of cPGS location for the coastal stations. (c) Map of cGPS location for inland stations. (d) Same than (a) but for inland stations.

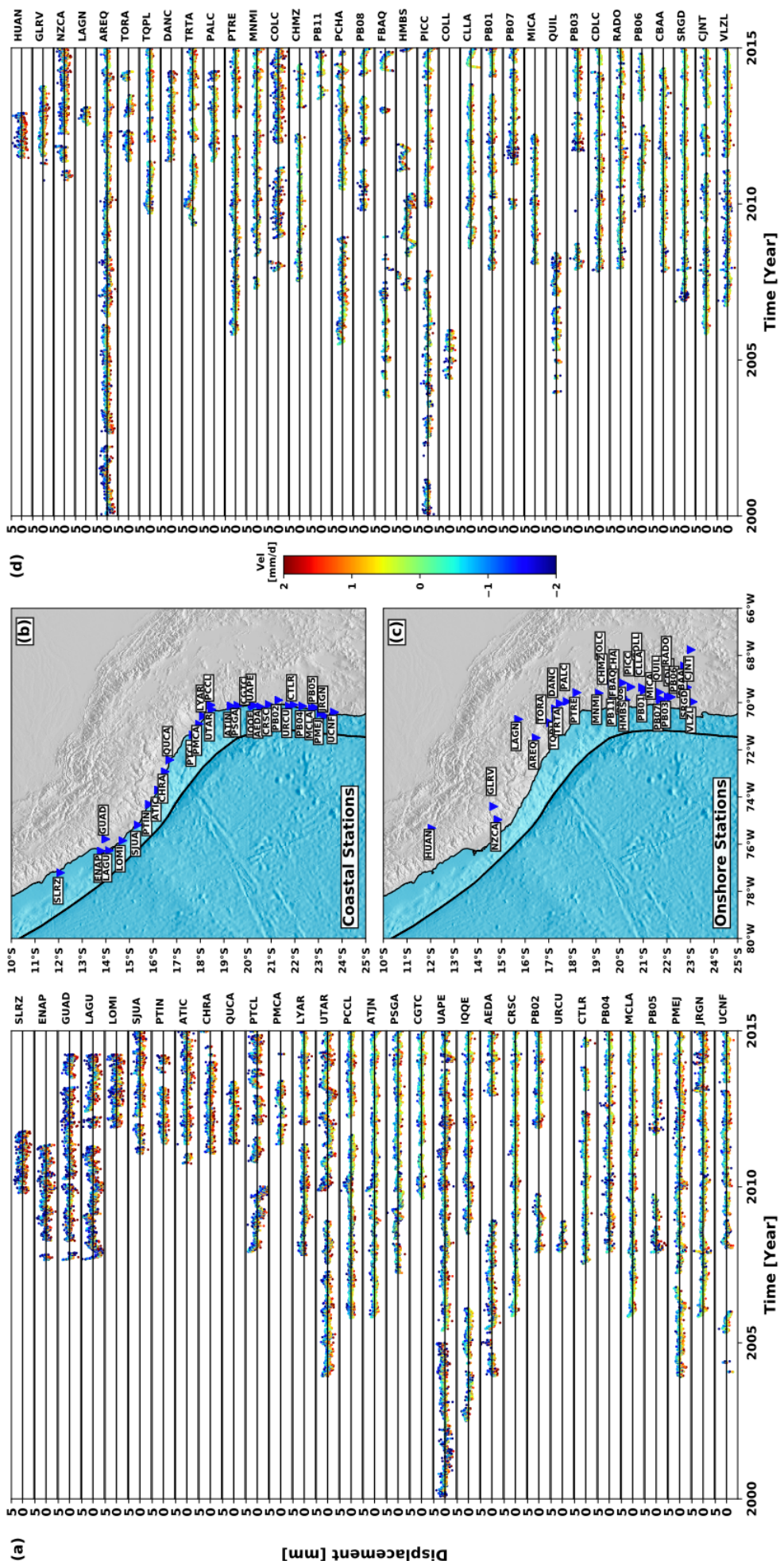


Figure S19. (a) East residuals displacement time series for the coastal stations, color-coded with the daily velocity. (b) Map of cPGS location for the coastal stations. (c) Map of cPGS location for inland stations. (d) Same than (a) but for inland stations.

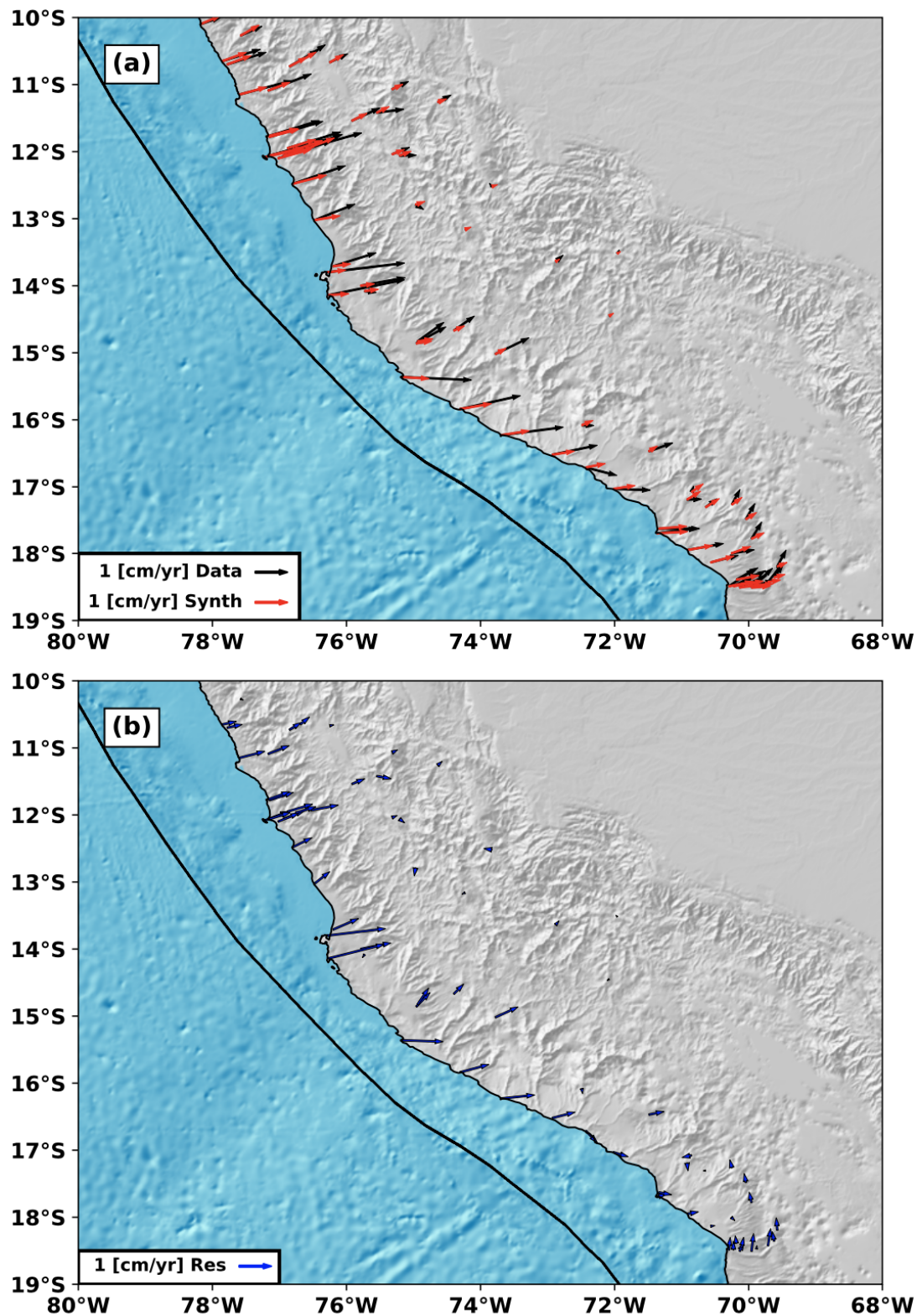


Figure S20. (a) Data (black arrows) and mean model (red arrows) for GNSS data in Peru. (b) Residuals, defined as data minus predictions, are shown in dark blue.

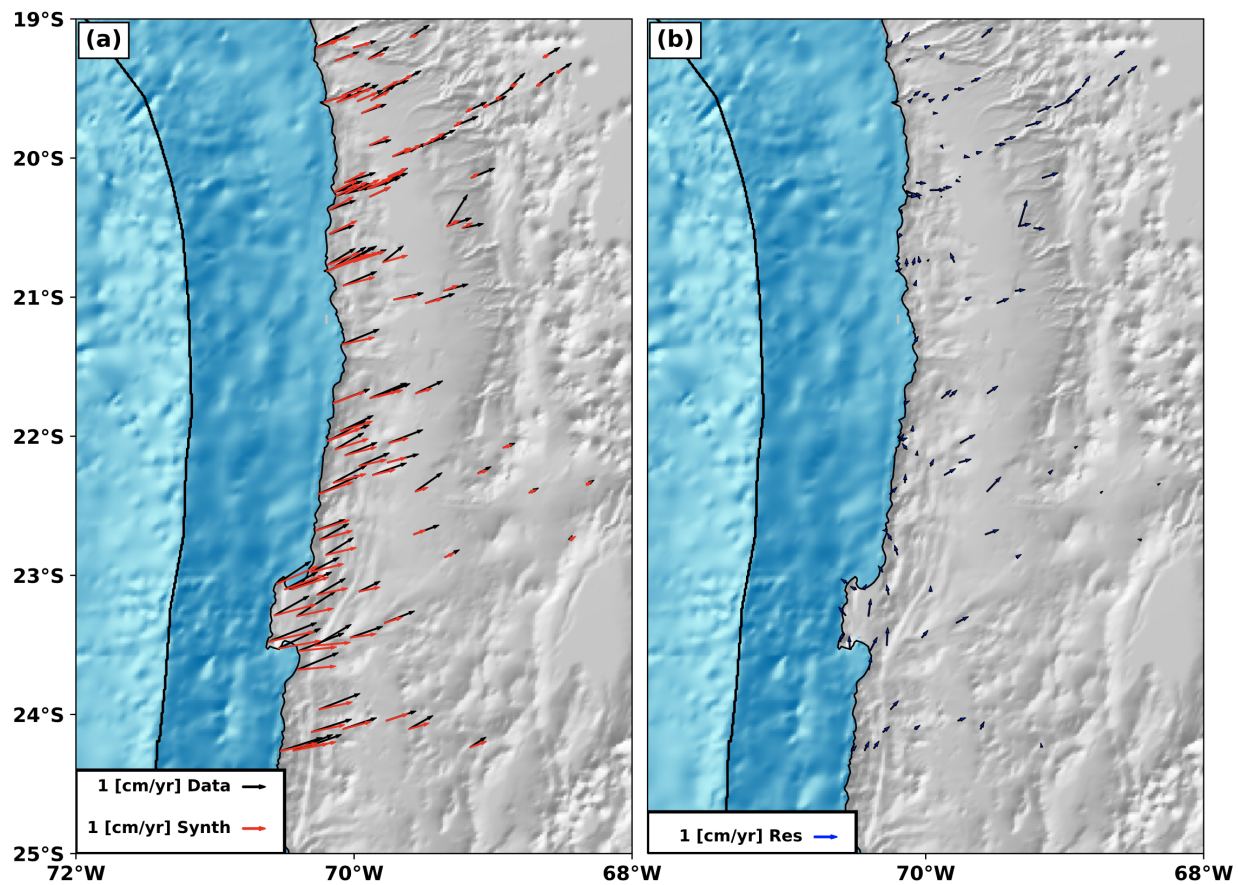


Figure S21. Same caption than Figure S20, but in Chile.

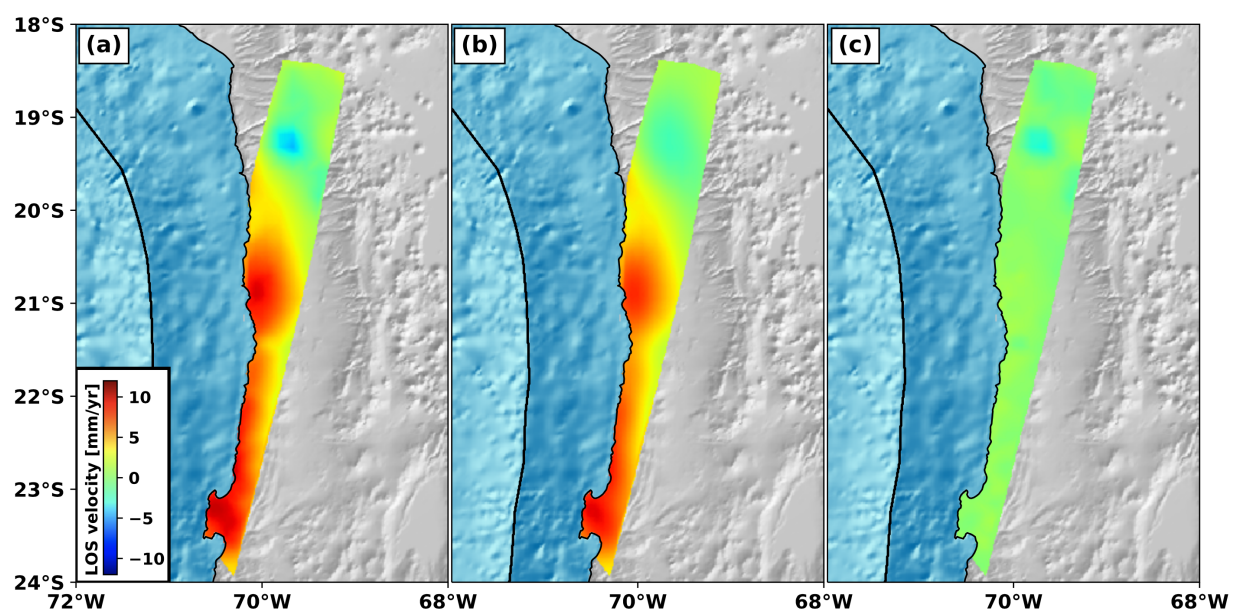


Figure S22. (a) Data, (b) Mean model, and (c) Residuals for InSAR velocity map.

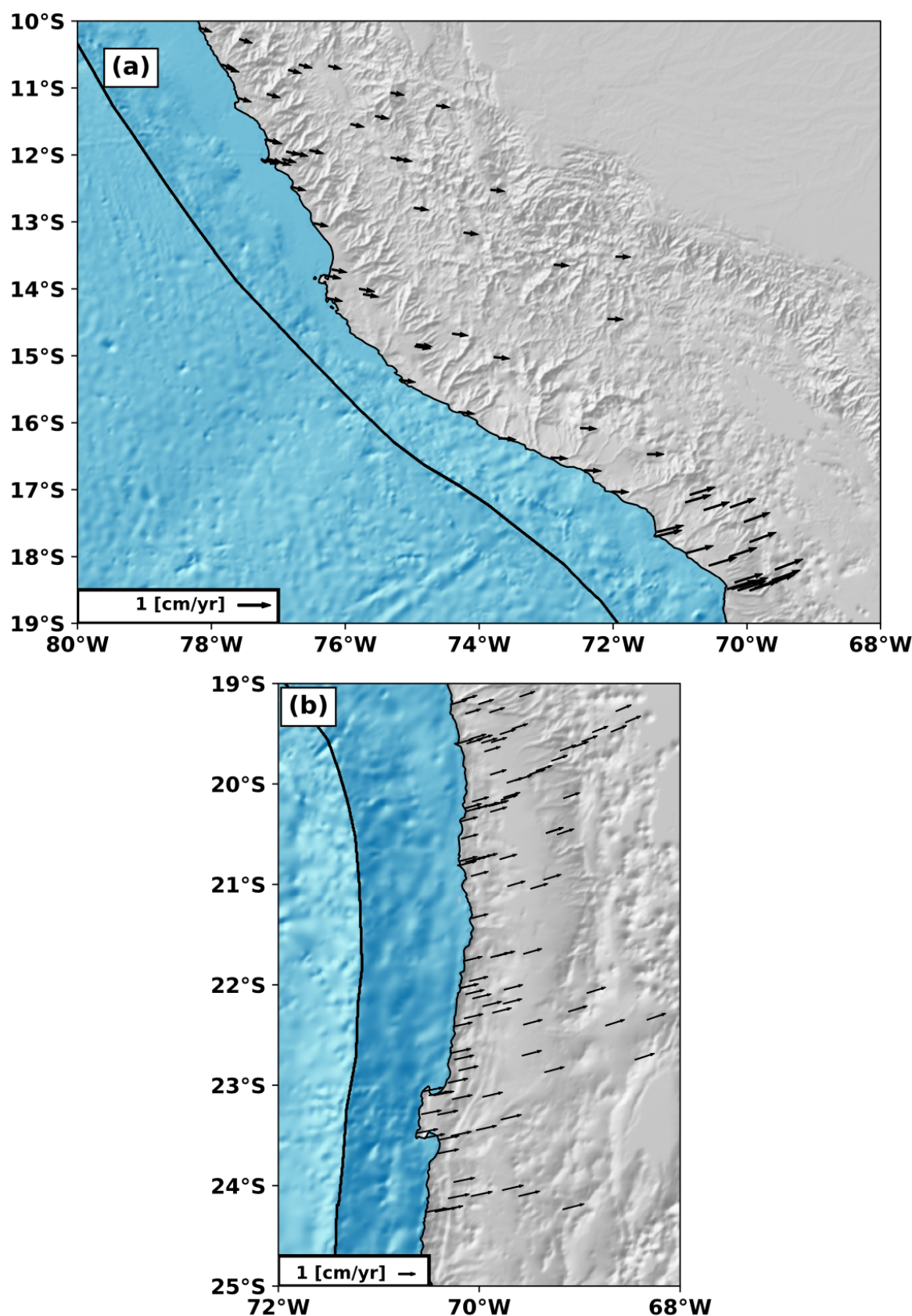


Figure S23. Mean translation for sliver motion in Peru (a) and Chile (b).

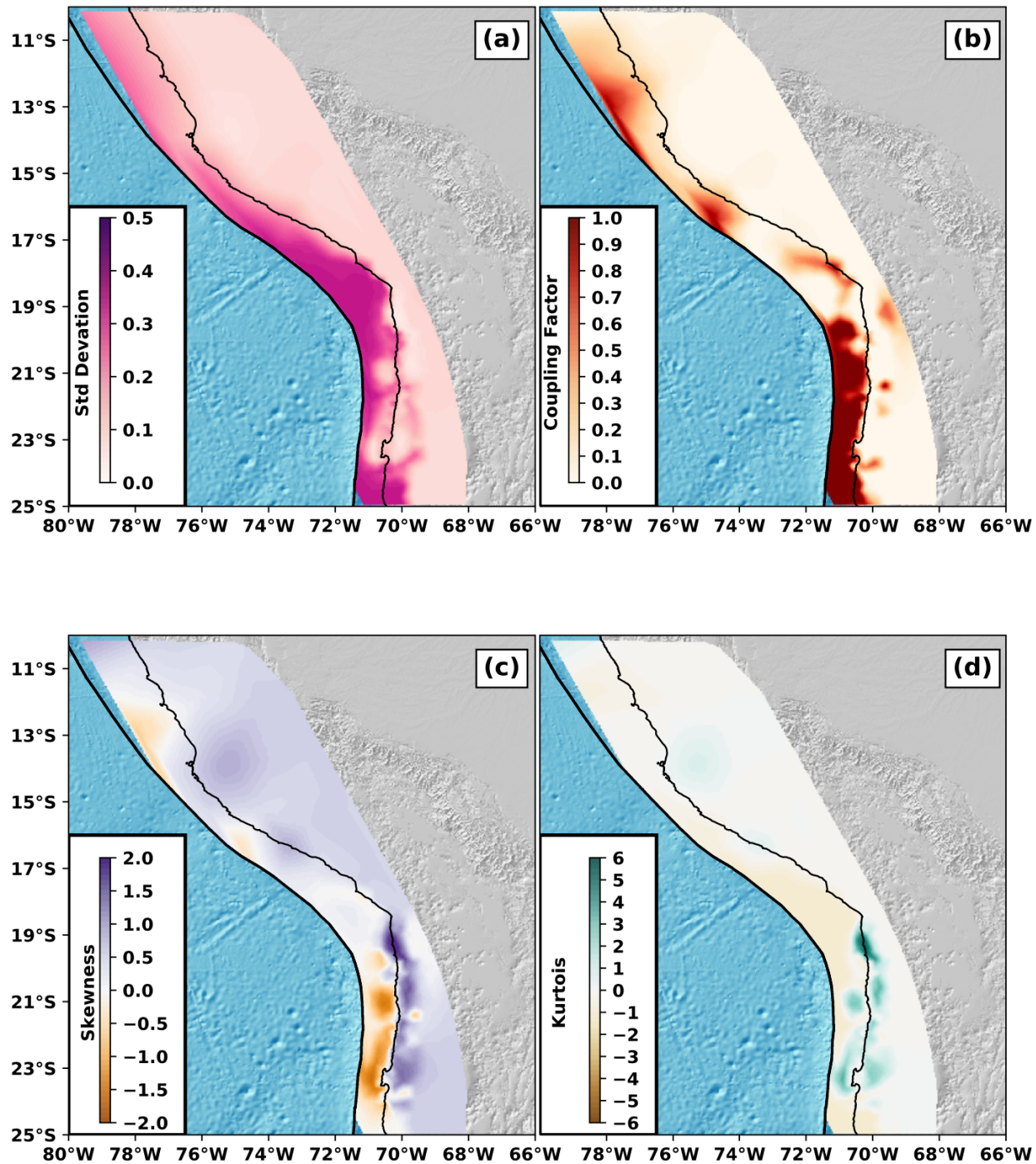


Figure S24. Posterior PDF statistical analysis. (a) Standard deviation, (b) Mode Model, (c) Skewness and (d) Kurtosis.

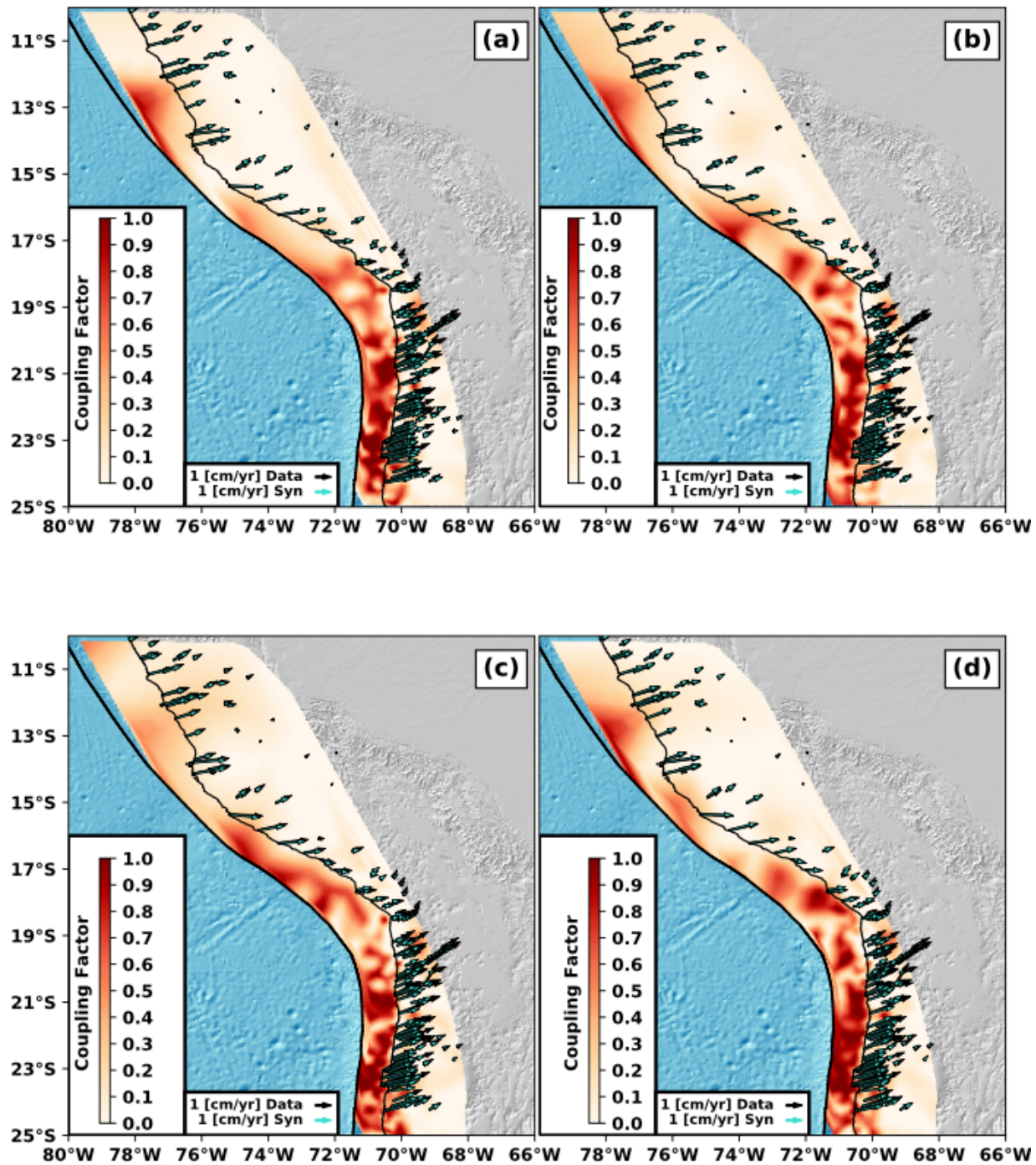


Figure S25. Four random coupling models (from 250000), along with GNSS data (black arrows) and model (light green).

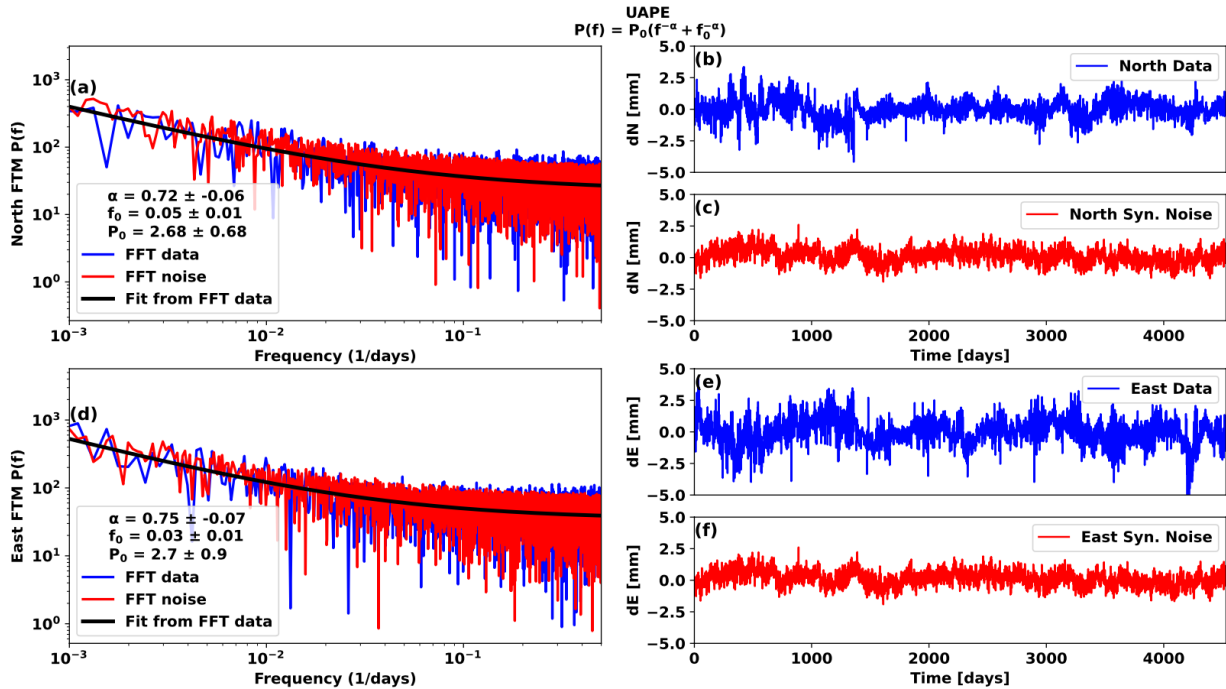


Figure S26. (a) FFT of North displacement for UAPE station (blue) and for a synthetic generated Noise (red), where the black line denotes fit from the model following the noise equation shown on top. (b) North displacement (blue) and (c) North synthetic displacement for UAPE station (red). (d,e,f) Same as (a,b,c) but for the East displacement for UAPE station.

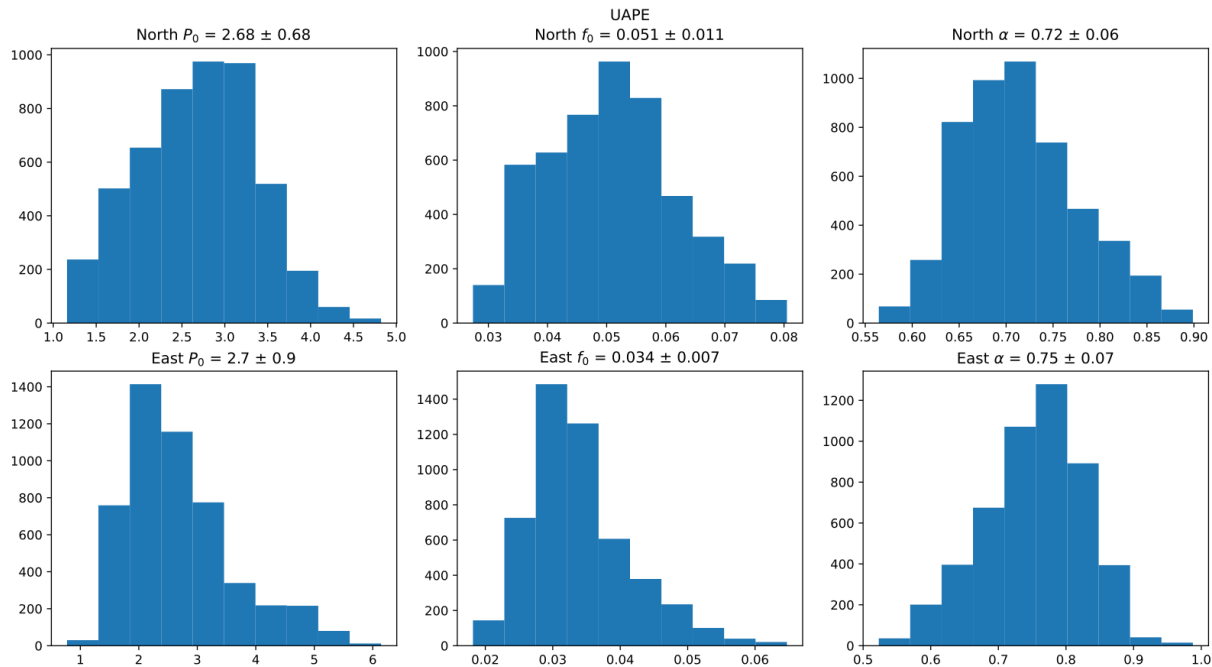


Figure S27. Probability density functions of the noise parameters (P_0 , f_0 and α) of UAPE station for North and East components. On top of each histogram is shown the mean and standard deviation of each parameter. The resume of those values for all the network are in Tables S39 - S40 for the North component and Tables S41 - S42 for the East ones.

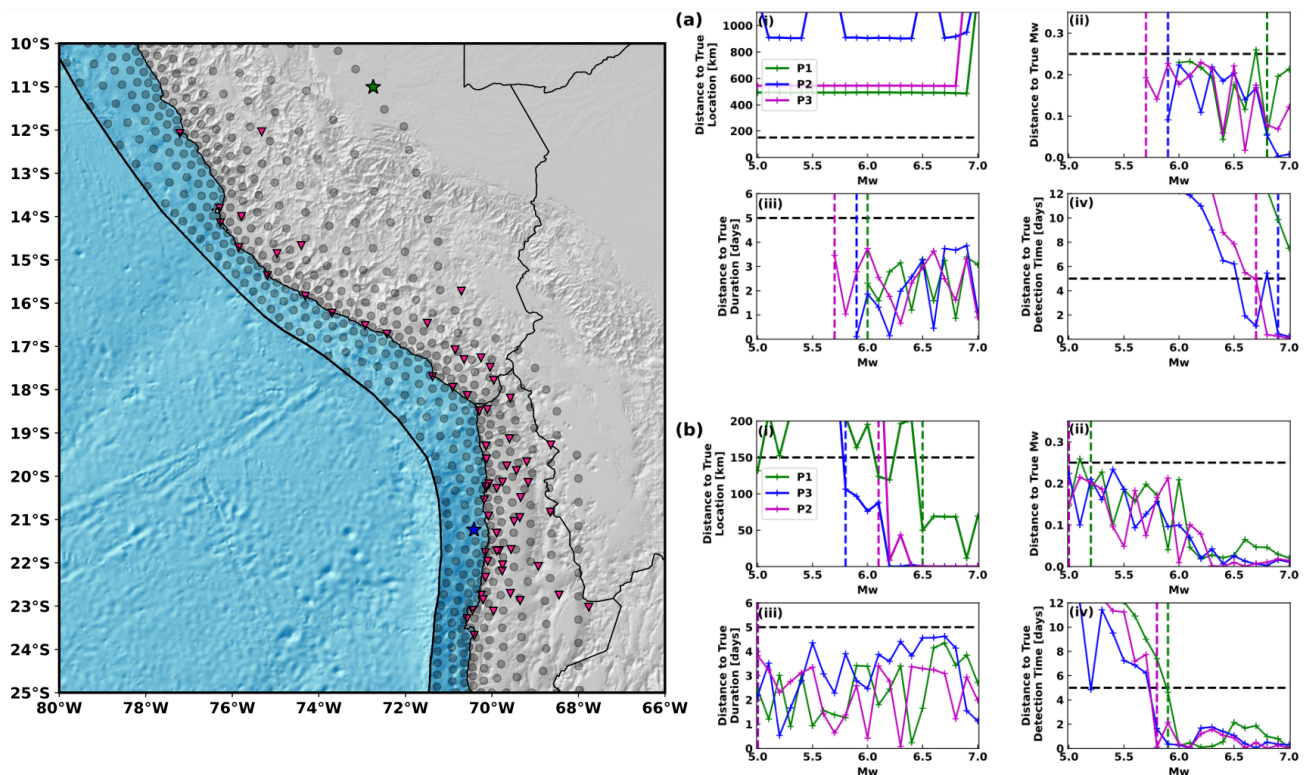


Figure S28. Examples of resolution test on synthetics of 10 days duration. On the left Figure, black dots are fault nodes on the fault plane, along with GNSS station locations denoted by inverted pink triangles. The red star indicates the fault node 5 location, while the blue denotes fault node 71. (a) Resolution test for fault node 5. (i) Mean distance (1000 models in all cases) to the true synthetic location in the function of the synthetic magnitude for Period 1 (green), Period 2 (blue), and Period 3 (pink). (ii) Mean modeled magnitude, (iii) duration, and (iv) true-time detection distance to the true synthetics in magnitude's function. Dashed black lines are the thresholds used on each fault node (i:150km, ii: 0.25Mw, iii and iv: 5 days). Dashed vertical lines denote the minimal magnitude detectable at each parameter. Same as (a), but for fault node 71.

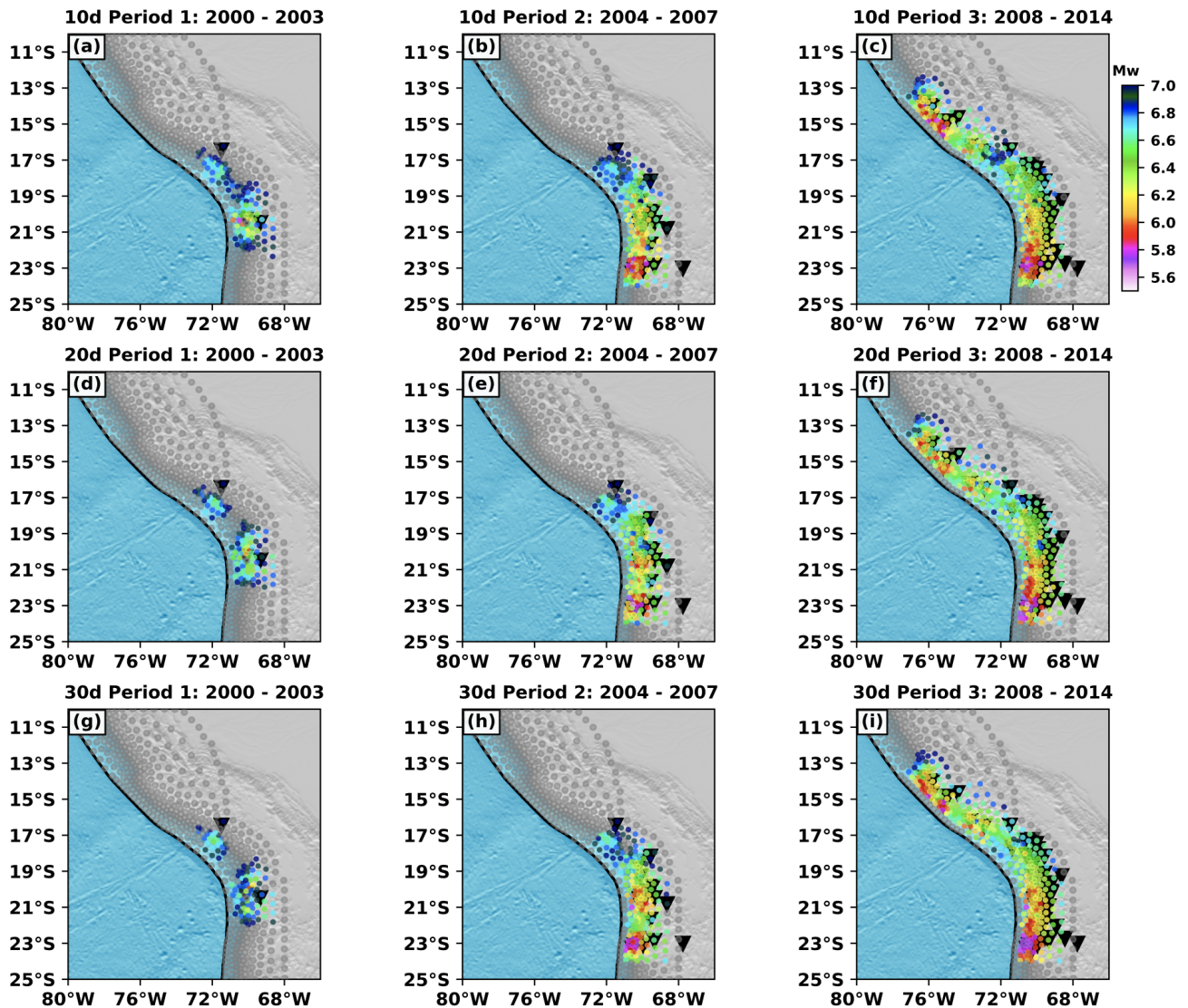


Figure S29. Resolution test maps for synthetics with a duration of 10 days by period (a,b,c), 20 days (d,e,f) and 30 days (g,h,i), not considering Pearson correlation coefficient for synthetics locations.

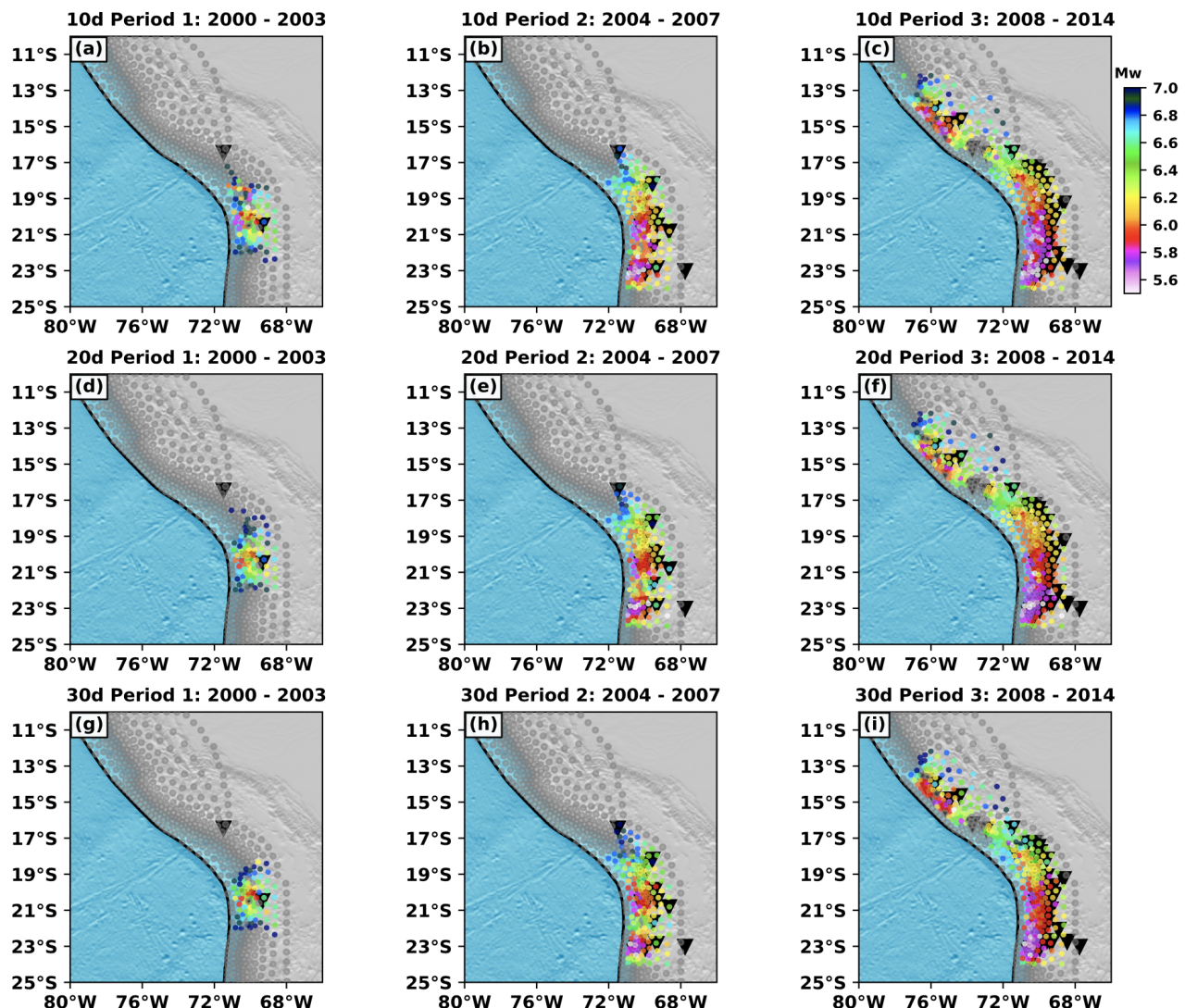


Figure S30. Resolution test maps for synthetics with a duration of 10 days by period (a,b,c), 20 days (d,e,f) and 30 days (g,h,i), considering a Pearson correlation coefficient of 90% for synthetics locations.

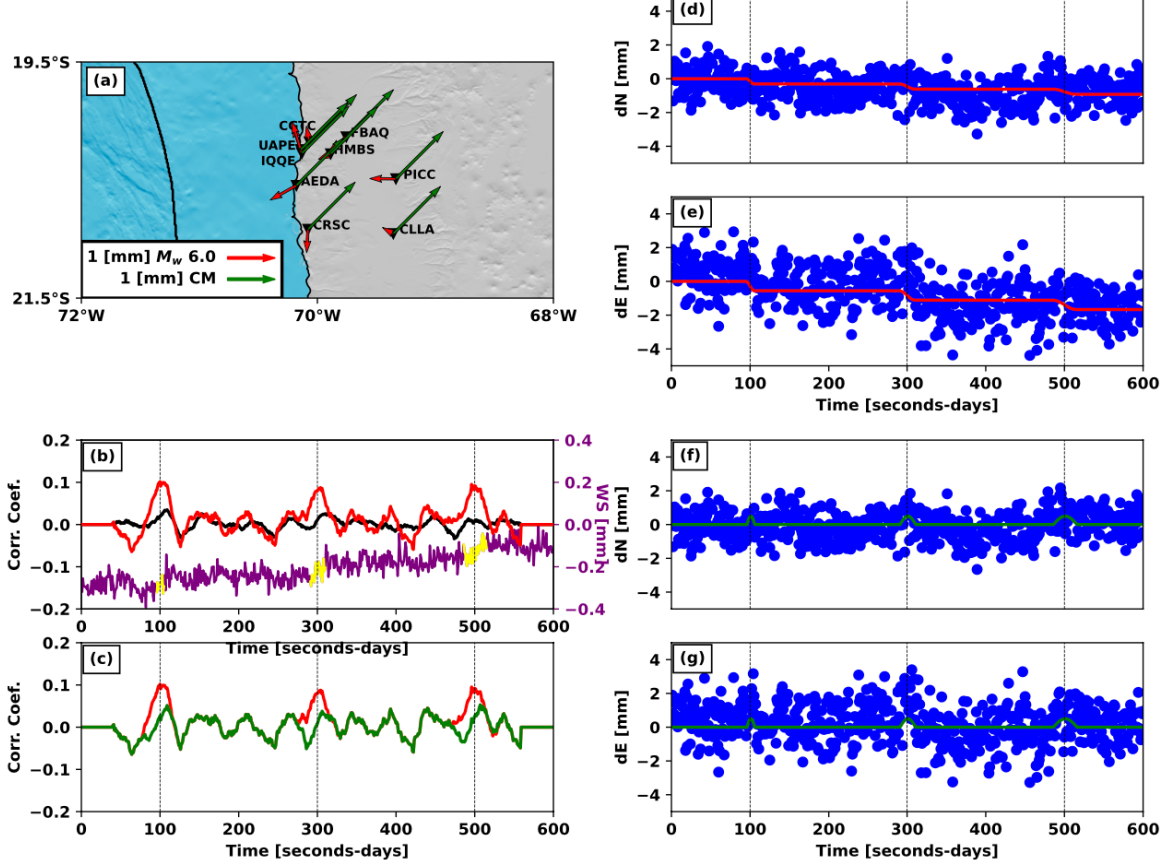


Figure S31. Synthetic example of aseismic slip event versus common mode source. (a) Distributed slip at a fault node corresponding to a magnitude of M_w 6. Red arrows indicate the displacement produced by such a slip source. Green arrows indicate a common mode with a displacement of 1 mm. (b) Sum of the weighted correlation function (red curve) at all stations for synthetic aseismic slip events added to synthetic noise based on realistic parameters (Tables S39-S42), with durations of 10 days (synthetic added at 100 days), 20 days (300 days), and 30 days (500 days). The synthetic template has a duration of 40 days and a slip amplitude corresponding to a magnitude of M_w 6. The black curve represents the correlation function at the AEDA station. Magenta line denotes the GNSS weighted stack, where the yellow segments are the timing we have added the synthetic slow slip events to the original signals. (c) Same as (b), but the green curve is equivalent to the red one considering a common mode source instead of an aseismic slip event. (d) AEDA station, north synthetic displacement including synthetic aseismic events (red curve). (e) Same as (d) but for eastward displacement. (f) AEDA station, north synthetic displacement including common mode sources (green curves). (g) Same as (f) but for eastward displacement.

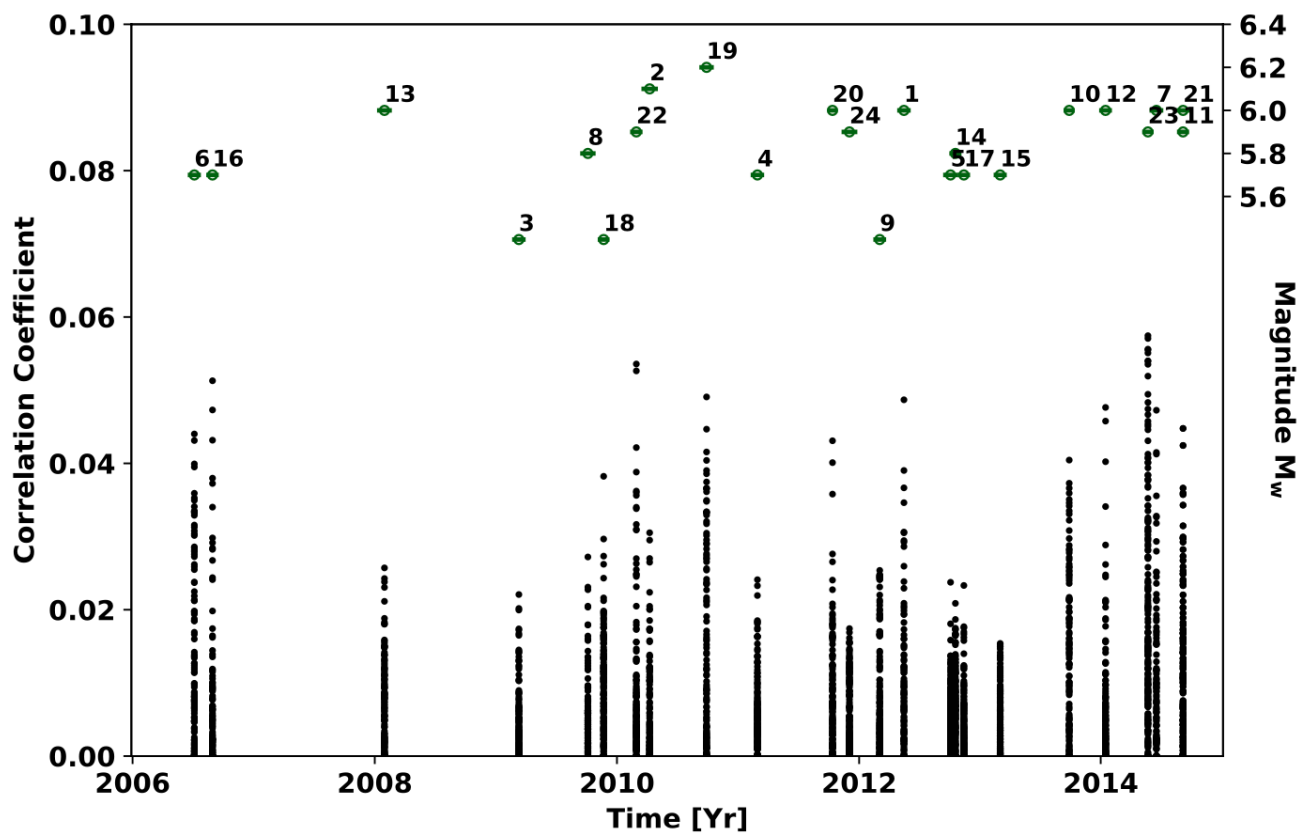


Figure S32. Correlation coefficients for each detected event, indicating its duration and magnitude in function of the time.

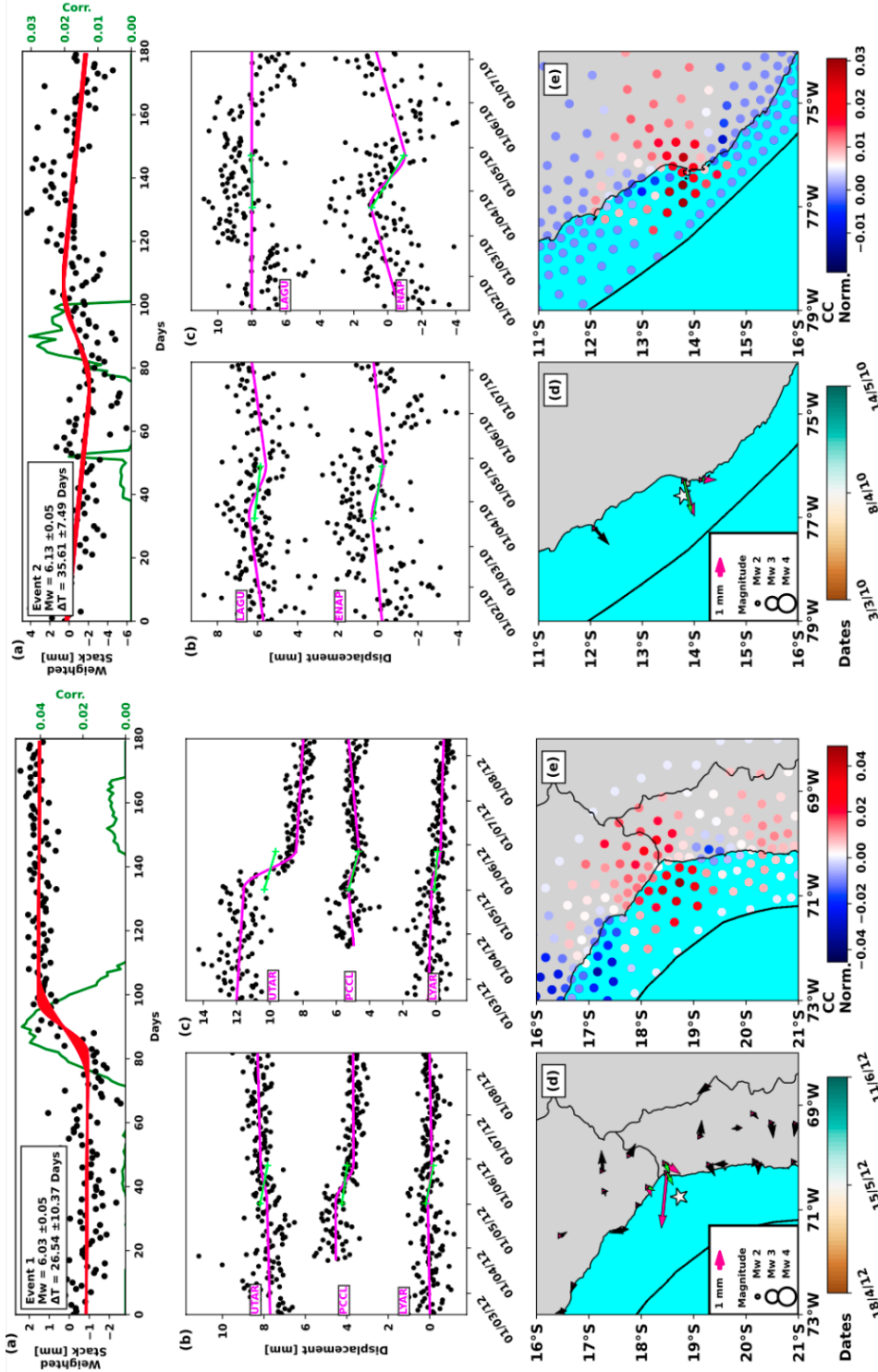


Figure S33. Stack (black dots), modeled events (red lines), and correlation function (green line) are presented alongside North and East displacement, as well as seismic activity and correlation peak map view during the SSE occurrence for events 1 (left side) and 2 (right side), as presented in the Figure 5 in the main text.

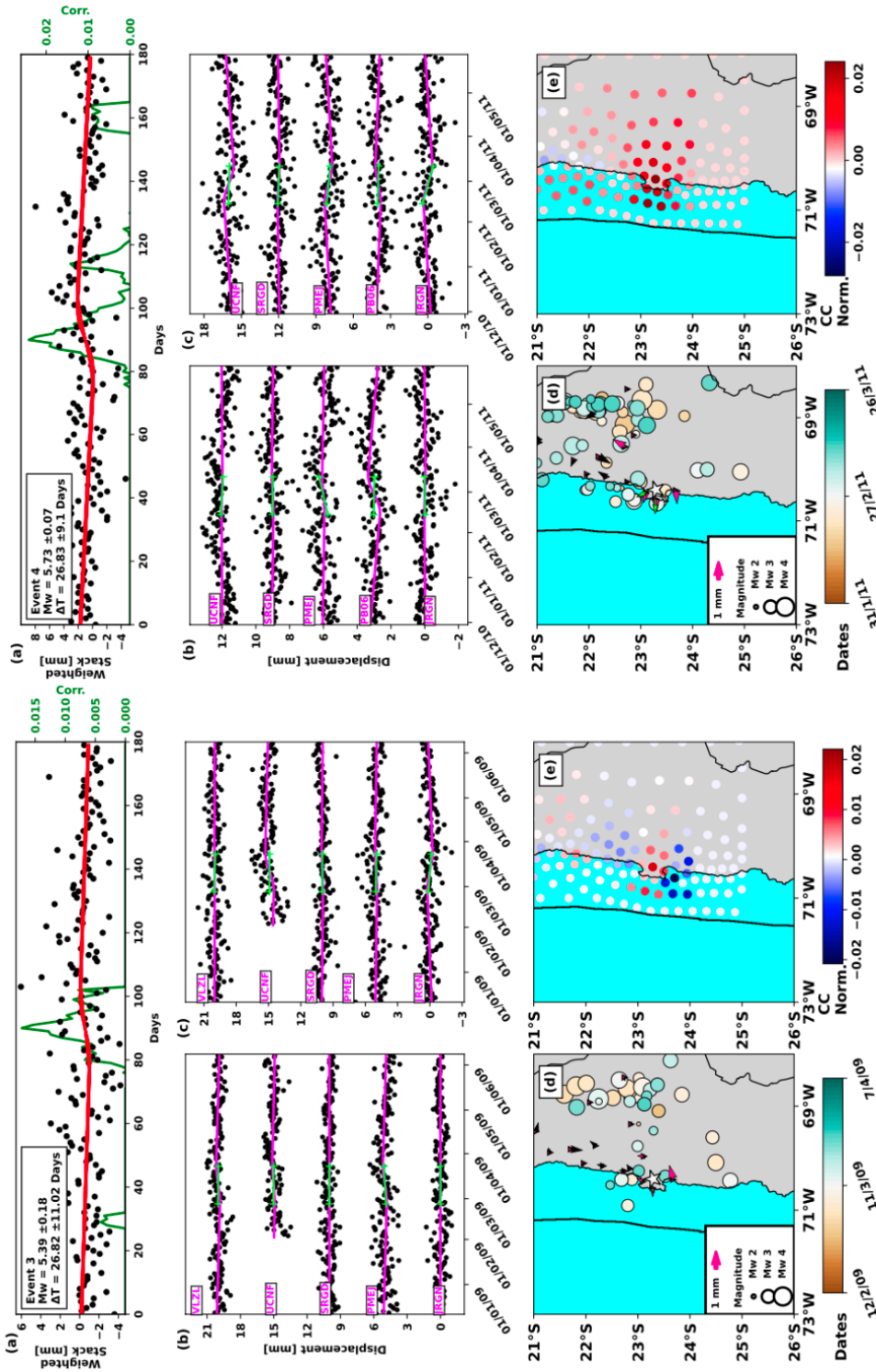


Figure S34. Same caption as Figure S33 for events 3 (left side) and 4 (right side).

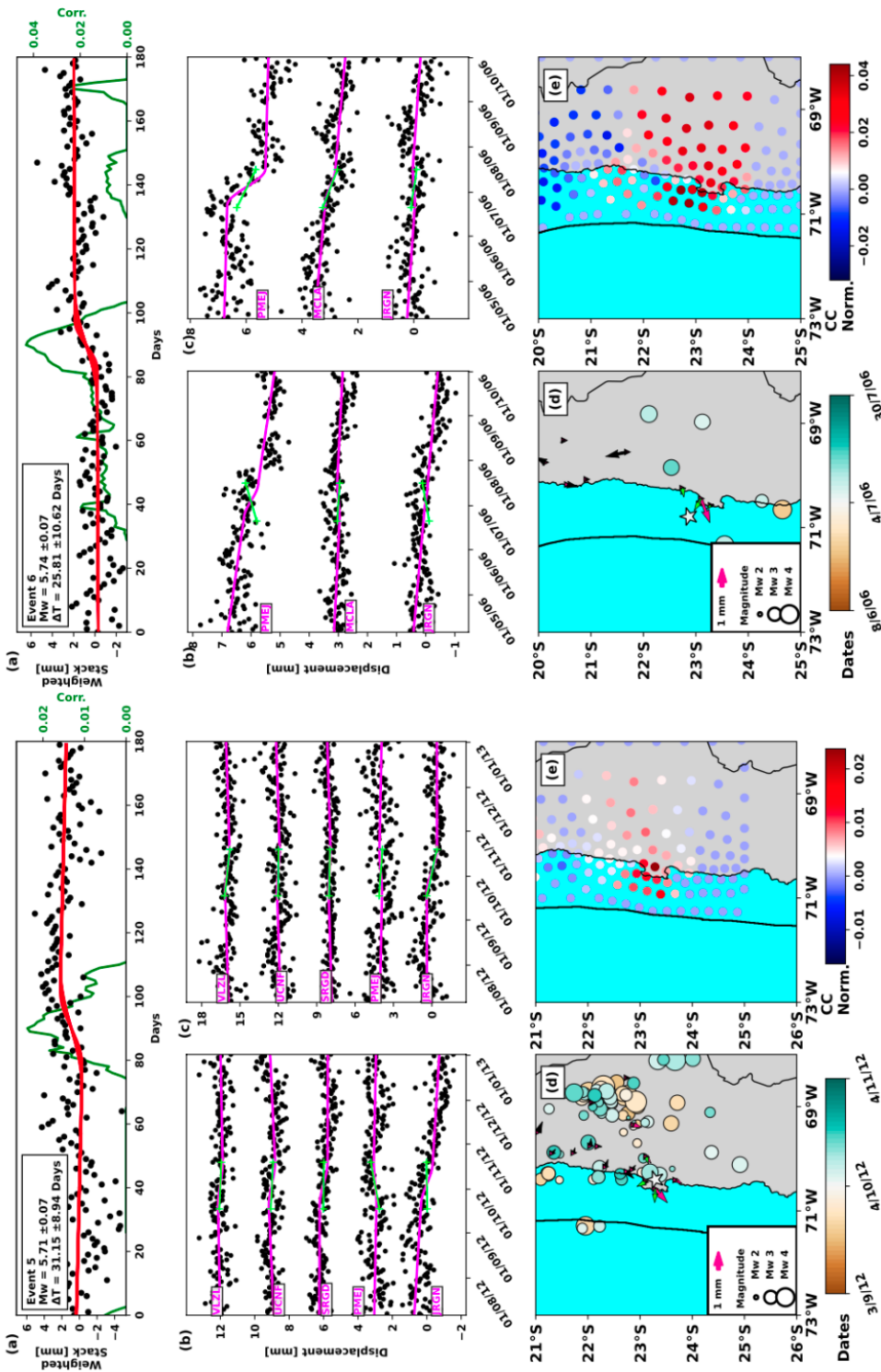


Figure S35. Same caption as Figure S33 for events 5 (left side) and 6 (right side).

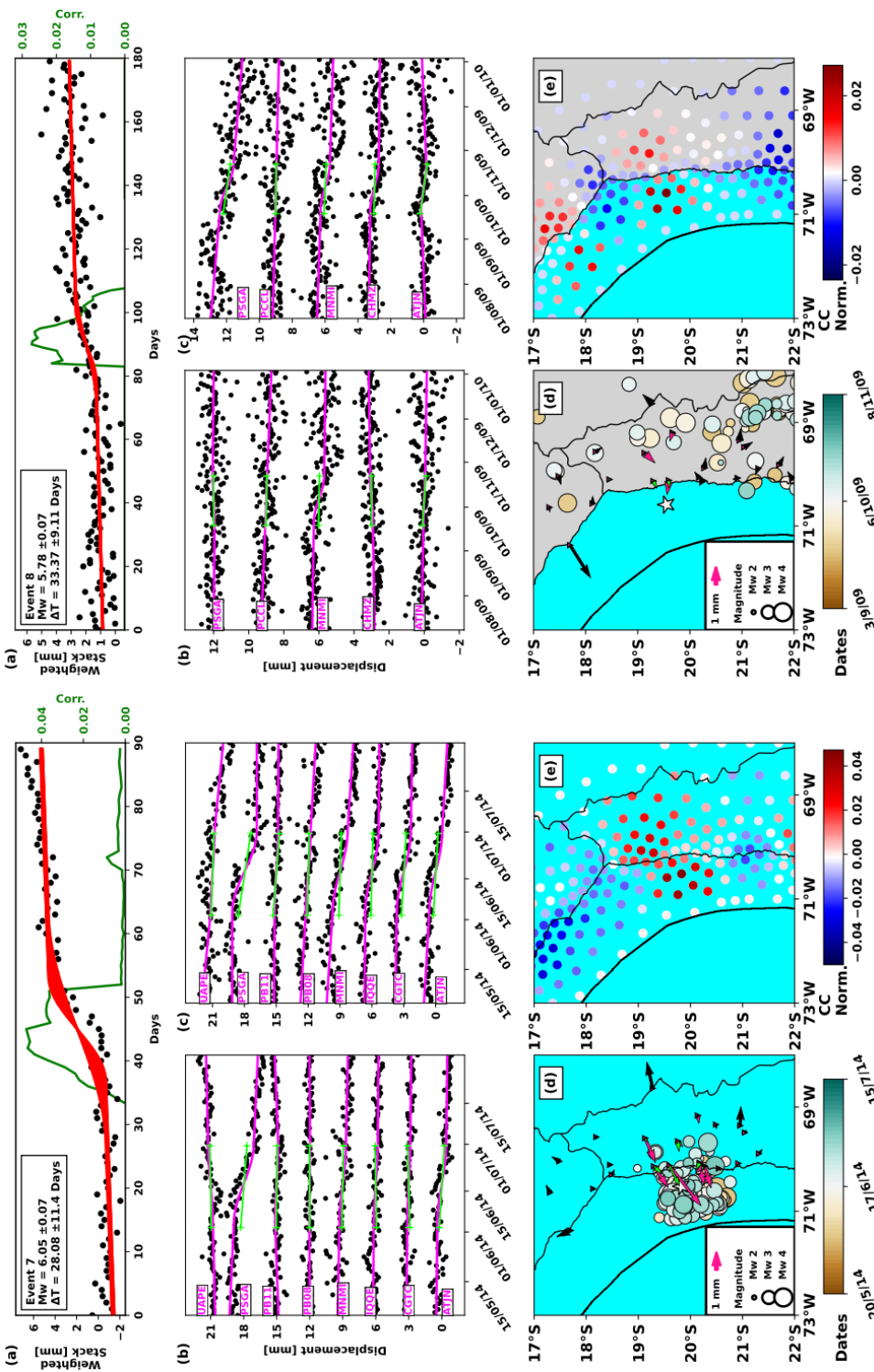


Figure S36. Same caption as Figure S33 for events 7 (left side) and 8 (right side).

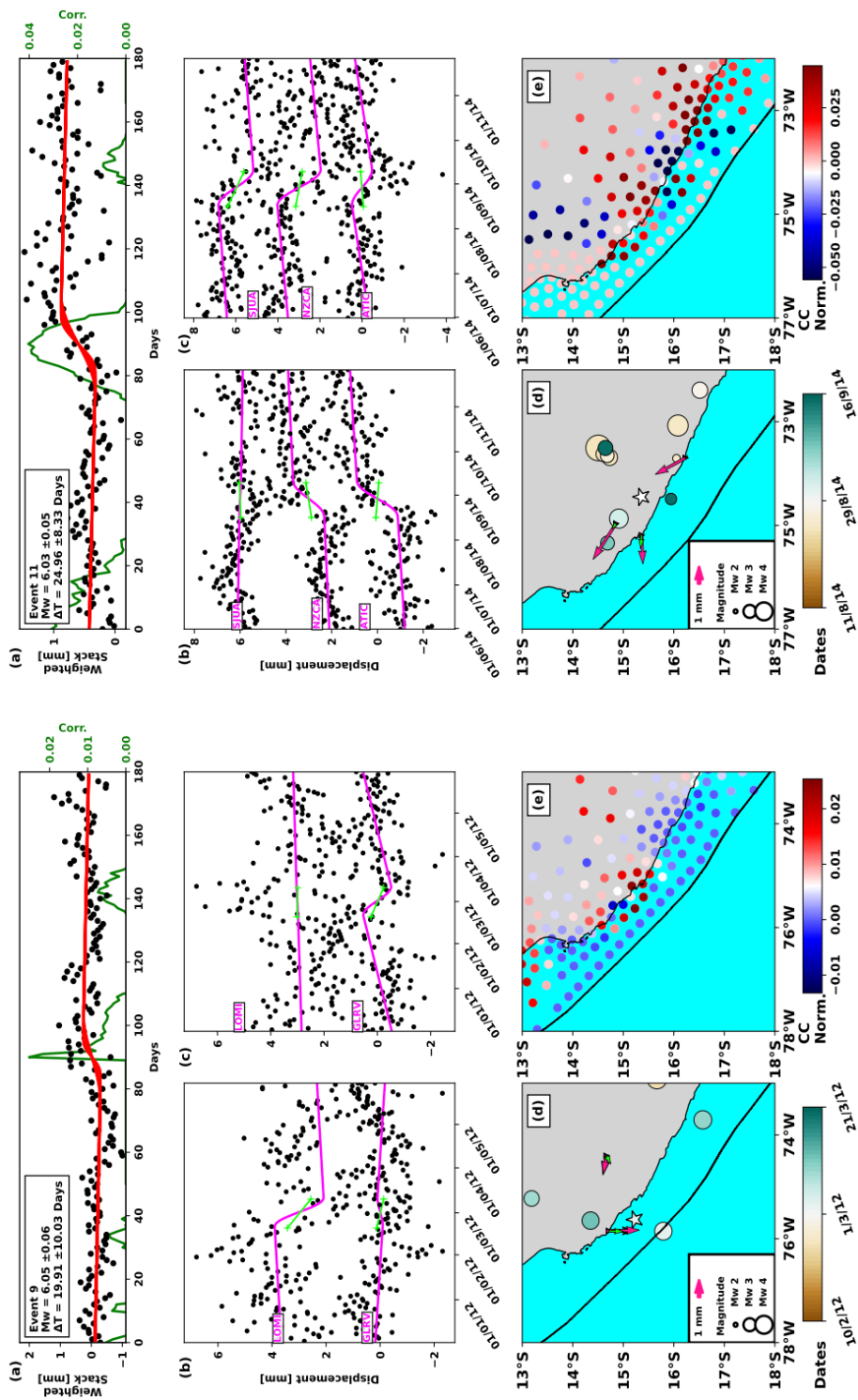


Figure S37. Same caption as Figure S33 for events 9 (left side) and 11 (right side).

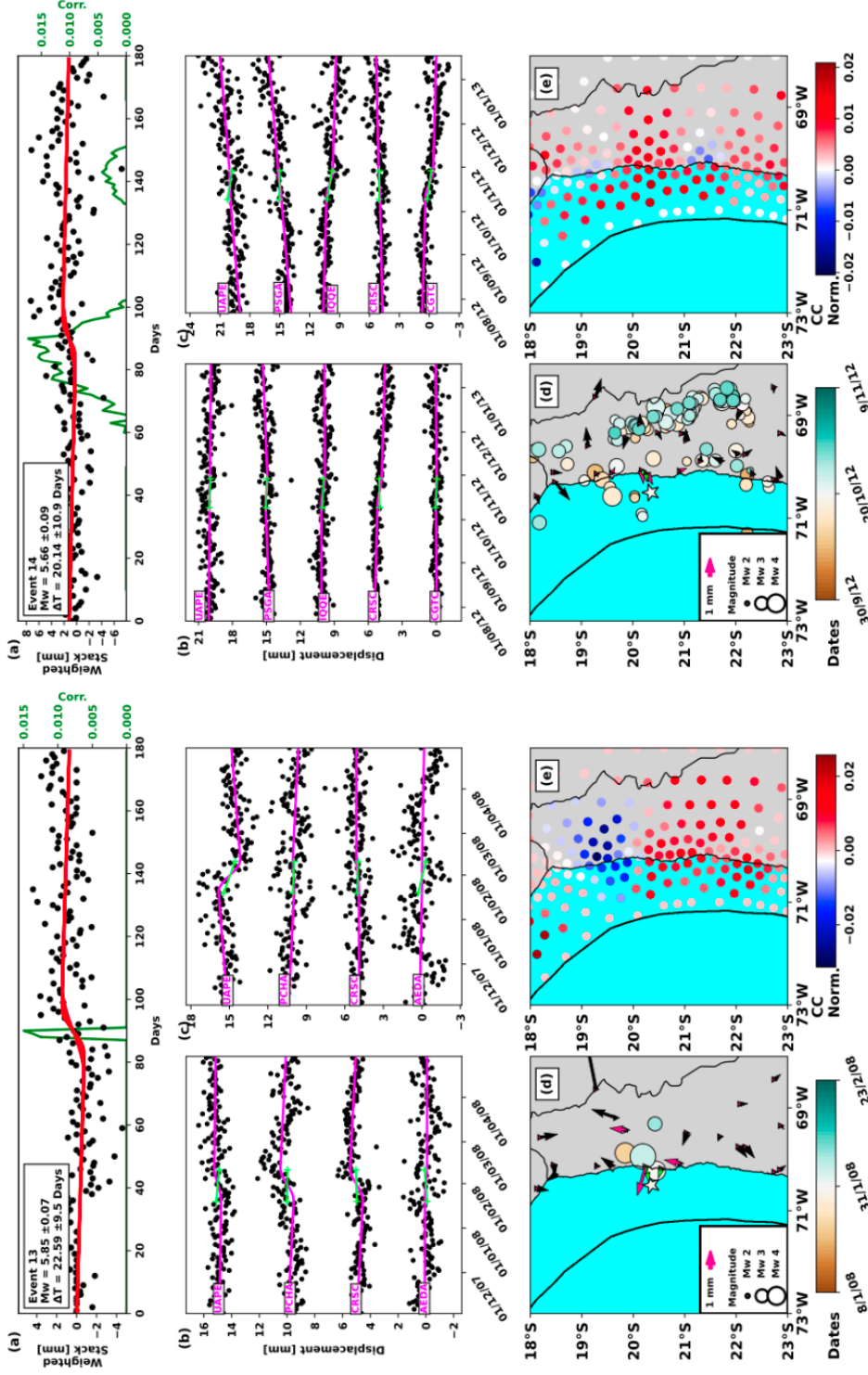


Figure S38. Same caption as Figure S33 for events 13 (left side) and 14 (right side).

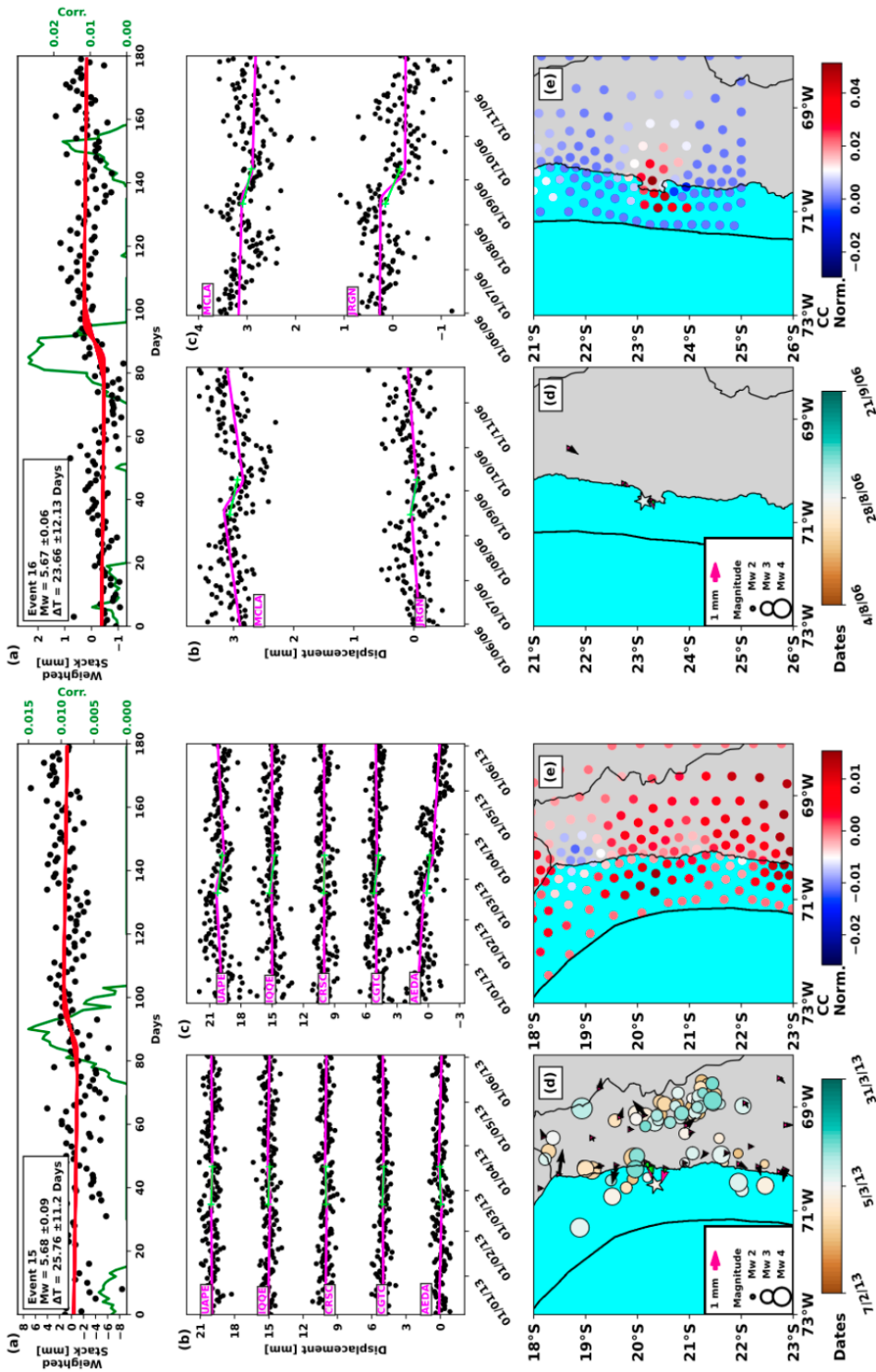


Figure S39. Same caption as Figure S33 for events 15 (left side) and 16 (right side).

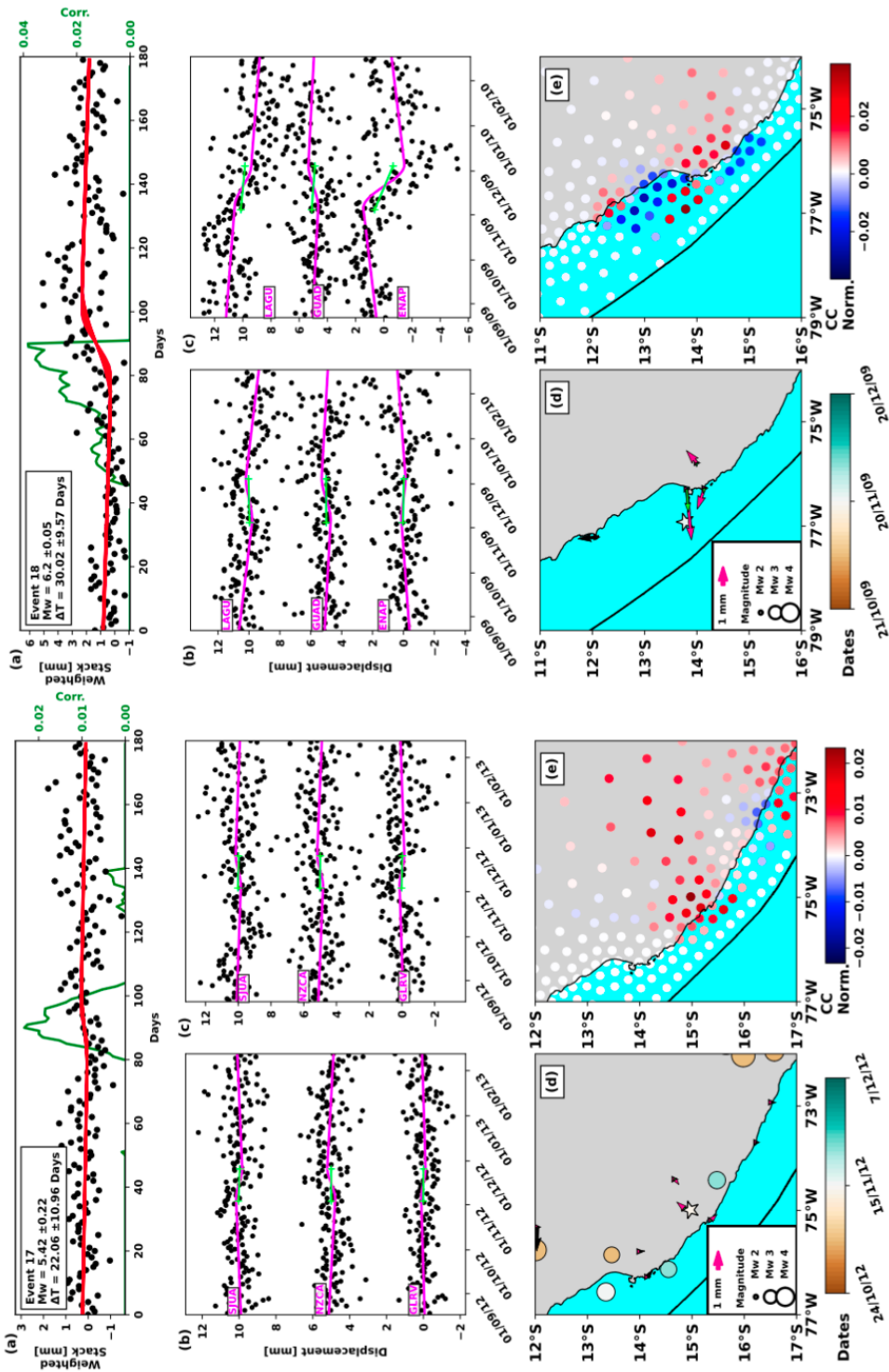


Figure S40. Same caption as Figure S33 for events 17 (left side) and 18 (right side).

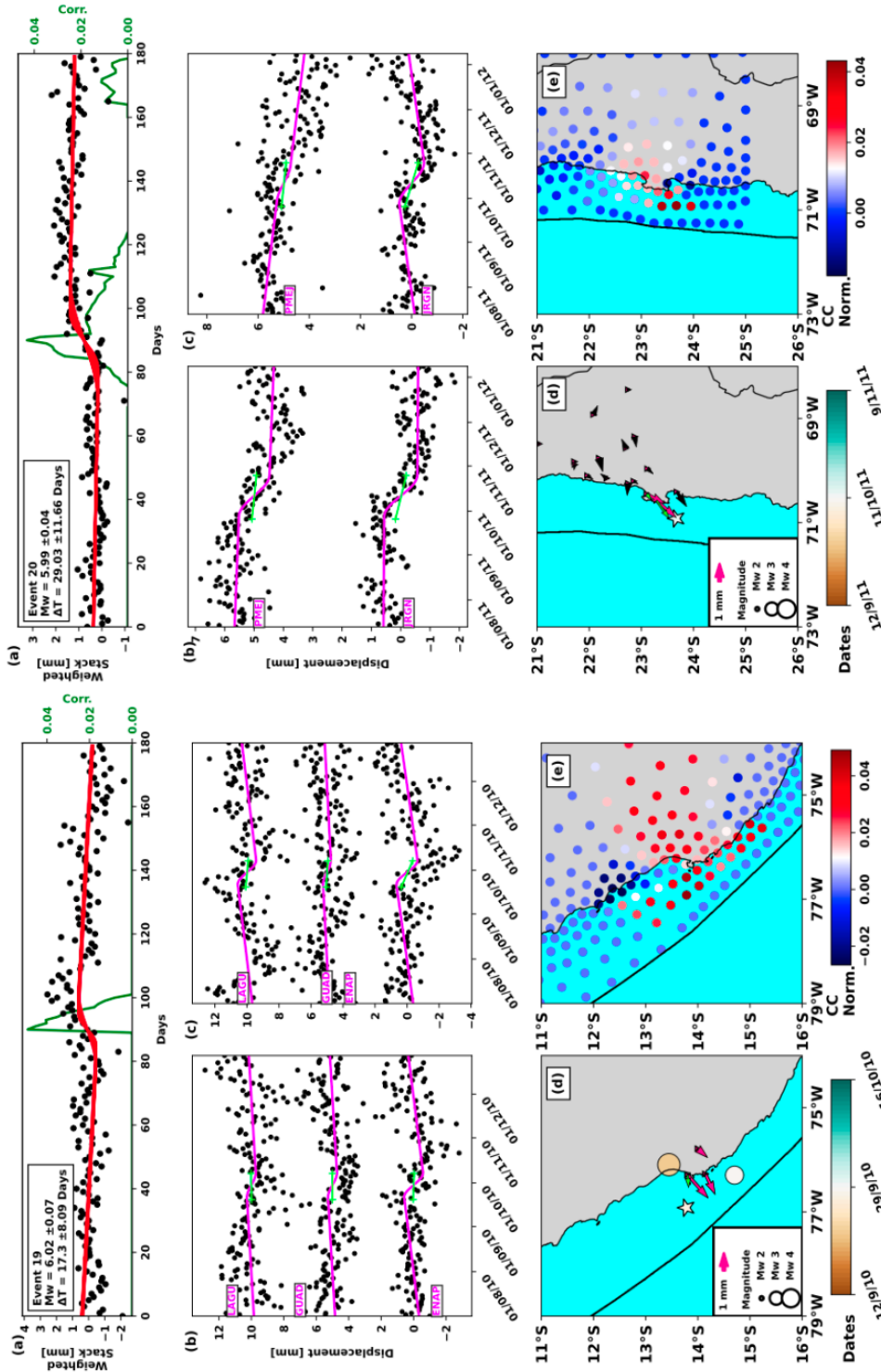


Figure S41. Same caption as Figure S33 for events 19 (left side) and 20 (right side).

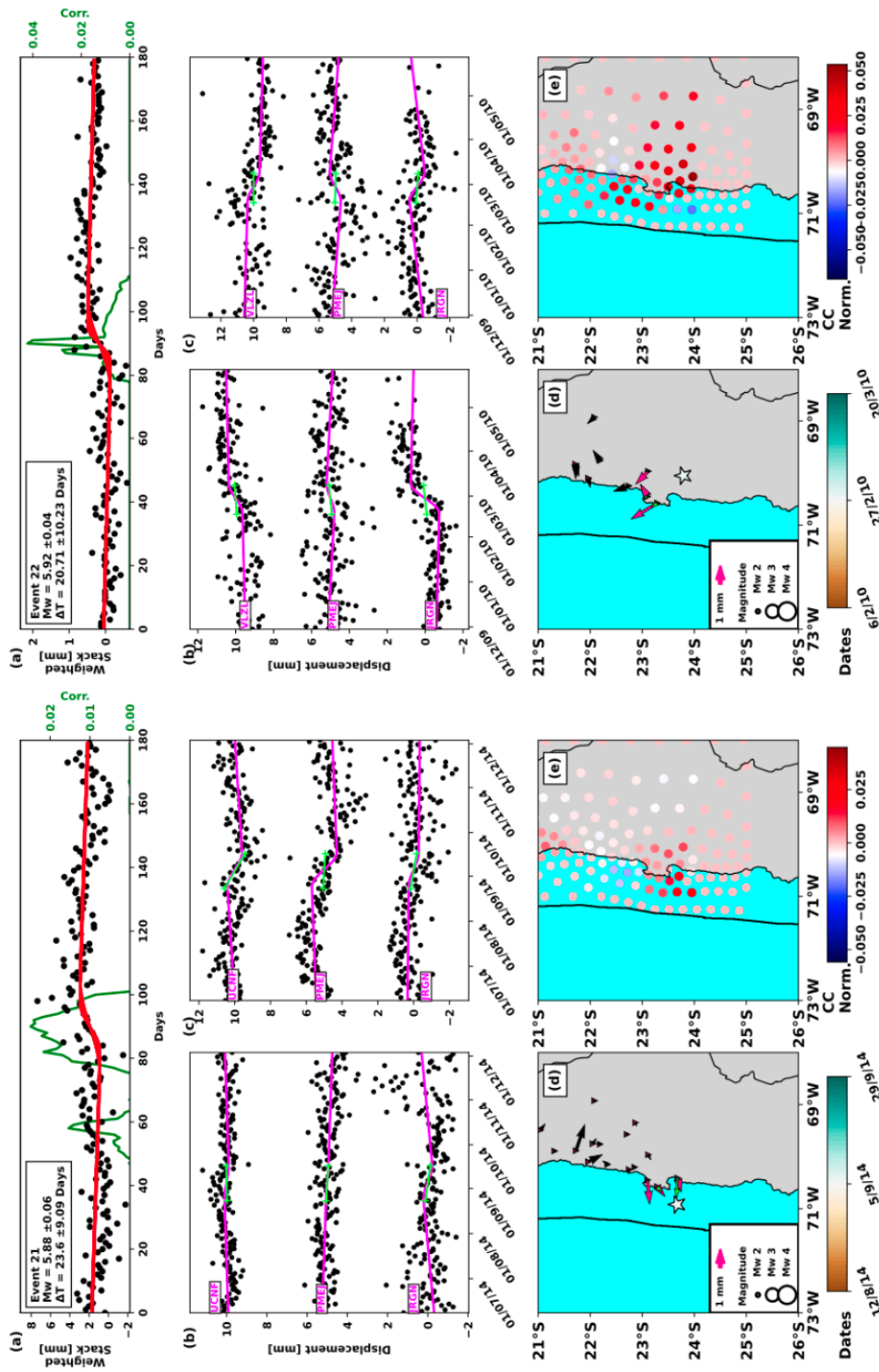


Figure S42. Same caption as Figure S33 for events 21 (left side) and 22 (right side).

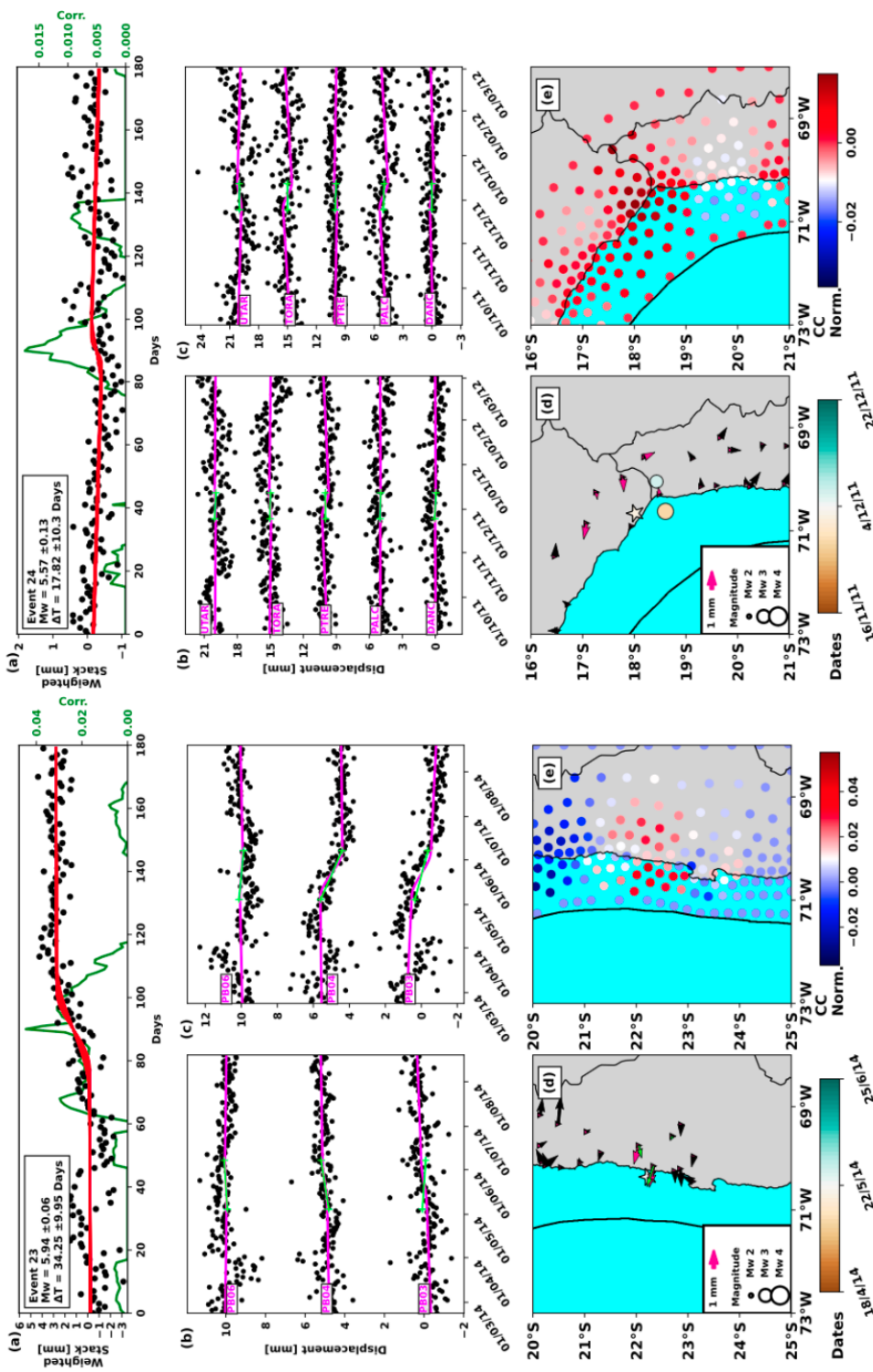


Figure S43. Same caption as Figure S33 for events 23 (left side) and 24 (right side).

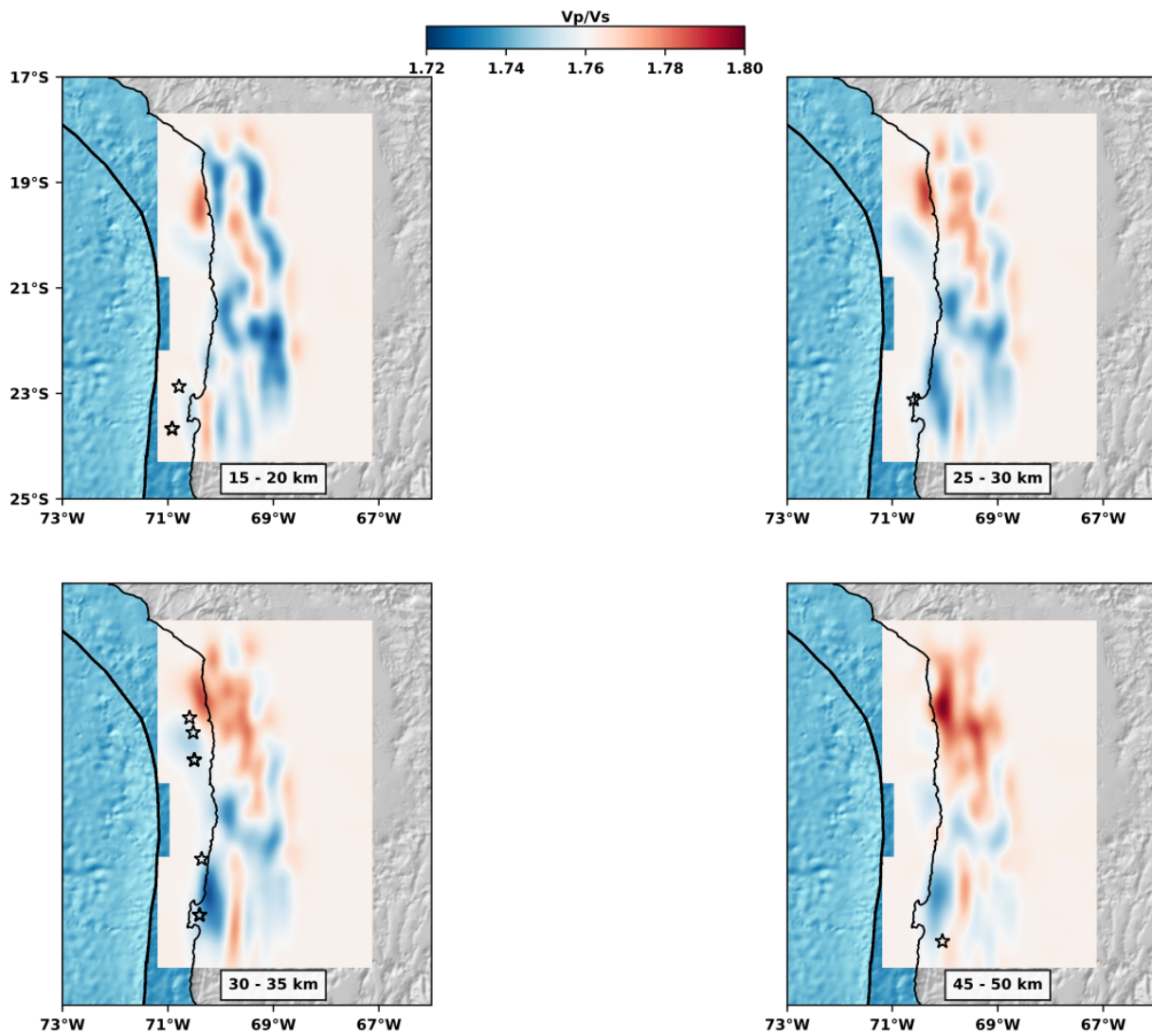


Figure S44. Mean V_p/V_s values for depths ranges in the North Chile subduction zone. Stars denote the location of aseismic events detected in this study at the corresponding depth. V_p/V_s values from Comte et al. (2016).

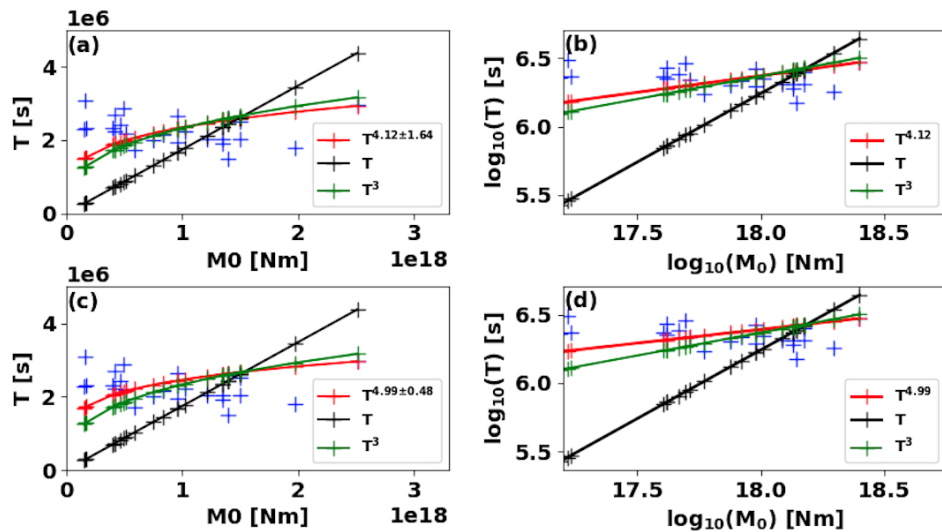


Figure S45. (a) Moment-duration scaling estimated by using a curve fitting method (Virtanen et al., 2020) in Eq. 16, with T [s] and M_0 [Nm]. (b) same as (a) in $\log\log$ scale. The black lines represent a $M \propto T$ scaling, while green ones are $M \propto T^3$, and red lines represent the inverted values $M \propto T^{4.12 \pm 1.64}$. (c) and (b), same as (a) and (b), but parameters are estimated using a Bayesian framework (Abril-Pla et al., 2023). Colors are the same as described above, but red lines are a $M \propto T^{4.99 \pm 0.48}$ scaling, where the standard deviation represents 94% of a confidence interval.

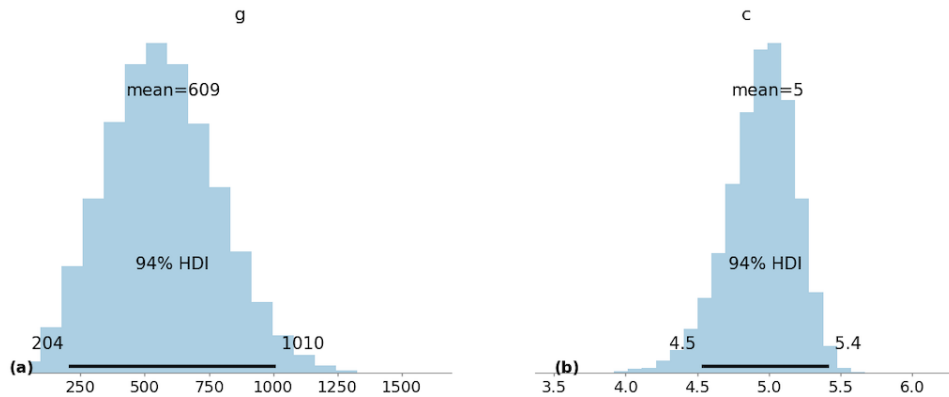


Figure S46. PDF for estimated parameters g (a) and c (b) in Eq. 16, using a Bayesian framework. On top of each PDF, the mean parameter values are shown, whereas, at bottom, the 94% confidence intervals are indicated.

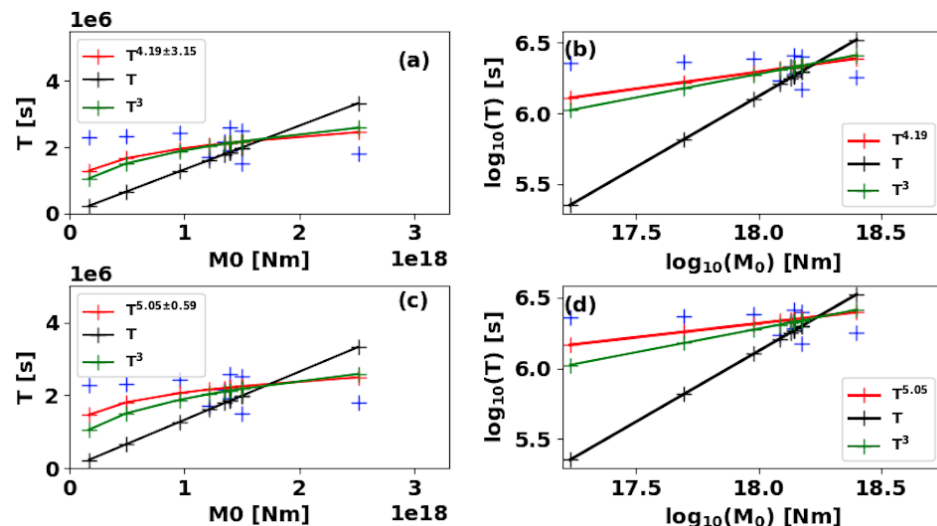


Figure S47. Same as Figure S45, but considering events classified as A.

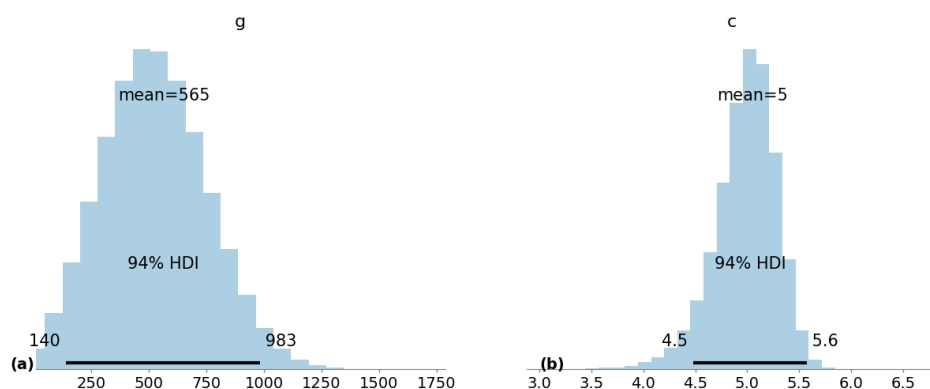


Figure S48. Same as Figure S46, but considering events classified as A.

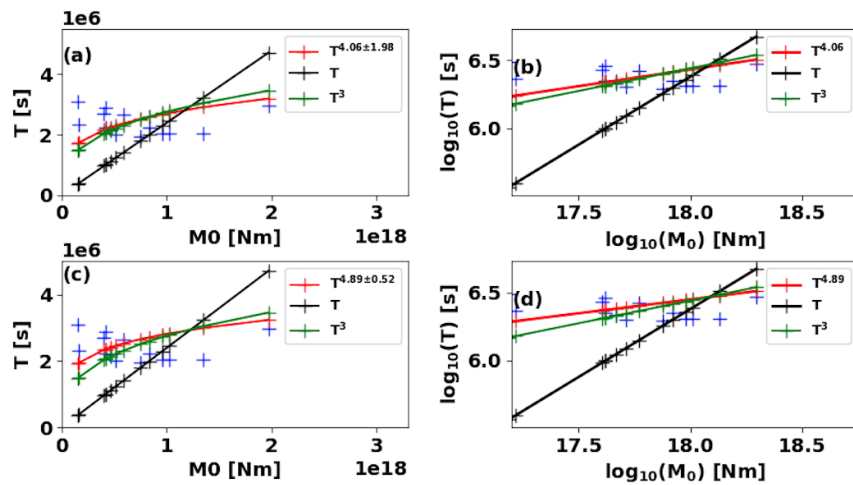


Figure S49. Same as Figure S45, but considering events classified as B.

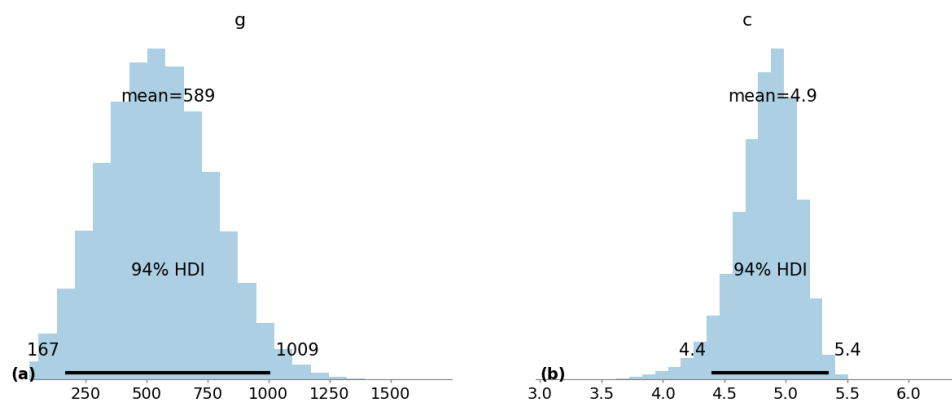


Figure S50. Same as Figure S46, but considering events classified as B.

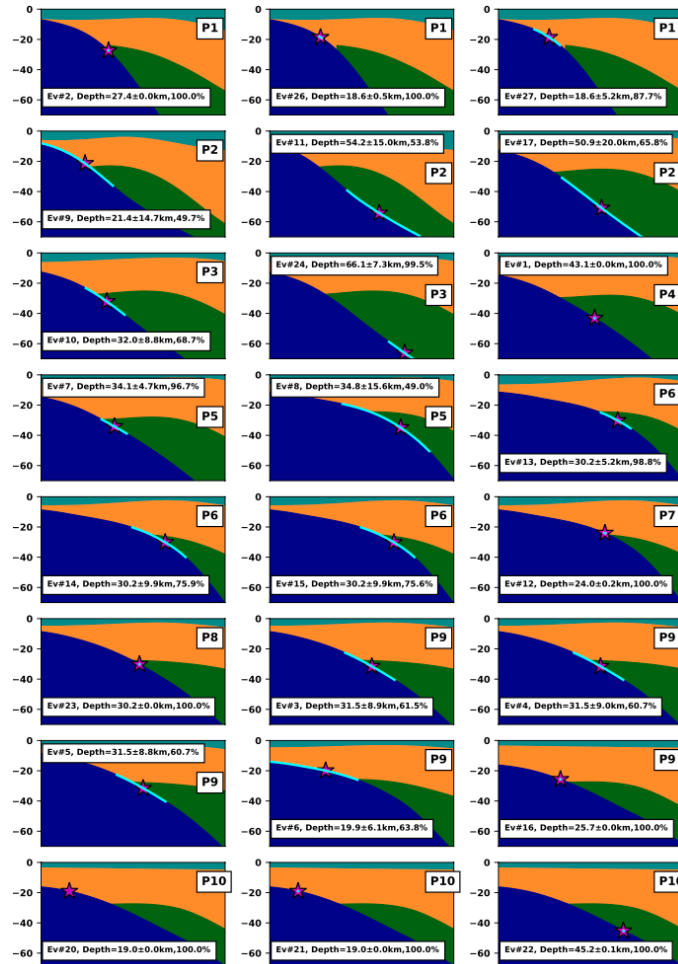


Figure S51. Location of the event at depth. Colors indicate the respective structure at depth (upper and lower crust, lithospheric mantle, asthenospheric wedge, and oceanic crust). White boxes indicate events ID along each profile, depth, and their probability of being within the polygon used to perform the analysis.

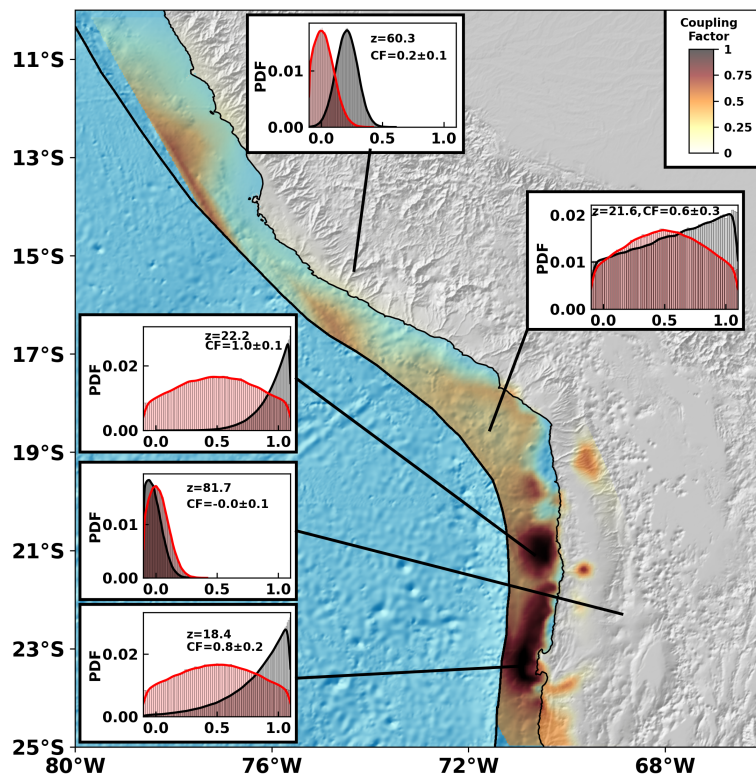


Figure S52. Background color from white to dark through yellow and red is the mean coupling distribution. Black red areas ($C \sim 1$) are locked regions, while transparent areas ($C \sim 0$) are regions that slip aseismically at a rate equal to the plate convergence rate. Five *a priori* (red) and *a posteriori* (gray) probability density functions (PDF) are shown for five nodes along the slab mesh.

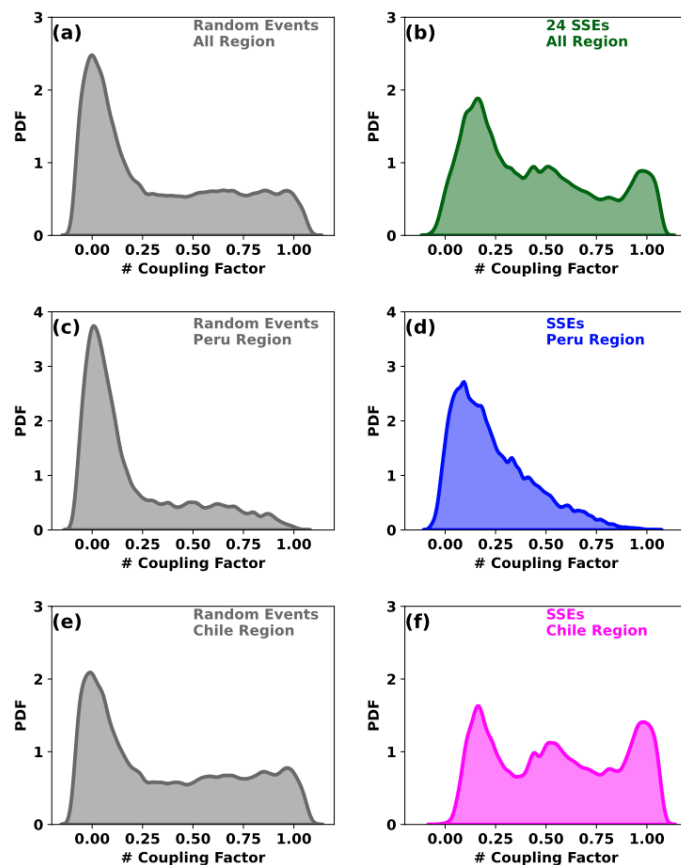


Figure S53. Depth Probability Density Functions (PDF) of coupling for 24 detected events/random picks. (a) Random picks PDF for the entire region, with the dark gray line representing the Kernel Density Estimation (KDE). (b) same as (a), but for depths shallower than 60km. (c) same as (a), but for the depths of our detected events. (d), (e), and (f) same as (a), (b), and (c) for the Peruvian regions, while (g), (h), (i) for the Chilean regions.

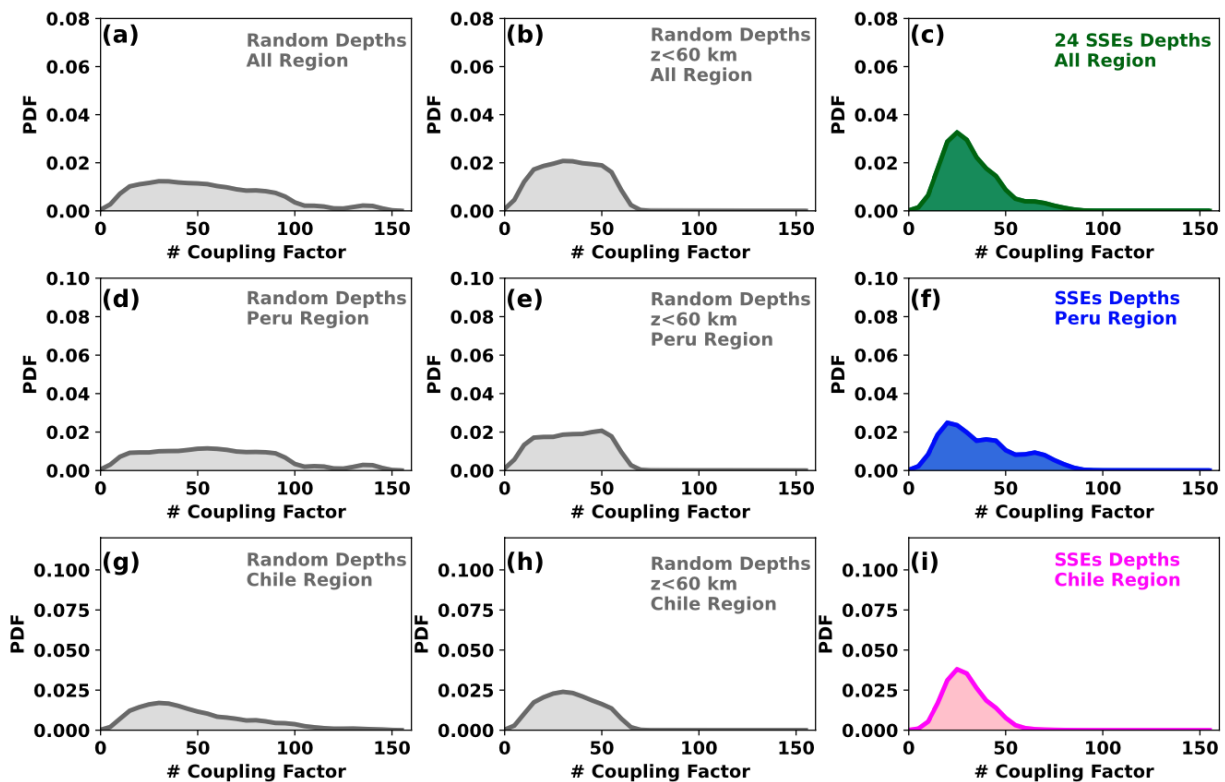


Figure S54. Depth Probability Density Functions (PDF) for 24 detected events/random picks. (a) Random picks PDF for the entire region, with the dark gray line representing the Kernel Density Estimation (KDE). (b) same as (a), but for depths shallower than 60km. (c) same as (a), but for the depths of our detected events. (d), (e), and (f) same as (a), (b), and (c) for the Peruvian regions, while (g), (h), (i) for the Chilean regions.

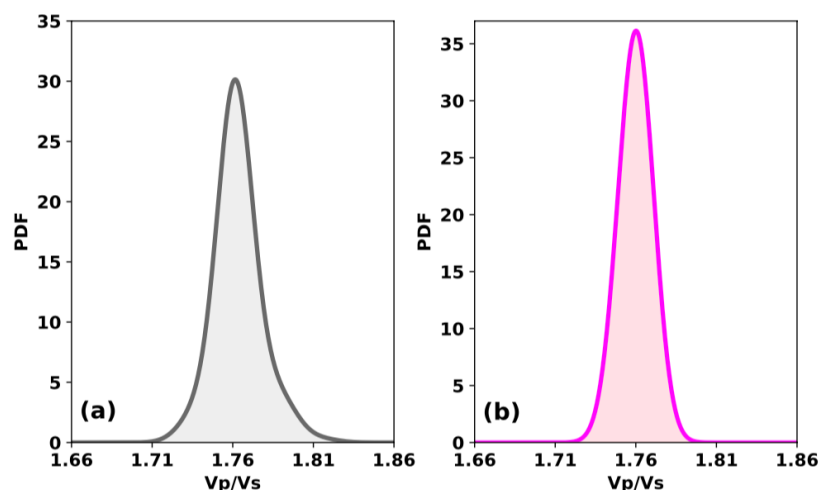


Figure S55. V_p/V_s ratio Probability Density Functions (PDF) and KDE for random picks (a) and 18 detected events (b).

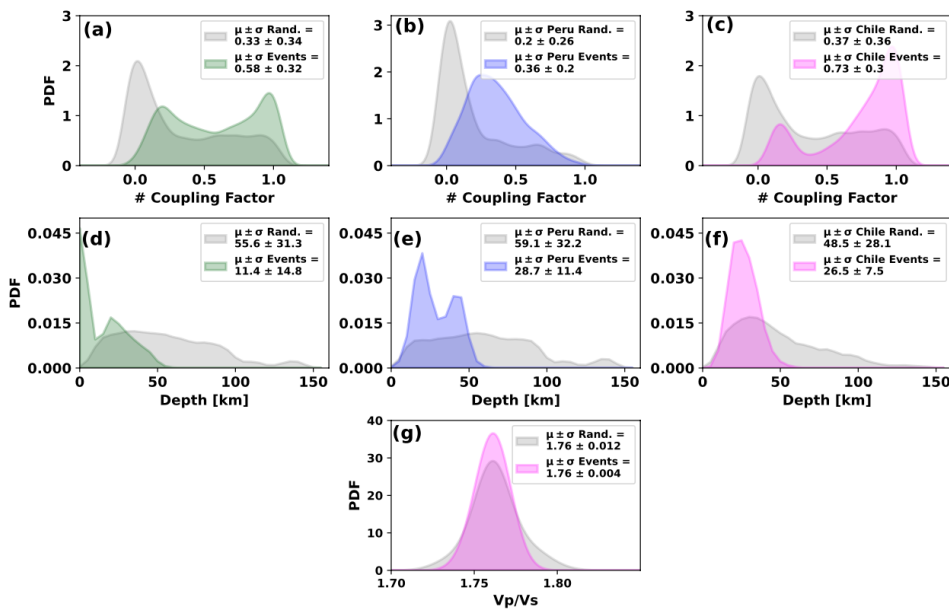


Figure S56. Coupling, depth, and V_p/V_s ratio of the 10 detected aseismic slip A events. (a) Probability Density Functions (PDF) of 1000 coupling models for 10 random picks (gray) and PDF of coupling where 10 aseismic slip events are detected (green), with respective mean (μ) and standard deviations (σ). (b) and (c) are the same as (a) for the Peru region only (gray: random, blue: SSEs) and northern Chile only (gray: random, magenta: events), respectively. (d) PDF of the depths of 10 random events (gray) and aseismic slip events detected in the region (green). (e) and (f) Same as (d) but for Peru (gray: random, blue: events) and Chile (gray, magenta) regions. (g) PDF of the V_p/V_s ratio for the Chilean region (gray, 10 random events), and detected aseismic events in Chile (magenta).

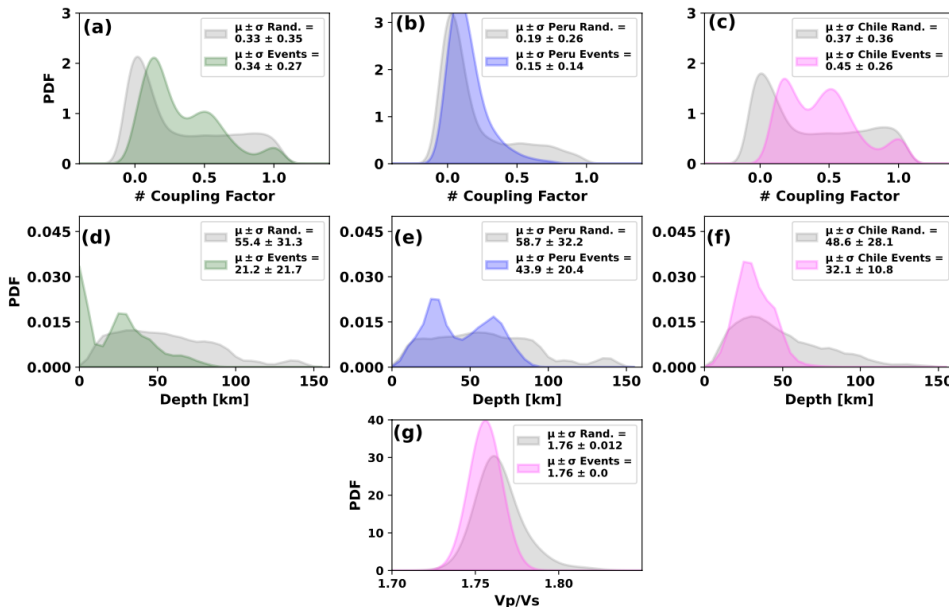


Figure S57. Same as Figure S56, for 14 events classified as B.

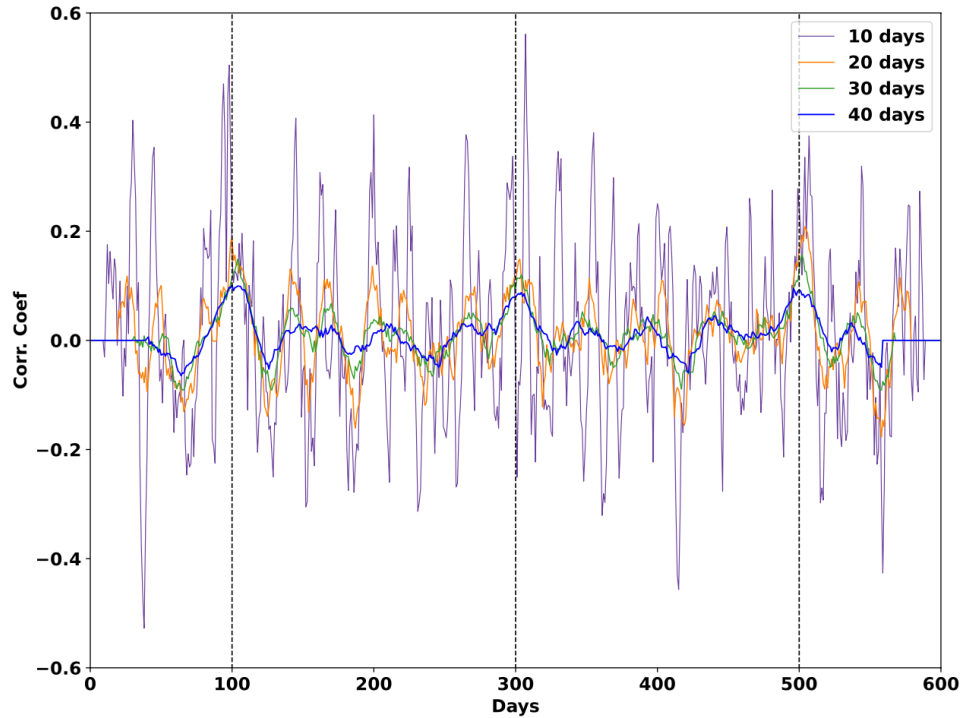


Figure S58. Correlation functions for various templates duration: 10 (purple), 20 (orange), 30 (green), and 40 (blue) days. Vertical dashed lines indicate the center of the synthetics with a slip equivalent to a SSEs of M_w 6.0 and duration of 10 (day 100), 20 (day 300) and 30 (day 500) days. Tested patch location aligns with Figure S31.

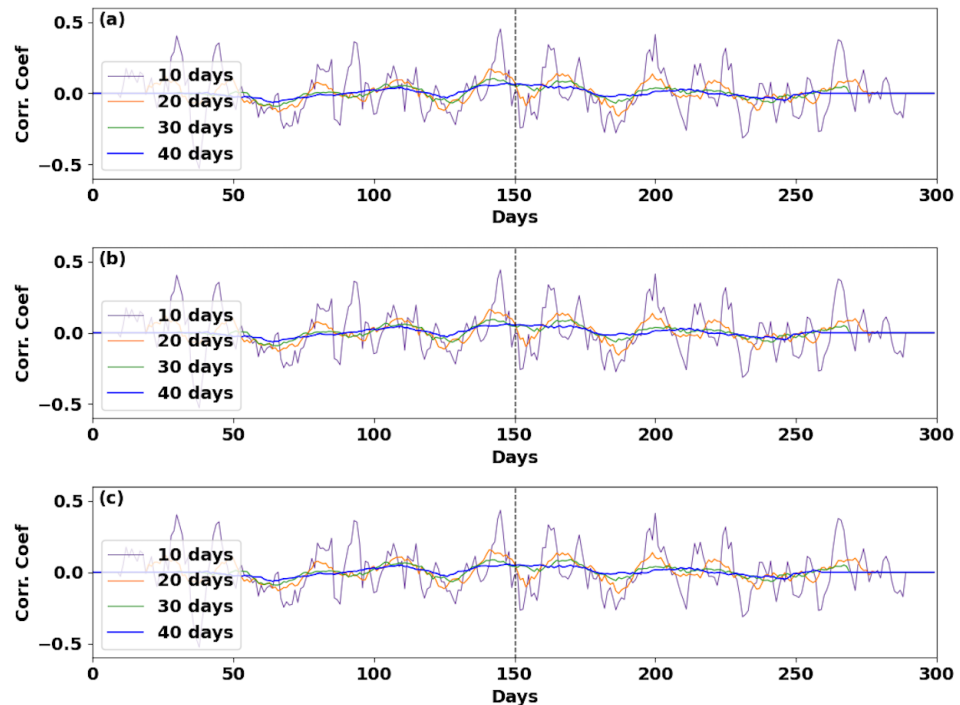


Figure S59. Same caption as Figure S58, but with synthetic events lasting for 60 (a), 80 (b), and 100 (c) days, centered on day 150.

Table S1. Estimated cGPS location and velocity field with their respective uncertainties for the stations analized in this study. Velocities are referred to SOAM fixed reference frame proposed by Nocquet et al. (2014). Velocities and errors are in mm/yr.

Station	Longitude($^{\circ}$)	Latitude($^{\circ}$)	$V_n \pm \sigma_{V_n}$ [mm/yr]	$V_e \pm \sigma_{V_e}$ [mm/yr]	$V_u \pm \sigma_{V_u}$ [mm/yr]
AEDA	-70.18	-20.55	6.58 ± 0.27	24.88 ± 0.35	-6.91 ± 0.94
AREQ	-71.49	-16.47	2.6 ± 0.2	12.7 ± 0.23	-1.33 ± 0.52
ATIC	-73.7	-16.23	2.05 ± 0.7	24.71 ± 0.82	0.58 ± 2.01
ATJN	-70.14	-19.3	5.18 ± 0.33	23.68 ± 0.36	1.4 ± 0.79
CBAA	-68.45	-22.75	4.88 ± 0.46	20.21 ± 0.73	-2.68 ± 1.03
CDLC	-69.76	-22.19	6.93 ± 0.42	30.89 ± 0.51	3.55 ± 0.65
CGTC	-70.07	-20.18	5.27 ± 0.56	25.31 ± 0.67	1.54 ± 1.37
CHMZ	-69.19	-19.67	6.67 ± 0.43	20.85 ± 0.48	-0.04 ± 0.96
CHRA	-72.93	-16.52	2.62 ± 0.76	19.24 ± 0.94	1.47 ± 3.45
CJNT	-67.76	-23.03	3.68 ± 0.33	16.81 ± 0.38	-0.51 ± 0.69
CLLA	-69.36	-20.95	4.74 ± 0.47	25.06 ± 0.54	-0.47 ± 1.21
COLC	-68.64	-19.28	5.52 ± 0.42	19.03 ± 0.49	-0.36 ± 1.26
COLL	-68.65	-20.83	1.64 ± 1.93	24.4 ± 2.05	4.25 ± 4.52
CRSC	-70.08	-20.92	7.62 ± 0.33	28.72 ± 0.39	0.86 ± 0.75
CTLR	-70.1	-21.96	8.5 ± 0.41	30.25 ± 0.44	5.68 ± 1.13
DANC	-70.25	-17.26	4.21 ± 1.04	10.34 ± 1.29	-3.25 ± 2.78
ENAP	-76.29	-13.8	1.92 ± 0.81	28.81 ± 1.0	-3.98 ± 2.63
FBAQ	-69.76	-20.14	6.32 ± 0.27	24.86 ± 0.33	4.16 ± 0.79
GLRV	-74.4	-14.67	3.94 ± 0.99	11.34 ± 1.2	-0.9 ± 2.57
GUAD	-75.79	-14.0	1.62 ± 0.46	18.58 ± 0.58	1.31 ± 1.55
HMBS	-69.89	-20.28	4.51 ± 0.39	21.96 ± 0.47	-2.68 ± 1.36
HUAN	-75.32	-12.04	1.37 ± 2.08	9.77 ± 2.55	-0.39 ± 6.65
IQQE	-70.13	-20.27	6.17 ± 0.24	25.5 ± 0.27	-0.37 ± 0.66
JRGN	-70.58	-23.29	10.93 ± 0.33	34.15 ± 0.4	-5.69 ± 0.83
LAGN	-70.7	-15.72	16.88 ± 5.25	66.18 ± 5.62	155.65 ± 17.28
LAGU	-76.27	-14.14	3.82 ± 0.46	28.47 ± 0.56	-7.82 ± 1.32
LOMI	-75.85	-14.71	-9.07 ± 1.28	14.09 ± 1.38	4.95 ± 3.09
LYAR	-70.57	-18.13	2.3 ± 0.42	17.62 ± 0.48	2.67 ± 1.21
MCLA	-70.25	-22.75	8.28 ± 0.33	30.34 ± 0.36	-0.61 ± 0.89
MICA	-69.83	-21.72	6.72 ± 0.72	30.18 ± 0.77	5.23 ± 1.72
MNMI	-69.6	-19.13	7.03 ± 0.39	19.99 ± 0.45	-0.87 ± 1.07
NZCA	-74.96	-14.86	4.41 ± 0.71	14.16 ± 0.96	0.65 ± 2.34
PALC	-69.96	-17.78	4.7 ± 1.04	11.95 ± 1.19	-1.68 ± 2.91

Table S2. Continuation of Table S1, with the same caption.

Station	Longitude($^{\circ}$)	Latitude($^{\circ}$)	$V_n \pm \sigma_{V_n}$ [mm/yr]	$V_e \pm \sigma_{V_e}$ [mm/yr]	$V_u \pm \sigma_{V_u}$ [mm/yr]
PB01	-69.49	-21.04	6.0 ± 0.42	26.84 ± 0.49	-1.09 ± 1.25
PB02	-69.89	-21.32	7.78 ± 0.42	29.77 ± 0.48	1.44 ± 1.12
PB03	-69.75	-22.05	6.94 ± 0.42	29.81 ± 0.67	2.96 ± 1.24
PB04	-70.15	-22.34	9.01 ± 0.42	29.61 ± 0.54	-0.53 ± 1.42
PB05	-70.2	-22.85	9.04 ± 0.42	30.05 ± 0.63	-0.58 ± 1.29
PB06	-69.57	-22.71	5.08 ± 0.59	25.97 ± 0.66	-1.49 ± 1.66
PB07	-69.89	-21.73	7.31 ± 0.58	30.08 ± 0.74	3.85 ± 1.69
PB08	-69.16	-20.14	6.11 ± 0.58	21.79 ± 1.26	0.47 ± 1.38
PB11	-69.66	-19.76	14.82 ± 1.97	35.36 ± 2.87	-14.42 ± 5.19
PCCL	-70.11	-18.46	4.72 ± 0.33	16.98 ± 0.41	1.0 ± 0.91
PCHA	-69.43	-19.87	5.86 ± 0.32	22.02 ± 0.37	1.07 ± 0.92
PICC	-69.33	-20.49	5.88 ± 0.2	23.19 ± 0.28	1.72 ± 0.48
PMCA	-70.91	-17.95	1.44 ± 1.03	18.73 ± 1.3	0.8 ± 3.55
PMEJ	-70.45	-23.1	9.17 ± 0.27	31.92 ± 0.36	-3.56 ± 0.78
PSGA	-70.12	-19.6	5.79 ± 0.39	24.55 ± 0.45	2.1 ± 1.16
PTCL	-71.37	-17.7	0.45 ± 0.42	20.97 ± 0.5	7.76 ± 1.59
PTIN	-74.31	-15.84	3.6 ± 1.06	24.02 ± 1.21	1.47 ± 3.32
PTRE	-69.57	-18.19	6.77 ± 0.33	12.21 ± 0.38	-2.58 ± 0.82
QUCA	-72.43	-16.71	-2.7 ± 1.51	14.94 ± 1.75	10.62 ± 4.61
QUIL	-69.56	-21.69	6.1 ± 0.67	31.14 ± 0.85	7.39 ± 1.6
RADO	-68.93	-22.08	5.44 ± 0.42	23.14 ± 0.5	6.58 ± 1.04
SJUA	-75.19	-15.36	-1.72 ± 0.76	27.0 ± 0.95	-7.63 ± 2.24
SLRZ	-77.21	-12.08	4.18 ± 1.51	22.77 ± 1.93	2.6 ± 4.49
SRGD	-69.35	-22.87	4.74 ± 0.37	27.2 ± 0.41	-0.15 ± 1.02
TORA	-70.85	-17.08	0.46 ± 1.04	7.6 ± 1.35	2.74 ± 3.32
TQPL	-70.64	-17.3	2.64 ± 0.57	11.54 ± 0.67	0.76 ± 1.52
TRTA	-70.04	-17.48	4.77 ± 0.53	9.31 ± 0.6	-1.72 ± 1.57
UAPE	-70.14	-20.24	5.51 ± 0.2	27.07 ± 0.23	0.94 ± 0.72
UCNF	-70.41	-23.68	9.72 ± 0.27	32.8 ± 0.32	0.52 ± 0.77
URCU	-70.15	-21.76	8.42 ± 3.08	57.44 ± 3.29	45.56 ± 7.45
UTAR	-70.3	-18.49	4.38 ± 0.27	18.36 ± 0.34	3.29 ± 0.85
VLZL	-69.96	-23.12	6.71 ± 0.36	30.1 ± 0.42	3.77 ± 0.85

Table S3. North, East, and Vertical Annual Amplitudes (in m) and Phases (in yr) estimated for each cGPS.

Station	N Amp.	N Phase	E Amp.	E Phase	U Amp.	U. Phase
AEDA	0.0016	0.0162	0.0013	-0.0794	0.0013	0.4266
AREQ	0.0011	0.0414	0.0017	-0.0458	0.0038	0.4871
ATIC	0.0014	0.0982	0.0017	-0.0449	0.0024	-0.4888
ATJN	0.0015	0.0424	0.0017	-0.0240	0.0028	0.4640
CBAA	0.0015	0.0456	0.0014	-0.0811	0.0022	0.4464
CDLC	0.0015	0.0251	0.0016	-0.0639	0.0016	0.4580
CGTC	0.0012	0.0306	0.0017	-0.0672	0.0030	-0.4994
CHMZ	0.0014	0.0161	0.0016	-0.0773	0.0035	0.4642
CHRA	0.0013	0.0872	0.0023	-0.0290	0.0039	-0.4939
CJNT	0.0014	0.0415	0.0014	-0.0508	0.0024	0.3933
CLLA	0.0015	0.0237	0.0016	-0.0755	0.0018	0.4670
COLC	0.0010	0.0099	0.0018	-0.0278	0.0021	0.3512
COLL	0.0015	0.1258	0.0021	0.0038	0.0047	0.1848
CRSC	0.0014	0.0334	0.0015	-0.0520	0.0024	0.4549
CTLR	0.0012	0.0017	0.0015	-0.0601	0.0015	0.4569
DANC	0.0015	0.0502	0.0021	-0.0518	0.0050	-0.4924
ENAP	0.0012	0.0825	0.0012	-0.0504	0.0018	0.3634
FBAQ	0.0021	0.0566	0.0017	-0.1008	0.0015	0.3763
GLRV	0.0014	0.1513	0.0030	-0.0532	0.0035	-0.4190
GUAD	0.0013	0.0677	0.0015	-0.0611	0.0023	0.4183
HMBS	0.0012	-0.1169	0.0018	-0.2186	0.0046	-0.4534
HUAN	0.0020	0.0938	0.0034	-0.0544	0.0060	-0.4765
IQQE	0.0012	0.0166	0.0017	-0.0517	0.0019	0.4416
JRGN	0.0016	0.0369	0.0013	-0.0306	0.0014	0.4650
LAGN	0.0027	-0.3551	0.0165	-0.2868	0.0444	-0.3345
LAGU	0.0011	0.1104	0.0017	-0.0636	0.0006	0.3032
LOMI	0.0022	-0.0343	0.0022	-0.0635	0.0025	-0.4937
LYAR	0.0015	0.0527	0.0016	-0.0516	0.0027	0.4611
MCLA	0.0012	0.0345	0.0013	-0.0462	0.0019	0.4367
MICA	0.0013	0.0069	0.0014	-0.0373	0.0027	0.4367
MNMI	0.0015	0.0046	0.0016	-0.0638	0.0019	0.4419
NZCA	0.0015	0.1029	0.0025	-0.0469	0.0026	0.4738
PALC	0.0017	0.0545	0.0020	-0.0857	0.0052	-0.4219

Table S4. Continuation of Table S3, with the same caption.

Station	N Amp.	N Phase	E Amp.	E Phase	U Amp.	U. Phase
PB01	0.0015	0.0190	0.0016	-0.0708	0.0018	0.4205
PB02	0.0016	0.0531	0.0016	-0.0742	0.0013	-0.4631
PB03	0.0016	0.0681	0.0013	-0.0798	0.0016	0.3475
PB04	0.0014	0.0294	0.0014	-0.0578	0.0014	0.3532
PB05	0.0013	0.0475	0.0015	-0.0795	0.0011	0.3318
PB06	0.0013	0.0254	0.0012	-0.0486	0.0016	0.4344
PB07	0.0016	0.0397	0.0014	-0.0630	0.0019	-0.4946
PB08	0.0016	0.0524	0.0017	-0.0726	0.0027	-0.4895
PB11	0.0027	-0.1294	0.0054	-0.2108	0.0033	0.3441
PCCL	0.0017	0.0445	0.0017	-0.0568	0.0031	0.4528
PCHA	0.0015	0.0247	0.0014	-0.0681	0.0027	0.4948
PICC	0.0013	0.0666	0.0015	-0.0711	0.0022	0.4310
PMCA	0.0014	0.0658	0.0019	-0.0358	0.0025	-0.4501
PMEJ	0.0014	0.0638	0.0015	-0.0399	0.0009	0.3783
PSGA	0.0012	0.0056	0.0014	-0.0170	0.0020	0.4359
PTCL	0.0019	0.0429	0.0025	-0.0290	0.0033	0.3849
PTIN	0.0011	0.0802	0.0020	-0.0190	0.0035	-0.4515
PTRE	0.0017	0.0563	0.0018	-0.0442	0.0042	-0.4830
QUCA	0.0017	0.0777	0.0019	-0.0542	0.0069	-0.4770
QUIL	0.0020	0.0378	0.0009	-0.0146	0.0032	0.2984
RADO	0.0013	0.0650	0.0015	-0.0797	0.0039	0.3944
SJUA	0.0014	0.0856	0.0023	-0.0348	0.0016	-0.4612
SLRZ	0.0008	-0.1344	0.0027	-0.0672	0.0039	0.4830
SRGD	0.0013	0.0349	0.0015	-0.0551	0.0019	0.4436
TORA	0.0020	0.0763	0.0026	-0.0666	0.0045	0.4507
TQPL	0.0015	0.0538	0.0018	-0.0489	0.0043	-0.4958
TRTA	0.0023	0.0037	0.0023	-0.0695	0.0046	0.4965
UAPE	0.0011	0.0156	0.0017	-0.0806	0.0022	0.3477
UCNF	0.0013	0.0316	0.0012	0.0122	0.0011	0.3725
URCU	0.0014	0.0586	0.0040	-0.0753	0.0032	-0.0423
UTAR	0.0015	0.0623	0.0018	-0.0601	0.0028	0.4689
VLZL	0.0012	0.0330	0.0013	-0.0567	0.0020	0.4331

Table S5. North, East and Vertical Semi-annual Amplitudes (in m) and Phases (in yr) estimated for each cGPS.

Station	N Amp.	N Phase	E Amp.	E Phase	U Amp.	U. Phase
AEDA	0.0002	0.1866	0.0003	-0.4243	0.0009	0.3124
AREQ	0.0003	0.2717	0.0003	-0.2246	0.0008	0.4931
ATIC	0.0002	-0.2018	0.0003	0.1946	0.0010	0.3377
ATJN	0.0002	0.2785	0.0004	-0.2441	0.0006	-0.3965
CBAA	0.0001	-0.4692	0.0005	-0.1829	0.0002	-0.0889
CDLC	0.0001	-0.1612	0.0004	-0.1519	0.0003	-0.0412
CGTC	0.0001	0.1150	0.0002	-0.0427	0.0008	0.3254
CHMZ	0.0001	-0.4736	0.0004	-0.2201	0.0008	-0.3745
CHRA	0.0002	-0.4347	0.0005	0.0974	0.0019	0.0742
CJNT	0.0000	0.2238	0.0004	-0.2483	0.0009	-0.4034
CLLA	0.0001	-0.4951	0.0004	-0.1331	0.0003	-0.0145
COLC	0.0001	0.0252	0.0007	-0.1952	0.0005	-0.4986
COLL	0.0015	0.3436	0.0008	-0.3487	0.0013	-0.4402
CRSC	0.0001	0.3523	0.0004	-0.2203	0.0004	-0.3679
CTLR	0.0000	0.3193	0.0004	-0.1701	0.0006	-0.1725
DANC	0.0003	-0.2464	0.0006	-0.1014	0.0014	0.3635
ENAP	0.0004	0.3537	0.0010	-0.0390	0.0018	-0.1473
FBAQ	0.0003	0.3077	0.0000	0.4209	0.0006	-0.3162
GLRV	0.0002	-0.0310	0.0004	-0.0282	0.0009	0.3476
GUAD	0.0001	-0.3365	0.0006	-0.2546	0.0006	0.3319
HMBS	0.0004	-0.4665	0.0016	-0.2112	0.0031	-0.2838
HUAN	0.0003	0.2605	0.0014	0.2049	0.0026	0.1914
IQQE	0.0001	0.2770	0.0002	-0.0885	0.0003	0.2092
JRGN	0.0000	0.4721	0.0004	-0.2650	0.0003	-0.2789
LAGN	0.0015	0.3021	0.0045	0.3662	0.0104	0.3565
LAGU	0.0001	-0.4607	0.0005	-0.1582	0.0016	0.0070
LOMI	0.0010	-0.1963	0.0006	-0.2789	0.0024	0.3730
LYAR	0.0002	0.2596	0.0003	-0.1682	0.0002	0.1240
MCLA	0.0001	0.4202	0.0004	-0.2161	0.0001	-0.4864
MICA	0.0003	-0.4727	0.0004	-0.2371	0.0008	-0.1771
MNMI	0.0002	0.2083	0.0002	-0.1722	0.0001	0.0403
NZCA	0.0003	-0.1465	0.0003	-0.0267	0.0013	0.2894
PALC	0.0004	-0.1290	0.0003	-0.1765	0.0012	0.3270

Table S6. Continuation of Table S5, with the same caption.

Station	N Amp.	N Phase	E Amp.	E Phase	U Amp.	U. Phase
PB01	0.0002	0.2016	0.0005	-0.1794	0.0005	-0.2579
PB02	0.0001	0.2339	0.0005	-0.2289	0.0002	-0.2852
PB03	0.0001	0.1569	0.0003	-0.1748	0.0001	0.3786
PB04	0.0001	0.1420	0.0004	-0.2094	0.0000	0.0101
PB05	0.0002	0.2583	0.0004	-0.1998	0.0004	-0.1579
PB06	0.0001	-0.0369	0.0004	-0.0642	0.0000	-0.4482
PB07	0.0001	-0.0333	0.0001	-0.2858	0.0007	0.2873
PB08	0.0003	0.1175	0.0001	-0.0154	0.0009	0.4606
PB11	0.0004	0.4367	0.0016	-0.3558	0.0005	0.4813
PCCL	0.0002	0.2726	0.0005	-0.2076	0.0004	-0.3198
PCHA	0.0001	0.2282	0.0004	-0.2109	0.0004	-0.4743
PICC	0.0001	0.4362	0.0002	-0.0603	0.0005	0.1829
PMCA	0.0002	0.0320	0.0000	0.0805	0.0015	0.2584
PMEJ	0.0002	0.3540	0.0004	-0.2161	0.0004	-0.1396
PSGA	0.0001	0.4202	0.0005	-0.2157	0.0004	-0.3308
PTCL	0.0003	0.2307	0.0009	-0.1031	0.0009	-0.1243
PTIN	0.0006	-0.3273	0.0002	0.0010	0.0009	0.2210
PTRE	0.0002	0.2664	0.0004	-0.2187	0.0008	-0.4614
QUCA	0.0006	-0.3057	0.0003	-0.1524	0.0018	0.1239
QUIL	0.0012	0.2759	0.0006	-0.3173	0.0009	-0.3264
RADO	0.0001	0.4173	0.0002	-0.2779	0.0006	-0.4191
SJUA	0.0003	0.0304	0.0002	0.2591	0.0010	0.3519
SLRZ	0.0005	-0.3147	0.0003	-0.1103	0.0006	0.1642
SRGD	0.0001	0.4359	0.0005	-0.1849	0.0003	-0.0422
TORA	0.0002	-0.1986	0.0001	0.3382	0.0015	-0.1752
TQPL	0.0001	-0.2405	0.0005	-0.2289	0.0013	0.3776
TRTA	0.0004	-0.2210	0.0006	-0.2749	0.0009	0.3582
UAPE	0.0003	0.2981	0.0004	-0.2906	0.0003	0.2340
UCNF	0.0003	0.4075	0.0004	-0.0841	0.0006	0.1220
URCU	0.0004	-0.4969	0.0016	-0.0997	0.0027	-0.1403
UTAR	0.0001	-0.2763	0.0006	-0.2597	0.0011	0.3678
VLZL	0.0001	0.2456	0.0004	-0.2174	0.0002	-0.3718

Table S7. Relaxation time estimated using a Trajectory Model for each earthquake $M_w \geq 7.5$ in the study area.

Earthquake	τ (days)
Arequipa	114
Tarapaca	70
Pisco	27
Tocopilla	89
Iquique	20

Table S8. Coseismic and Postseismic (PS) offsets values estimated using a Trajectory Model for Arequipa earthquake ($M_w 8.4$, 23/06/2001) in south Peru. Values are in mm.

Station	$N \pm \sigma_N$	$E \pm \sigma_E$	$U \pm \sigma_U$	$N PS \pm \sigma_{NPS}$	$E PS \pm \sigma_{EPS}$	$U PS \pm \sigma_{UPS}$
AREQ	-288.38 ± 1.41	-418.67 ± 2.36	-26.39 ± 1.11	-88.11 ± 0.72	-126.9 ± 1.32	39.14 ± 0.60
UAPE	-2.18 ± 1.60	2.89 ± 3.03	5.26 ± 1.54	-	-	-

Table S9. Coseismic and Postseismic (PS) offsets values estimated using a Trajectory Model for Tarapaca earthquake (M_w 7.8, 13/06/2005) in north Chile. Values are in mm.

Station	$N \pm \sigma_N$	$E \pm \sigma_E$	$U \pm \sigma_U$	$N PS \pm \sigma_{NPS}$	$E PS \pm \sigma_{EPS}$	$U PS \pm \sigma_{UPS}$
AREQ	-0.39 ± 0.15	-2.64 ± 0.30	-1.509 ± 0.13	-	-	-
AEDA	-23.04 ± 0.85	-42.12 ± 1.79	29.16 ± 0.83	-1.56 ± 0.74	-2.39 ± 1.54	9.04 ± 0.72
COLL	36.80 ± 0.66	-20.79 ± 1.22	-22.39 ± 0.61	1.67 ± 1.45	-9.42 ± 2.70	-19.07 ± 1.35
FBAQ	1.18 ± 0.34	-14.94 ± 0.65	4.39 ± 0.32	-4.63 ± 0.50	-9.98 ± 0.96	-3.98 ± 0.47
IQQE	-13.61 ± 0.35	-48.13 ± 0.68	41.13 ± 0.33	-1.18 ± 0.22	-12.89 ± 0.44	1.79 ± 0.21
PICC	33.81 ± 0.22	-7.13 ± 0.41	-54.80 ± 0.21	-4.97 ± 0.30	-8.55 ± 0.56	-0.91 ± 0.28
PMEJ	-1.65 ± 0.24	-1.06 ± 0.49	1.63 ± 0.25	1.40 ± 0.42	-2.86 ± 0.84	-4.58 ± 0.44
QUIL	3.16 ± 0.48	-3.07 ± 0.94	3.16 ± 0.50	-0.65 ± 1.00	-6.85 ± 1.96	-17.61 ± 1.05
UAPE	-13.95 ± 0.41	-48.44 ± 0.78	38.38 ± 0.39	-2.58 ± 0.28	-7.90 ± 0.55	-7.50 ± 0.27
UCNF	0.12 ± 0.27	-3.32 ± 0.53	-3.09 ± 0.29	-	-	-
UTAR	1.74 ± 0.45	-4.34 ± 0.93	4.70 ± 0.42	-0.26 ± 0.41	-3.55 ± 0.84	-2.94 ± 0.38

Table S10. Coseismic and Postseismic (PS) offsets values estimated using a Trajectory Model for Pisco earthquake (M_w 8.0, 15/08/2007) in south Peru. Values are in mm.

Station	$N \pm \sigma_N$	$E \pm \sigma_E$	$U \pm \sigma_U$	$N PS \pm \sigma_{NPS}$	$E PS \pm \sigma_{EPS}$	$U PS \pm \sigma_{UPS}$
AREQ	2.23 ± 0.20	-2.76 ± 0.39	1.07 ± 0.16	0.16 ± 0.27	-5.13 ± 0.51	3.29 ± 0.22
AEDA	1.91 ± 0.36	1.47 ± 0.77	0.21 ± 0.36	-	-	-
ATJN	1.66 ± 0.18	0.07 ± 0.33	0.26 ± 0.16	-	-	-
CHMZ	1.31 ± 0.32	0.79 ± 0.54	3.20 ± 0.28	-	-	-
CRSC	0.56 ± 0.18	0.01 ± 0.33	1.89 ± 0.17	-	-	-
CTLR	0.84 ± 0.47	1.24 ± 0.90	3.58 ± 0.45	-	-	-
ENAP	0.00 ± 0.00	0.00 ± 0.00	0.00 ± 0.00	6.60 ± 1.86	-67.91 ± 4.42	39.66 ± 1.61
GUAD	0.00 ± 0.00	0.00 ± 0.00	0.00 ± 0.00	-34.45 ± 0.49	-74.30 ± 1.02	-25.60 ± 0.41
HMBS	0.18 ± 0.31	-4.57 ± 0.67	-1.37 ± 0.30	-	-	-
JRGN	1.23 ± 0.19	-0.84 ± 0.35	2.364 ± 0.19	-	-	-
LAGU	0.00 ± 0.00	0.00 ± 0.00	0.00 ± 0.00	-37.14 ± 0.45	-111.42 ± 0.99	61.43 ± 0.39
MCLA	0.97 ± 0.18	-0.30 ± 0.34	1.07 ± 0.19	-	-	-
MNMI	1.95 ± 0.70	-1.31 ± 1.36	-1.84 ± 0.65	-	-	-
PCCL	1.67 ± 0.15	-0.47 ± 0.27	-0.57 ± 0.14	-	-	-
PCHA	2.57 ± 0.29	-0.95 ± 0.58	-0.76 ± 0.27	-	-	-
PICC	1.88 ± 0.24	1.301 ± 0.47	1.71 ± 0.23	-	-	-
PMEJ	2.03 ± 0.25	-0.13 ± 0.50	-1.79 ± 0.26	-	-	-
PSGA	1.56 ± 0.26	0.87 ± 0.53	-2.01 ± 0.25	-	-	-
PTRE	2.07 ± 0.14	-1.36 ± 0.22	0.39 ± 0.12	-	-	-
QUIL	3.19 ± 0.60	-0.59 ± 1.18	-3.60 ± 0.63	-	-	-
SRGD	1.26 ± 0.18	-0.35 ± 0.29	1.25 ± 0.17	-	-	-
UAPE	0.99 ± 0.21	0.65 ± 0.41	2.34 ± 0.20	-	-	-
UTAR	0.46 ± 0.26	-0.97 ± 0.52	-2.50 ± 0.24	-	-	-
VLZL	0.97 ± 0.23	-1.30 ± 0.44	-0.02 ± 0.24	-	-	-

Table S11. Coseismic and Postseismic (PS) offsets values estimated using a Trajectory Model for Tocopilla earthquake (M_w 7.7, 14/11/2007) in north Chile. Values are in mm.

Station	$N \pm \sigma_N$	$E \pm \sigma_E$	$U \pm \sigma_U$	$N PS \pm \sigma_{NPS}$	$E PS \pm \sigma_{EPS}$	$U PS \pm \sigma_{UPS}$
AEDA	0.18 ± 2.08	0.43 ± 4.44	9.13 ± 2.05	-1.92 ± 1.27	1.44 ± 2.67	21.00 ± 1.26
AREQ	0.62 ± 0.25	1.14 ± 0.49	-1.79 ± 0.21	-	-	-
ATJN	0.1 ± 0.23	-1.98 ± 0.42	2.25 ± 0.21	-	-	-
CBAA	0.22 ± 0.50	-56.37 ± 0.87	-2.7 ± 0.49	-3.16 ± 0.31	-24.66 ± 0.53	9.63 ± 0.30
CDLC	-43.60 ± 2.28	-105.00 ± 4.01	-77.10 ± 2.07	-812.34 ± 294.56	1545.88 ± 510.81	-1232.04 ± 279.52
CHMZ	-1.46 ± 0.19	-2.24 ± 0.32	1.96 ± 0.17	-	-	-
CJNT	-3.26 ± 1.53	-11.69 ± 2.58	-0.74 ± 1.47	-1492.52 ± 244.60	1425.28 ± 406.30	448.75 ± 232.39
COLC	-0.84 ± 0.96	-1.45 ± 1.78	-2.24 ± 0.87	-	-	-
CRSC	-0.02 ± 1.27	-1.88 ± 2.39	-2.85 ± 1.20	-0.64 ± 0.38	-2.30 ± 0.69	7.66 ± 0.36
CTLR	6.25 ± 0.35	-16.56 ± 0.67	81.86 ± 0.35	-3.46 ± 0.62	-6.67 ± 1.18	-7.95 ± 0.61
JRGN	-120.78 ± 5.80	-183.33 ± 10.67	168.70 ± 5.33	-1732.04 ± 255.19	-5241.34 ± 470.35	4025.55 ± 256.94
LYAR	0.68 ± 0.36	-1.68 ± 0.69	1.91 ± 0.34	-	-	-
MCLA	-72.58 ± 0.74	-95.29 ± 1.39	271.00 ± 0.74	443.04 ± 40.55	-93.33 ± 75.09	-12.21 ± 40.52
MICA	0.00 ± 0.00	0.00 ± 0.00	0.00 ± 0.00	-3.07 ± 0.81	-7.30 ± 1.58	-1.96 ± 0.82
PB01	0.00 ± 0.00	0.00 ± 0.00	0.00 ± 0.00	-4.80 ± 0.39	-7.93 ± 0.66	10.61 ± 0.37
PB02	0.000 ± 0.00	0.00 ± 0.00	0.00 ± 0.00	-3.46 ± 0.38	-5.50 ± 0.68	8.05 ± 0.37
PB03	0.00 ± 0.00	0.00 ± 0.00	0.00 ± 0.00	-5.74 ± 0.51	-14.08 ± 0.94	-0.40 ± 0.50
PB04	0.00 ± 0.00	0.00 ± 0.00	0.00 ± 0.00	-7.56 ± 0.26	-5.59 ± 0.45	12.02 ± 0.25
PB05	0.00 ± 0.00	0.00 ± 0.00	0.00 ± 0.00	-8.01 ± 0.43	-22.38 ± 0.83	11.91 ± 0.44
PCCL	0.8 ± 0.19	-0.77 ± 0.34	1.05 ± 0.17	-	-	-
PCHA	-2.02 ± 0.39	-2.06 ± 0.77	-1.81 ± 0.35	-	-	-
PSGA	0.9 ± 0.27	-1.72 ± 0.55	2.73 ± 0.26	-	-	-
PMEJ	-96.94 ± 5.71	-256.66 ± 10.94	246.00 ± 5.35	-2298.53 ± 339.29	-6283.96 ± 671.34	9991.06 ± 353.25

Table S12. Coseismic and Postseismic (PS) offsets values estimated using a Trajectory Model for Tocopilla earthquake (M_w 7.7, 14/11/2007) in north Chile. Values are in mm. Continuation of Tables S11.

Station	$N \pm \sigma_N$	$E \pm \sigma_E$	$U \pm \sigma_U$	$N PS \pm \sigma_{NPS}$	$E PS \pm \sigma_{EPS}$	$U PS \pm \sigma_{UPS}$
QUIL	-49.21 ± 16.28	-52.27 ± 31.83	-61.40 ± 16.55	-2387.17 ± 3589.23	1895.46 ± 7035.72	-7178.01 ± 3650.50
PTRE	-0.97 ± 0.13	-1.04 ± 0.22	4.41 ± 0.12	-	-	-
RADO	0.00 ± 0.00	0.00 ± 0.00	0.00 ± 0.00	-7.30 ± 0.33	-22.17 ± 0.61	-22.84 ± 0.32
SRGD	-0.90 ± 2.40	-118.77 ± 4.39	-46.88 ± 2.23	-944.03 ± 277.28	1656.86 ± 468.87	339.83 ± 266.95
UAPE	1.07 ± 1.40	1.30 ± 2.69	1.62 ± 1.30	0.41 ± 0.38	-7.52 ± 0.73	3.90 ± 0.36
UTAR	1.36 ± 0.29	-0.82 ± 0.59	-0.22 ± 0.27	-	-	-
VLZL	-33.55 ± 1.04	-98.15 ± 2.00	-25.32 ± 1.05	297.00 ± 132.11	-19.35 ± 252.48	463.10 ± 135.13

Table S13. Coseismic and Postseismic (PS) offsets values estimated using a Trajectory Model for Iquique earthquake (M_w 8.1, 01/04/2014) in north Chile. Values are in mm.

Station	$N \pm \sigma_N$	$E \pm \sigma_E$	$U \pm \sigma_U$	$N\ PS \pm \sigma_{NPS}$	$E\ PS \pm \sigma_{EPS}$	$U\ PS \pm \sigma_{UPS}$
AEDA	-74.35 ± 1.83	-269.55 ± 3.46	102.67 ± 1.73	15.44 ± 20.52	-164.59 ± 40.30	42.48 ± 19.68
AREQ	3.41 ± 0.90	-1.63 ± 1.60	-2.00 ± 0.74	0.84 ± 0.21	0.22 ± 0.38	-1.56 ± 0.17
ATIC	-1.12 ± 1.10	2.52 ± 2.20	1.75 ± 0.93	1.61 ± 0.33	-0.64 ± 0.64	-3.53 ± 0.28
ATJN	-283.33 ± 1.67	-545.02 ± 3.13	-161.61 ± 1.51	-79.93 ± 18.30	-48.17 ± 34.67	-90.11 ± 16.56
CBAA	3.69 ± 1.04	-4.33 ± 1.70	-1.94 ± 0.96	0.06 ± 0.86	0.73 ± 1.46	2.52 ± 0.79
CGTC	67.09 ± 1.32	-413.22 ± 2.26	-83.97 ± 1.19	-65.47 ± 14.89	-85.01 ± 26.09	-87.29 ± 13.46
CHMZ	-30.89 ± 1.14	-235.81 ± 1.82	-12.26 ± 1.01	55.93 ± 22.09	-64.51 ± 36.53	-229.12 ± 19.51
CJNT	2.86 ± 0.99	-5.28 ± 1.58	-1.32 ± 0.91	-0.86 ± 0.33	1.95 ± 0.56	-1.44 ± 0.31
COLC	-26.89 ± 1.81	-112.09 ± 3.45	-0.10 ± 1.63	-53.10 ± 22.17	-227.95 ± 42.95	61.09 ± 19.97
CRSC	-14.01 ± 1.55	-80.81 ± 2.78	-0.22 ± 1.45	79.224 ± 19.59	-114.40 ± 35.98	0.10 ± 18.30
DANC	0.3 ± 1.21	0.24 ± 2.11	6.92 ± 1.01	-	-	-
IQQE	34.08 ± 1.43	-291.16 ± 2.84	-47.21 ± 1.35	-40.57 ± 15.94	-35.08 ± 32.04	-125.33 ± 14.95
JRGN	-0.85 ± 1.07	-1.26 ± 1.97	2.51 ± 1.08	-1.34 ± 0.24	1.32 ± 0.44	-6.83 ± 0.23
LYAR	-0.05 ± 1.45	-1.55 ± 2.66	6.76 ± 1.28	-6.67 ± 0.23	-8.14 ± 0.42	-7.92 ± 0.20
MCLA	1.52 ± 1.54	-3.24 ± 2.78	5.17 ± 1.51	44.745 ± 15.42	-34.41 ± 27.92	65.80 ± 15.09
MNMI	-126.38 ± 1.88	-257.32 ± 3.78	-18.92 ± 1.77	-108.63 ± 21.93	-283.76 ± 44.37	-152.61 ± 20.36
NZCA	0.2 ± 1.06	1.09 ± 2.16	3.92 ± 0.87	-	-	-
PB01	18.78 ± 1.17	-34.60 ± 1.90	-7.06 ± 1.06	-24.06 ± 13.59	-75.02 ± 22.66	21.02 ± 12.34
PB02	0.27 ± 1.24	-8.06 ± 2.10	-8.57 ± 1.15	-71.13 ± 13.94	26.48 ± 23.84	-1.35 ± 12.86
PB03	-1.27 ± 1.30	-0.48 ± 2.21	-3.21 ± 1.22	-47.36 ± 15.60	42.20 ± 27.54	-39.14 ± 14.78
PB04	-3.01 ± 1.13	0.89 ± 1.82	-1.34 ± 1.06	-38.37 ± 12.56	62.45 ± 20.69	-12.91 ± 11.77
PB05	-3.77 ± 1.33	1.93 ± 2.34	-0.28 ± 1.29	-37.10 ± 15.54	66.29 ± 27.85	26.56 ± 15.22
PB06	-2.79 ± 1.36	2.77 ± 2.36	3.50 ± 1.30	-28.20 ± 18.47	-14.96 ± 33.43	-213.91 ± 17.98
PB07	-1.40 ± 1.33	-3.11 ± 2.28	-6.72 ± 1.25	-24.44 ± 20.71	15.68 ± 36.19	36.12 ± 19.38
PB08	20.88 ± 1.60	-181.23 ± 2.87	-10.13 ± 1.46	-33.96 ± 18.80	-184.20 ± 34.39	-83.49 ± 17.23
PB11	-61.89 ± 1.67	-467.17 ± 3.06	-87.47 ± 1.51	3.54 ± 26.52	-119.24 ± 49.91	-33.11 ± 24.24

Table S14. Coseismic and Postseismic (PS) offsets values estimated using a Trajectory Model for Iquique earthquake (M_w 8.1, 01/04/2014) in north Chile. Values are in mm. Continuation of Tables S13.

Station	$N \pm \sigma_N$	$E \pm \sigma_E$	$U \pm \sigma_U$	$N\ PS \pm \sigma_{NPS}$	$E\ PS \pm \sigma_{EPS}$	$U\ PS \pm \sigma_{UPS}$
PALC	0.93 ± 2.06	-1.18 ± 4.83	2.71 ± 1.98	-	-	-
PCCL	-76.18 ± 1.58	-69.33 ± 2.89	-8.98 ± 1.38	-109.28 ± 15.85	-176.69 ± 28.91	-180.79 ± 13.90
PCHA	-8.67 ± 2.29	-318.70 ± 4.49	-33.65 ± 2.09	4.65 ± 28.25	-205.58 ± 55.86	47.23 ± 25.71
PICC	40.71 ± 1.27	-129.06 ± 2.19	-11.72 ± 1.17	-22.65 ± 13.99	-235.81 ± 23.76	-101.16 ± 12.51
PMCA	2.38 ± 2.26	-1.97 ± 4.58	-0.74 ± 2.01	-5.85 ± 12.23	-18.39 ± 25.26	-9.21 ± 10.87
PMEJ	-1.12 ± 1.13	-1.72 ± 2.17	-4.56 ± 1.16	-2.13 ± 0.26	1.86 ± 0.52	-1.95 ± 0.27
PSGA	-232.44 ± 1.78	-814.29 ± 3.56	-260.60 ± 1.67	-106.17 ± 19.78	-76.87 ± 40.14	23.03 ± 18.81
PTCL	2.07 ± 1.50	-1.90 ± 2.77	-8.70 ± 1.31	3.39 ± 0.27	-0.47 ± 0.53	-1.52 ± 0.24
PTRE	-55.26 ± 1.09	-50.91 ± 1.71	-1.61 ± 0.93	-182.82 ± 12.35	-102.01 ± 19.96	-23.73 ± 10.47
RADO	4.93 ± 1.54	-8.63 ± 2.64	2.36 ± 1.43	0.38 ± 0.25	-0.80 ± 0.45	-6.57 ± 0.23
SJUA	1.55 ± 1.07	1.07 ± 2.21	-2.63 ± 0.90	-0.76 ± 0.27	0.85 ± 0.57	-1.54 ± 0.23
SRGD	1.59 ± 1.06	-1.87 ± 1.60	1.16 ± 0.97	-1.72 ± 0.18	1.07 ± 0.28	-2.19 ± 0.16
TQPL	-5.39 ± 1.67	-2.06 ± 3.14	-1.00 ± 1.41	-26.91 ± 19.780	41.99 ± 38.62	-32.49 ± 16.98
TORA	0.7 ± 2.09	-1.84 ± 4.14	-1.49 ± 1.82	-	-	-
TRTA	-18.51 ± 1.47	-9.86 ± 2.76	5.07 ± 1.23	-26.21 ± 17.79	69.70 ± 34.31	-146.19 ± 14.96
UAPE	8.93 ± 0.78	-531.76 ± 1.45	87.50 ± 0.69	-9.07 ± 0.28	-63.35 ± 0.53	-11.60 ± 0.25
UCNF	0.17 ± 0.93	-0.07 ± 1.69	0.25 ± 0.95	-2.05 ± 0.20	1.12 ± 0.37	-3.53 ± 0.20
UTAR	-72.31 ± 2.15	-59.31 ± 4.34	-26.65 ± 1.96	142.16 ± 21.29	-12.56 ± 42.52	-438.67 ± 19.28
VLZL	-0.44 ± 1.14	-0.96 ± 2.09	-1.53 ± 1.15	-2.25 ± 0.26	0.62 ± 0.49	-3.26 ± 0.26

Table S15. Coseismic offsets values estimated using a Trajectory Model for an earthquake M_w 6.4, 23/06/2001). Values are in mm.

Station	$N \pm \sigma_N$	$E \pm \sigma_E$	$U \pm \sigma_U$
AREQ	-9.86 ± 1.53	-13.91 ± 2.56	1.23 ± 1.20
UAPE	-2.93 ± 1.81	3.29 ± 3.43	-2.51 ± 1.74

Table S16. Coseismic offsets values estimated using a Trajectory Model for an earthquake M_w 7.3, 07/07/2001). Values are in mm.

Station	$N \pm \sigma_N$	$E \pm \sigma_E$	$U \pm \sigma_U$
AREQ	-38.03 ± 0.65	-34.39 ± 1.08	-7.97 ± 0.50
UAPE	-2.89 ± 1.08	0.31 ± 2.03	-3.48 ± 1.03

Table S17. Coseismic offsets values estimated using a Trajectory Model for an earthquake M_w 6.3, 15/11/2007). Values are in mm.

Station	$N \pm \sigma_N$	$E \pm \sigma_E$	$U \pm \sigma_U$
AREQ	-38.03 ± 0.65	-34.39 ± 1.08	-7.97 ± 0.50
UAPE	-2.89 ± 1.08	0.31 ± 2.03	-3.48 ± 1.03

Table S18. Coseismic offsets values estimated using a Trajectory Model for an earthquake M_w 6.4, 16/12/2007). Values are in mm.

Station	$N \pm \sigma_N$	$E \pm \sigma_E$	$U \pm \sigma_U$
CBAA	0.19 ± 0.28	-1.42 ± 0.48	-1.23 ± 0.26
CDLC	0.76 ± 0.37	-1.93 ± 0.65	-0.68 ± 0.36
CJNT	1.33 ± 0.36	-1.29 ± 0.61	-1.09 ± 0.35
CRSC	0.04 ± 0.32	0.36 ± 0.6	0.08 ± 0.31
CTLR	-0.08 ± 0.39	-0.26 ± 0.74	2.54 ± 0.38
JRGN	4.03 ± 0.4	-6.71 ± 0.73	-9.82 ± 0.4
MCLA	-0.17 ± 0.38	-4.35 ± 0.71	-1.31 ± 0.38
PB01	0.35 ± 0.32	0.11 ± 0.56	-2.9 ± 0.3
PB02	-0.17 ± 0.33	0.71 ± 0.6	-0.9 ± 0.32
PB03	-0.31 ± 0.35	0.72 ± 0.65	-0.43 ± 0.34
PB04	-0.34 ± 0.28	-0.15 ± 0.48	-2.32 ± 0.27
PB05	-0.79 ± 0.4	-3.4 ± 0.78	-1.18 ± 0.41
PMEJ	-1.15 ± 0.55	-6.69 ± 1.08	-27.36 ± 0.56
QUIL	0.04 ± 1.59	0.15 ± 3.12	1.12 ± 1.63
RADO	0.78 ± 0.51	1.94 ± 0.93	7.84 ± 0.49
SRGD	0.96 ± 0.4	-1.39 ± 0.69	-0.65 ± 0.38
URCU	0.31 ± 0.85	0.17 ± 1.75	-1.08 ± 0.87
VLZL	-3.44 ± 0.5	2.21 ± 0.95	10.28 ± 0.51

Table S19. Coseismic offsets values estimated using a Trajectory Model for an earthquake M_w 6.3, 04/02/2008). Values are in mm.

Station	$N \pm \sigma_N$	$E \pm \sigma_E$	$U \pm \sigma_U$
AEDA	-3.72 ± 0.56	0.96 ± 1.17	1.65 ± 0.55
ATJN	-1.03 ± 0.19	-0.72 ± 0.35	2.71 ± 0.17
CHMZ	-2.97 ± 0.14	-1.48 ± 0.24	3.04 ± 0.13
COLC	-1.3 ± 0.25	-4.22 ± 0.46	-1.71 ± 0.22
CRSC	-2.1 ± 0.26	-0.26 ± 0.49	-0.7 ± 0.25
CTLR	-1.02 ± 0.34	0.7 ± 0.64	1.1 ± 0.33
MICA	-1.56 ± 0.95	1.53 ± 1.85	-0.13 ± 0.93
PB01	-0.47 ± 0.23	-0.1 ± 0.4	-1.8 ± 0.22
PB02	-0.84 ± 0.24	0.45 ± 0.43	-1.58 ± 0.23
PCCL	-0.59 ± 0.15	0.37 ± 0.27	1.67 ± 0.14
PCHA	-2.64 ± 0.32	-2.97 ± 0.62	4.46 ± 0.28
PSGA	-2.33 ± 0.21	-1.6 ± 0.43	-0.8 ± 0.2
QUIL	0.67 ± 1.08	-0.76 ± 2.12	2.19 ± 1.12
UAPE	-1.52 ± 0.26	1.69 ± 0.5	5.77 ± 0.25
URCU	0.23 ± 0.74	-2.73 ± 1.56	-3.14 ± 0.78
UTAR	-1.17 ± 0.24	-0.24 ± 0.48	3.46 ± 0.22

Table S20. Coseismic offsets values estimated using a Trajectory Model for an earthquake M_w 6.5, 13/11/2009). Values are in mm.

Station	$N \pm \sigma_N$	$E \pm \sigma_E$	$U \pm \sigma_U$
ATJN	-4.57 ± 0.12	-11.47 ± 0.24	-2.35 ± 0.12
CGTC	1.03 ± 0.15	-2.31 ± 0.26	-0.82 ± 0.14
CHMZ	-0.38 ± 0.08	-1.72 ± 0.14	1.59 ± 0.07
CLLA	-0.62 ± 0.17	-0.79 ± 0.32	0.8 ± 0.16
COLC	6.05 ± 0.18	-2.67 ± 0.35	-15.09 ± 0.16
CRSC	-0.04 ± 0.12	-0.19 ± 0.22	-0.23 ± 0.12
HMBS	2.0 ± 0.29	2.95 ± 0.65	8.0 ± 0.3
IQQE	0.03 ± 0.1	-1.49 ± 0.2	-0.05 ± 0.1
LYAR	-0.65 ± 0.13	-1.16 ± 0.24	0.02 ± 0.12
MNMI	-1.98 ± 0.18	-3.62 ± 0.38	-0.02 ± 0.17
PB01	0.17 ± 0.11	0.18 ± 0.19	0.81 ± 0.1
PB08	-0.54 ± 0.55	-1.43 ± 1.06	2.9 ± 0.52
PCCL	-1.34 ± 0.11	-2.1 ± 0.19	-0.9 ± 0.1
PSGA	-0.94 ± 0.16	-9.56 ± 0.33	-2.68 ± 0.16
PTCL	0.14 ± 0.18	-1.88 ± 0.34	17.39 ± 0.16
PTRE	-3.21 ± 0.07	-0.67 ± 0.12	4.48 ± 0.07
TQPL	-0.18 ± 0.24	-2.05 ± 0.47	-0.43 ± 0.21
TRTA	-2.66 ± 0.16	-2.32 ± 0.31	0.59 ± 0.14
UAPE	-1.52 ± 0.71	-0.74 ± 1.42	1.89 ± 0.68

Table S21. Coseismic offsets values estimated using a Trajectory Model for an earthquake M_w 6.3, 24/03/2010). Values are in mm.

Station	$N \pm \sigma_N$	$E \pm \sigma_E$	$U \pm \sigma_U$
CBA	0.96 ± 0.14	-0.44 ± 0.24	-2.17 ± 0.14
CDLC	0.2 ± 0.22	-0.98 ± 0.41	-2.26 ± 0.2
CJNT	1.2 ± 0.16	-1.11 ± 0.27	-2.04 ± 0.15
CLLA	0.58 ± 0.16	-0.44 ± 0.3	1.11 ± 0.15
CTLR	0.84 ± 0.18	0.17 ± 0.34	-3.04 ± 0.17
MICA	0.53 ± 0.25	-0.3 ± 0.48	1.11 ± 0.25
PB04	1.46 ± 0.09	0.08 ± 0.17	-0.6 ± 0.09
RADO	0.11 ± 0.14	0.49 ± 0.26	-6.27 ± 0.14
SRGD	0.96 ± 0.13	-0.53 ± 0.22	-1.07 ± 0.13

Table S22. Coseismic offsets values estimated using a Trajectory Model for an earthquake M_w 6.1, 23/05/2010). Values are in mm.

Station	$N \pm \sigma_N$	$E \pm \sigma_E$	$U \pm \sigma_U$
GUAD	0.33 ± 0.16	0.86 ± 0.36	3.58 ± 0.14

Table S23. Coseismic offsets values estimated using a Trajectory Model for an earthquake M_w 6.3, 12/07/2010). Values are in mm.

Station	$N \pm \sigma_N$	$E \pm \sigma_E$	$U \pm \sigma_U$
CBA	0.81 ± 0.14	0.39 ± 0.24	0.41 ± 0.13
CDLC	-0.23 ± 0.23	0.04 ± 0.41	4.8 ± 0.23
CJNT	0.63 ± 0.15	0.81 ± 0.26	1.55 ± 0.15
MICA	0.97 ± 0.26	0.6 ± 0.5	-0.2 ± 0.26
PB06	1.04 ± 0.16	-0.96 ± 0.31	2.53 ± 0.16
SRGD	0.41 ± 0.12	0.3 ± 0.19	1.51 ± 0.11

Table S24. Coseismic offsets values estimated using a Trajectory Model for an earthquake M_w 6.3, 06/03/2011). Values are in mm.

Station	$N \pm \sigma_N$	$E \pm \sigma_E$	$U \pm \sigma_U$
ATJN	1.6 ± 0.24	-0.52 ± 0.49	-2.05 ± 0.23
LYAR	0.13 ± 0.15	0.55 ± 0.3	-1.03 ± 0.14
MNMI	-0.07 ± 0.19	-1.13 ± 0.4	-0.02 ± 0.18
PCCL	0.09 ± 0.12	0.38 ± 0.22	-2.09 ± 0.11
PTRE	0.46 ± 0.08	0.1 ± 0.14	-2.24 ± 0.07
TQPL	-0.25 ± 0.21	-0.93 ± 0.42	-3.03 ± 0.19
TRTA	0.9 ± 0.16	-1.91 ± 0.32	0.25 ± 0.15

Table S25. Coseismic offsets values estimated using a Trajectory Model for an earthquake M_w 6.4, 20/06/2011). Values are in mm.

Station	$N \pm \sigma_N$	$E \pm \sigma_E$	$U \pm \sigma_U$
CBAA	0.47 ± 0.11	-0.76 ± 0.19	0.41 ± 0.11
CDLC	0.06 ± 0.12	-1.57 ± 0.2	-0.12 ± 0.11
CLLA	0.41 ± 0.13	-1.25 ± 0.23	0.87 ± 0.12
MICA	0.61 ± 0.24	-1.59 ± 0.46	-1.8 ± 0.24
PB01	0.5 ± 0.12	-1.14 ± 0.2	0.79 ± 0.11
PB07	0.19 ± 0.17	-1.83 ± 0.3	0.61 ± 0.16
RADO	-0.49 ± 0.15	-0.57 ± 0.28	-5.41 ± 0.15
SRGD	0.24 ± 0.09	-1.13 ± 0.16	0.16 ± 0.09

Table S26. Coseismic offsets values estimated using a Trajectory Model for an earthquake M_w 6.9, 28/10/2011). Values are in mm.

Station	$N \pm \sigma_N$	$E \pm \sigma_E$	$U \pm \sigma_U$
ATIC	-0.52 ± 0.14	-0.26 ± 0.29	-2.33 ± 0.13
CHRA	-0.5 ± 0.17	-1.63 ± 0.35	-0.34 ± 0.16
GLRV	-1.64 ± 0.25	-2.44 ± 0.53	-1.08 ± 0.21
GUAD	-11.17 ± 0.2	-8.19 ± 0.46	-4.24 ± 0.17
HUAN	-1.87 ± 0.35	-2.42 ± 0.77	-1.55 ± 0.28
NZCA	-0.14 ± 0.19	-8.28 ± 0.41	-2.41 ± 0.17
PTIN	-0.57 ± 0.18	-0.71 ± 0.38	2.55 ± 0.17
SJUA	-0.05 ± 0.18	-2.12 ± 0.38	-1.93 ± 0.16

Table S27. Coseismic offsets values estimated using a Trajectory Model for an earthquake M_w 6.4, 30/01/2012). Values are in mm.

Station	$N \pm \sigma_N$	$E \pm \sigma_E$	$U \pm \sigma_U$
GLRV	1.58 ± 0.22	-2.6 ± 0.47	-0.12 ± 0.18
GUAD	1.41 ± 0.21	-4.72 ± 0.47	0.12 ± 0.17
LAGU	3.33 ± 0.28	-6.16 ± 0.62	-1.37 ± 0.25
LOMI	-3.02 ± 0.23	-2.5 ± 0.51	2.73 ± 0.19

Table S28. Coseismic offsets values estimated using a Trajectory Model for an earthquake M_w 6.2, 14/05/2012). Values are in mm.

Station	$N \pm \sigma_N$	$E \pm \sigma_E$	$U \pm \sigma_U$
ATJN	0.43 ± 0.13	0.63 ± 0.25	0.1 ± 0.12
COLC	-0.78 ± 0.2	0.45 ± 0.39	5.09 ± 0.18
DANC	0.48 ± 0.15	-1.38 ± 0.27	0.56 ± 0.14
LYAR	0.47 ± 0.13	-0.18 ± 0.25	-1.2 ± 0.12
MNMI	-0.34 ± 0.19	-0.34 ± 0.4	0.09 ± 0.18
PALC	0.84 ± 0.26	-1.45 ± 0.62	-1.64 ± 0.26
PCCL	0.46 ± 0.13	0.94 ± 0.24	-0.22 ± 0.12
PSGA	-0.44 ± 0.15	1.26 ± 0.31	-1.17 ± 0.15
PTCL	0.56 ± 0.13	0.01 ± 0.25	-5.45 ± 0.12
TQPL	-0.12 ± 0.2	-0.46 ± 0.4	0.21 ± 0.18
TRTA	2.78 ± 0.17	2.11 ± 0.33	1.42 ± 0.15
UTAR	-0.45 ± 0.18	1.44 ± 0.37	-2.66 ± 0.17

Table S29. Coseismic offsets values estimated using a Trajectory Model for an earthquake M_w 6.1, 07/06/2012). Values are in mm.

Station	$N \pm \sigma_N$	$E \pm \sigma_E$	$U \pm \sigma_U$
AREQ	0.43 ± 0.12	0.21 ± 0.22	2.51 ± 0.1
ATIC	0.21 ± 0.15	-0.71 ± 0.3	0.86 ± 0.13
CHRA	-0.37 ± 0.17	-0.8 ± 0.35	-0.29 ± 0.16
QUCA	2.34 ± 0.35	0.37 ± 0.73	-9.66 ± 0.33

Table S30. Coseismic offsets values estimated using a Trajectory Model for Acari earthquake M_w 7.1 (25/09/2013). Values are in mm.

Station	$N \pm \sigma_N$	$E \pm \sigma_E$	$U \pm \sigma_U$
AREQ	0.05 ± 0.11	0.36 ± 0.21	-1.01 ± 0.09
ATIC	-1.91 ± 0.16	-0.2 ± 0.32	-2.94 ± 0.14
CHRA	-1.19 ± 0.2	0.67 ± 0.4	-0.57 ± 0.18
DANC	0.14 ± 0.17	0.93 ± 0.3	-1.6 ± 0.14
GLRV	-6.8 ± 0.42	-1.67 ± 0.9	-2.9 ± 0.34
GUAD	-0.92 ± 0.17	-0.75 ± 0.36	-1.04 ± 0.14
LAGU	1.02 ± 0.15	-2.14 ± 0.33	6.54 ± 0.13
LOMI	8.18 ± 0.18	1.78 ± 0.4	-3.81 ± 0.15
LYAR	0.15 ± 0.13	0.79 ± 0.24	-2.36 ± 0.12
NZCA	-2.79 ± 0.17	-0.34 ± 0.37	-1.91 ± 0.15
PALC	0.77 ± 0.27	-0.61 ± 0.67	-1.48 ± 0.27
PCCL	0.57 ± 0.14	1.32 ± 0.25	-2.84 ± 0.12
PTCL	0.7 ± 0.43	2.22 ± 0.85	6.08 ± 0.39
SJUA	6.2 ± 0.17	-5.02 ± 0.36	2.64 ± 0.15
TQPL	0.12 ± 0.19	0.36 ± 0.38	-2.73 ± 0.16
TRTA	-0.77 ± 0.16	1.52 ± 0.31	-1.7 ± 0.14
UTAR	0.09 ± 0.19	0.63 ± 0.4	-5.86 ± 0.18

Table S31. Coseismic offsets values estimated using a Trajectory Model for an earthquake M_w 6.3, 03/03/2014). Values are in mm.

Station	$N \pm \sigma_N$	$E \pm \sigma_E$	$U \pm \sigma_U$
AEDA	-0.58 ± 0.57	-0.31 ± 1.16	0.38 ± 0.56
ATJN	-0.14 ± 0.45	0.87 ± 0.87	-4.6 ± 0.42
CGTC	-1.12 ± 0.36	0.38 ± 0.64	-3.22 ± 0.33
CHMZ	-0.35 ± 0.33	0.28 ± 0.55	-2.29 ± 0.3
CRSC	0.06 ± 0.39	-0.14 ± 0.71	-2.46 ± 0.37
IQQE	-0.78 ± 0.38	0.27 ± 0.79	-2.97 ± 0.37
LYAR	-0.23 ± 0.39	2.06 ± 0.72	-1.11 ± 0.35
MNMI	-1.76 ± 0.5	-0.31 ± 1.0	-0.17 ± 0.46
PB01	-0.0 ± 0.36	0.84 ± 0.61	-2.18 ± 0.33
PB02	-0.33 ± 0.35	0.5 ± 0.61	-0.53 ± 0.33
PB08	-0.86 ± 0.46	0.95 ± 0.87	0.61 ± 0.44
PB11	-2.68 ± 0.76	-1.36 ± 1.45	1.2 ± 0.71
PCCL	-0.8 ± 0.43	1.5 ± 0.8	-3.04 ± 0.38
PCHA	0.52 ± 0.69	2.35 ± 1.38	0.3 ± 0.64
PICC	-0.12 ± 0.39	2.1 ± 0.71	-2.29 ± 0.36
PSGA	-0.07 ± 0.5	0.26 ± 1.01	0.25 ± 0.47
UAPE	-1.13 ± 0.63	-1.72 ± 1.16	-7.42 ± 0.56
UTAR	-1.2 ± 0.58	2.37 ± 1.21	-3.57 ± 0.54

Table S32. Coseismic offsets values estimated using a Trajectory Model for an earthquake M_w 6.2, 14/03/2014). Values are in mm.

Station	$N \pm \sigma_N$	$E \pm \sigma_E$	$U \pm \sigma_U$
AEDA	-0.58 ± 0.57	-0.31 ± 1.16	0.38 ± 0.56
GUAD	-1.84 ± 1.56	-1.84 ± 3.14	1.83 ± 1.15
LAGU	-1.7 ± 1.5	-1.22 ± 3.31	0.23 ± 1.27
LOMI	1.14 ± 1.49	1.59 ± 3.1	4.22 ± 1.13
NZCA	-2.44 ± 0.38	1.08 ± 0.82	2.72 ± 0.32
SJUA	-1.46 ± 0.39	0.74 ± 0.84	2.48 ± 0.34

Table S33. Coseismic offsets values estimated using a Trajectory Model for an earthquake M_w 6.0, 15/03/2014). Values are in mm.

Station	$N \pm \sigma_N$	$E \pm \sigma_E$	$U \pm \sigma_U$
GUAD	-2.1 ± 1.61	0.1 ± 3.26	5.15 ± 1.19
LAGU	-1.76 ± 1.55	-6.94 ± 3.42	-6.67 ± 1.31
LOMI	0.19 ± 1.53	0.14 ± 3.19	-1.83 ± 1.16

Table S34. Coseismic offsets values estimated using a Trajectory Model for an earthquake M_w 6.6, 16/03/2014). Values are in mm.

Station	$N \pm \sigma_N$	$E \pm \sigma_E$	$U \pm \sigma_U$
AEDA	-0.25 ± 1.77	1.33 ± 3.63	-2.97 ± 1.74
ATJN	-0.93 ± 1.54	0.18 ± 2.96	-2.52 ± 1.41
CDLC	-5.79 ± 0.12	-2.69 ± 0.21	-4.04 ± 0.11
CGTC	-0.58 ± 1.28	1.9 ± 2.34	-6.81 ± 1.19
CHMZ	-0.6 ± 1.1	1.35 ± 1.85	-0.91 ± 0.99
COLC	-2.68 ± 0.48	0.39 ± 0.92	1.99 ± 0.43
CRSC	-0.65 ± 1.33	1.41 ± 2.49	-0.27 ± 1.27
DANC	-2.05 ± 0.34	0.08 ± 0.6	4.81 ± 0.28
IQQE	-1.07 ± 1.28	2.42 ± 2.63	-5.07 ± 1.22
LYAR	-2.43 ± 0.6	-0.44 ± 1.09	4.37 ± 0.53
PALC	-2.56 ± 0.56	0.86 ± 1.36	3.84 ± 0.54
PB01	-1.7 ± 0.44	-0.77 ± 0.75	5.63 ± 0.4
PB02	0.64 ± 1.22	0.51 ± 2.16	-1.87 ± 1.16
PB03	-1.8 ± 0.38	1.11 ± 0.7	1.94 ± 0.37
PB04	-1.58 ± 0.29	1.29 ± 0.49	2.21 ± 0.27
PB07	-2.29 ± 0.34	1.57 ± 0.61	3.16 ± 0.32
PB08	-0.34 ± 1.57	1.14 ± 3.0	0.99 ± 1.48
PB11	-1.36 ± 1.72	-0.2 ± 3.32	2.47 ± 1.6
PCCL	-1.98 ± 0.72	-0.28 ± 1.32	3.65 ± 0.63
PCHA	-0.72 ± 2.29	0.84 ± 4.62	-3.32 ± 2.1
PICC	-0.87 ± 1.34	0.62 ± 2.5	-3.81 ± 1.26
PSGA	-0.46 ± 1.66	2.01 ± 3.44	-0.13 ± 1.6
PTCL	-2.96 ± 0.44	2.93 ± 0.85	5.35 ± 0.38
PTRE	-2.08 ± 0.41	1.64 ± 0.67	1.01 ± 0.35
RADO	-1.4 ± 0.37	0.33 ± 0.66	13.56 ± 0.36
TORA	-2.34 ± 0.55	3.5 ± 1.09	1.02 ± 0.47
TQPL	-1.96 ± 0.46	1.28 ± 0.9	4.3 ± 0.4
TRTA	-4.28 ± 0.4	1.35 ± 0.77	5.19 ± 0.33
UAPE	-0.84 ± 2.01	2.09 ± 3.75	-4.92 ± 1.78
UTAR	-0.62 ± 1.88	-0.72 ± 3.92	-2.86 ± 1.75

Table S35. Coseismic offsets values estimated using a Trajectory Model for an earthquake M_w 6.1, 17/03/2014). Values are in mm.

Station	$N \pm \sigma_N$	$E \pm \sigma_E$	$U \pm \sigma_U$
AEDA	0.58 ± 1.9	-2.78 ± 3.88	4.08 ± 1.86
ATJN	-3.96 ± 1.63	-3.99 ± 3.13	5.27 ± 1.49
CGTC	0.06 ± 1.36	-5.4 ± 2.47	9.54 ± 1.26
CHMZ	-1.92 ± 1.15	-2.31 ± 1.93	4.79 ± 1.04
CRSC	0.57 ± 1.43	-1.47 ± 2.66	3.82 ± 1.36
IQQE	0.8 ± 1.36	-6.5 ± 2.79	8.64 ± 1.3
PB02	-2.1 ± 1.21	-0.8 ± 2.14	4.79 ± 1.14
PB08	-1.65 ± 1.65	-0.76 ± 3.13	2.76 ± 1.54
PB11	-1.37 ± 1.82	-3.43 ± 3.49	4.2 ± 1.68
PCHA	-1.46 ± 2.44	-2.17 ± 4.89	8.61 ± 2.22
PICC	-0.23 ± 1.39	-1.67 ± 2.59	6.17 ± 1.31
PSGA	-4.42 ± 1.76	-5.78 ± 3.62	3.43 ± 1.68
UAPE	0.5 ± 2.14	-5.23 ± 3.99	11.73 ± 1.89
UTAR	-1.99 ± 2.02	1.03 ± 4.18	7.85 ± 1.86

Table S36. Coseismic offsets values estimated using a Trajectory Model for an earthquake M_w 6.0, 22/03/2014). Values are in mm.

Station	$N \pm \sigma_N$	$E \pm \sigma_E$	$U \pm \sigma_U$
AEDA	-1.02 ± 2.03	-2.75 ± 4.12	-2.58 ± 1.95
ATJN	-2.51 ± 1.62	-4.01 ± 3.01	-2.16 ± 1.44
CGTC	-1.69 ± 1.3	-4.84 ± 2.25	-2.46 ± 1.16
CRSC	-2.13 ± 1.46	-3.76 ± 2.63	-1.72 ± 1.35
IQQE	-1.61 ± 1.38	-3.52 ± 2.77	-1.78 ± 1.28
PB11	-2.75 ± 1.8	-4.8 ± 3.38	-3.4 ± 1.63
PCCL	-2.22 ± 1.46	-4.13 ± 2.64	-2.72 ± 1.25
PCHA	-2.36 ± 2.57	-3.9 ± 5.09	-1.65 ± 2.33
PSGA	-2.15 ± 1.84	-5.14 ± 3.68	-0.68 ± 1.71
UAPE	-1.6 ± 2.26	-5.71 ± 4.22	2.49 ± 1.98
UTAR	-1.94 ± 2.12	-5.62 ± 4.38	-2.8 ± 1.92

Table S37. Coseismic offsets values estimated using a Trajectory Model for an earthquake M_w 6.2, 23/03/2014). Values are in mm.

Station	$N \pm \sigma_N$	$E \pm \sigma_E$	$U \pm \sigma_U$
AEDA	1.97 ± 1.94	1.96 ± 3.93	5.99 ± 1.86
ATJN	-0.72 ± 1.54	-1.32 ± 2.86	4.02 ± 1.36
CGTC	1.78 ± 1.23	1.19 ± 2.12	4.36 ± 1.1
CHMZ	-0.12 ± 0.58	-1.52 ± 0.96	0.72 ± 0.51
CRSC	1.64 ± 1.38	2.94 ± 2.49	4.92 ± 1.28
IQQE	1.79 ± 1.31	1.4 ± 2.63	1.9 ± 1.21
LYAR	-0.26 ± 0.63	-0.42 ± 1.13	1.06 ± 0.55
PB08	0.04 ± 0.82	-0.98 ± 1.51	1.31 ± 0.75
PB11	1.1 ± 1.71	0.4 ± 3.22	4.99 ± 1.55
PCCL	0.75 ± 1.4	2.47 ± 2.54	5.12 ± 1.2
PCHA	1.13 ± 2.45	1.43 ± 4.86	5.74 ± 2.22
PICC	-0.19 ± 0.68	-1.26 ± 1.21	1.44 ± 0.62
PSGA	-0.34 ± 1.76	-2.75 ± 3.54	0.45 ± 1.64
PTRE	-0.85 ± 0.52	-0.95 ± 0.85	1.6 ± 0.44
UAPE	2.42 ± 2.15	3.28 ± 4.03	-0.1 ± 1.89
UTAR	1.26 ± 2.02	3.42 ± 4.15	2.84 ± 1.82

Table S38. Coseismic offsets values estimated using a Trajectory Model for an earthquake M_w 6.2, 24/08/2014). Values are in mm.

Station	$N \pm \sigma_N$	$E \pm \sigma_E$	$U \pm \sigma_U$
ATIC	-1.41 ± 0.23	1.23 ± 0.45	0.14 ± 0.2
NZCA	-1.97 ± 0.26	-0.02 ± 0.53	1.31 ± 0.22

Table S39. Inverted values for North noise parameters, following $P(f) = P_0 (f^{-\alpha} + f_0^{-\alpha})$

Station	P_0	σ_{P0}	f_0	σ_{f0}	α	σ_α
AEDA	3.77	0.49	0.14	0.03	0.52	0.05
AREQ	3.03	0.75	0.05	0.01	0.66	0.06
ATIC	6.62	0.47	0.23	0.02	0.39	0.03
ATJN	6.65	0.45	0.14	0.02	0.35	0.03
CBA	2.22	0.27	0.1	0.02	0.53	0.04
CDLC	3.18	0.35	0.15	0.02	0.6	0.04
CGTC	0.74	0.4	0.02	0.01	0.7	0.13
CHMZ	2.69	0.45	0.11	0.03	0.51	0.05
CHRA	2.21	0.47	0.09	0.02	0.66	0.05
CJNT	2.12	0.34	0.08	0.02	0.6	0.05
CLLA	2.0	0.87	0.03	0.01	0.42	0.13
COLC	3.75	0.95	0.09	0.02	0.57	0.07
COLL	2.75	0.81	0.08	0.02	0.37	0.12
CRSC	4.81	0.42	0.15	0.02	0.29	0.04
CTLR	4.03	0.55	0.07	0.02	0.44	0.04
DANC	4.36	0.55	0.21	0.02	0.23	0.07
ENAP	4.68	0.78	0.09	0.02	0.49	0.06
FBAQ	1.43	0.22	0.1	0.02	0.78	0.04
GLRV	2.56	0.42	0.09	0.02	0.51	0.06
GUAD	4.96	0.67	0.1	0.02	0.52	0.04
HMBS	1.54	0.39	0.11	0.02	0.76	0.08
HUAN	4.18	0.43	0.22	0.02	0.38	0.05
IQQE	2.0	0.56	0.04	0.01	0.61	0.07
JRGN	3.24	0.64	0.07	0.01	0.58	0.06
LAGN	3.72	0.68	0.17	0.01	0.05	0.1
LAGU	4.98	1.08	0.09	0.02	0.58	0.06
LOMI	4.62	0.62	0.2	0.02	0.83	0.05
LYAR	6.06	1.12	0.04	0.02	0.17	0.06
MCLA	3.1	0.68	0.06	0.02	0.38	0.07
MICA	0.9	0.52	0.03	0.01	0.67	0.14
MNMI	4.24	0.35	0.15	0.02	0.44	0.03
NZCA	3.37	0.66	0.1	0.02	0.54	0.06
PALC	4.48	0.43	0.23	0.02	0.35	0.05

Table S40. Continuation of Table S39, with the same caption.

Station	P_0	σ_{P_0}	f_0	σ_{f_0}	α	σ_α
PB01	1.5	0.93	0.03	0.01	0.61	0.15
PB02	4.86	0.58	0.11	0.02	0.26	0.05
PB03	3.73	0.44	0.08	0.01	0.33	0.05
PB04	2.67	0.68	0.06	0.02	0.53	0.07
PB05	2.74	0.71	0.06	0.02	0.44	0.08
PB06	2.03	0.71	0.04	0.02	0.45	0.1
PB07	2.01	0.61	0.05	0.02	0.52	0.09
PB08	1.05	0.51	0.04	0.02	0.68	0.1
PB11	0.62	0.14	0.08	0.01	0.84	0.07
PCCL	6.8	0.5	0.23	0.01	0.21	0.04
PCHA	3.05	0.56	0.14	0.03	0.69	0.06
PICC	1.12	0.57	0.03	0.01	0.72	0.11
PMCA	4.3	0.85	0.19	0.04	0.16	0.11
PMEJ	3.44	0.94	0.12	0.07	0.6	0.05
PSGA	4.01	0.37	0.17	0.02	0.46	0.04
PTCL	4.4	0.75	0.13	0.03	0.64	0.05
PTIN	3.86	0.48	0.15	0.02	0.44	0.06
PTRE	1.6	0.52	0.04	0.01	0.71	0.09
QUCA	3.89	0.45	0.25	0.01	0.46	0.05
QUIL	2.81	0.36	0.16	0.01	0.64	0.05
RADO	3.6	0.37	0.14	0.02	0.43	0.04
SJUA	5.63	0.51	0.22	0.03	0.36	0.04
SLRZ	4.85	0.76	0.15	0.02	0.41	0.07
SRGD	3.82	0.34	0.14	0.02	0.38	0.04
TORA	3.77	0.47	0.19	0.02	0.37	0.06
TQPL	3.85	0.46	0.12	0.02	0.4	0.05
TRTA	3.16	0.73	0.16	0.02	0.64	0.09
UAPE	2.68	0.68	0.05	0.01	0.72	0.06
UCNF	2.68	0.44	0.13	0.02	0.57	0.06
URCU	1.44	0.57	0.03	0.02	0.24	0.13
UTAR	4.64	0.51	0.14	0.02	0.64	0.03
VLZL	3.72	0.49	0.09	0.02	0.37	0.04

Table S41. Inverted values for East noise parameters, following $P(f) = P_0 (f^{-\alpha} + f_0^{-\alpha})$

Station	P_0	σ_{P0}	f_0	σ_{f0}	α	σ_α
AEDA	3.77	0.49	0.14	0.03	0.52	0.05
AREQ	3.03	0.75	0.05	0.01	0.66	0.06
ATIC	6.62	0.47	0.23	0.02	0.39	0.03
ATJN	6.65	0.45	0.14	0.02	0.35	0.03
CBA	2.22	0.27	0.1	0.02	0.53	0.04
CDLC	3.18	0.35	0.15	0.02	0.6	0.04
CGTC	0.74	0.4	0.02	0.01	0.7	0.13
CHMZ	2.69	0.45	0.11	0.03	0.51	0.05
CHRA	2.21	0.47	0.09	0.02	0.66	0.05
CJNT	2.12	0.34	0.08	0.02	0.6	0.05
CLLA	2.0	0.87	0.03	0.01	0.42	0.13
COLC	3.75	0.95	0.09	0.02	0.57	0.07
COLL	2.75	0.81	0.08	0.02	0.37	0.12
CRSC	4.81	0.42	0.15	0.02	0.29	0.04
CTLR	4.03	0.55	0.07	0.02	0.44	0.04
DANC	4.36	0.55	0.21	0.02	0.23	0.07
ENAP	4.68	0.78	0.09	0.02	0.49	0.06
FBAQ	1.43	0.22	0.1	0.02	0.78	0.04
GLRV	2.56	0.42	0.09	0.02	0.51	0.06
GUAD	4.96	0.67	0.1	0.02	0.52	0.04
HMBS	1.54	0.39	0.11	0.02	0.76	0.08
HUAN	4.18	0.43	0.22	0.02	0.38	0.05
IQQE	2.0	0.56	0.04	0.01	0.61	0.07
JRGN	3.24	0.64	0.07	0.01	0.58	0.06
LAGN	3.72	0.68	0.17	0.01	0.05	0.1
LAGU	4.98	1.08	0.09	0.02	0.58	0.06
LOMI	4.62	0.62	0.2	0.02	0.83	0.05
LYAR	6.06	1.12	0.04	0.02	0.17	0.06
MCLA	3.1	0.68	0.06	0.02	0.38	0.07
MICA	0.9	0.52	0.03	0.01	0.67	0.14
MNMI	4.24	0.35	0.15	0.02	0.44	0.03
NZCA	3.37	0.66	0.1	0.02	0.54	0.06
PALC	4.48	0.43	0.23	0.02	0.35	0.05

Table S42. Continuation of Table S41, with the same caption.

Station	P_0	σ_{P_0}	f_0	σ_{f_0}	α	σ_α
PB01	1.5	0.93	0.03	0.01	0.61	0.15
PB02	4.86	0.58	0.11	0.02	0.26	0.05
PB03	3.73	0.44	0.08	0.01	0.33	0.05
PB04	2.67	0.68	0.06	0.02	0.53	0.07
PB05	2.74	0.71	0.06	0.02	0.44	0.08
PB06	2.03	0.71	0.04	0.02	0.45	0.1
PB07	2.01	0.61	0.05	0.02	0.52	0.09
PB08	1.05	0.51	0.04	0.02	0.68	0.1
PB11	0.62	0.14	0.08	0.01	0.84	0.07
PCCL	6.8	0.5	0.23	0.01	0.21	0.04
PCHA	3.05	0.56	0.14	0.03	0.69	0.06
PICC	1.12	0.57	0.03	0.01	0.72	0.11
PMCA	4.3	0.85	0.19	0.04	0.16	0.11
PMEJ	3.44	0.94	0.12	0.07	0.6	0.05
PSGA	4.01	0.37	0.17	0.02	0.46	0.04
PTCL	4.4	0.75	0.13	0.03	0.64	0.05
PTIN	3.86	0.48	0.15	0.02	0.44	0.06
PTRE	1.6	0.52	0.04	0.01	0.71	0.09
QUCA	3.89	0.45	0.25	0.01	0.46	0.05
QUIL	2.81	0.36	0.16	0.01	0.64	0.05
RADO	3.6	0.37	0.14	0.02	0.43	0.04
SJUA	5.63	0.51	0.22	0.03	0.36	0.04
SLRZ	4.85	0.76	0.15	0.02	0.41	0.07
SRGD	3.82	0.34	0.14	0.02	0.38	0.04
TORA	3.77	0.47	0.19	0.02	0.37	0.06
TQPL	3.85	0.46	0.12	0.02	0.4	0.05
TRTA	3.16	0.73	0.16	0.02	0.64	0.09
UAPE	2.68	0.68	0.05	0.01	0.72	0.06
UCNF	2.68	0.44	0.13	0.02	0.57	0.06
URCU	1.44	0.57	0.03	0.02	0.24	0.13
UTAR	4.64	0.51	0.14	0.02	0.64	0.03
VLZL	3.72	0.49	0.09	0.02	0.37	0.04

Table S43. Detected events parameters

Event Id	Mw	Duration (Days)	Longitude (°)	Latitude (°)	Depth (km)	Time (Dec Yr)	Aseismic %	Type
1	6.03 ± 0.05	26.54 ± 10.37	-70.75	-18.73	43.06	2012.37	100.0	A*
2	6.13 ± 0.05	35.61 ± 7.49	-76.58	-13.78	27.37	2010.27	100.0	B
3	5.39 ± 0.18	26.82 ± 11.02	-70.4	-23.29	31.54	2009.19	85.15	B
4	5.73 ± 0.07	26.83 ± 9.1	-70.4	-23.29	31.54	2011.16	92.14	A
5	5.71 ± 0.07	31.15 ± 8.94	-70.4	-23.29	31.54	2012.76	98.64	B
6	5.74 ± 0.07	25.81 ± 10.62	-70.79	-22.87	19.91	2006.51	100.0	B
7	6.05 ± 0.07	28.08 ± 11.4	-70.52	-19.83	34.12	2014.46	88.39	A
8	5.78 ± 0.07	33.37 ± 9.11	-70.59	-19.55	34.83	2009.76	97.88	B
9	6.05 ± 0.06	19.91 ± 10.03	-75.63	-15.23	21.36	2012.17	100.0	B
10	5.92 ± 0.05	23.17 ± 9.6	-71.1	-18.67	32.04	2013.74	98.53	A*
11	6.03 ± 0.05	24.96 ± 8.33	-74.45	-15.36	54.24	2014.68	95.59	B*
12	6.02 ± 0.03	30.71 ± 6.75	-70.6	-21.0	24.02	2014.04	100.0	A
13	5.85 ± 0.07	22.59 ± 9.5	-70.5	-20.35	30.15	2008.08	99.99	B
14	5.66 ± 0.09	20.14 ± 10.9	-70.5	-20.35	30.15	2012.8	96.61	B
15	5.68 ± 0.1	23.54 ± 11.48	-70.5	-20.35	30.15	2013.17	98.26	B
16	5.67 ± 0.06	23.66 ± 12.13	-70.59	-23.12	25.67	2006.66	100.0	B
17	5.42 ± 0.22	22.06 ± 10.96	-74.99	-14.97	50.9	2012.87	99.24	B
18	6.2 ± 0.05	30.02 ± 9.57	-76.92	-13.78	18.57	2009.89	100.0	A
19	6.02 ± 0.07	17.3 ± 8.09	-76.92	-13.78	18.57	2010.74	100.0	A
20	5.99 ± 0.04	29.03 ± 11.66	-70.92	-23.67	19.03	2011.78	100.0	A
21	5.88 ± 0.06	23.6 ± 9.09	-70.92	-23.67	19.03	2014.68	100.0	A
22	5.92 ± 0.04	20.71 ± 10.23	-70.05	-23.79	45.21	2010.16	100.0	B
23	5.94 ± 0.06	34.25 ± 9.95	-70.36	-22.23	30.21	2014.39	100.0	A*
24	5.57 ± 0.13	17.82 ± 10.3	-70.66	-18.02	66.06	2011.92	100.0	B